

People's Democratic Republic of Algeria  
Ministry of Higher Education and Scientific Research  
University of 8 Mai 1945 Guelma



Faculty of Science and technology

Department of Process Engineering

Domiciliation laboratory of Industrial Analysis and Materials Engineering (LAIGM)

**THESIS FOR THE OBTAINING OF THE DOCTORATE DEGREE  
IN 3RD CYCLE**

Field: Science and Technology

Stream: Process Engineering

Speciality: Materials Process Engineering

**Presented by:  
Aouissi Lamaa**

*Title*

**Development of Ni-based coatings for corrosion protection**

Defended on :

Before the jury composed of:

<b>Mr Moahamed El hocine BENHAMZA</b>	<b>Prof</b>	Univ. of May 8, 1945 Guelma	President
<b>Meme Hayet MOUMENI</b>	<b>Prof</b>	Univ. of May 8, 1945 Guelma	Supervisor
<b>Mr Abderrafik NEMAMCHA</b>	<b>Prof</b>	Univ. of May 8, 1945 Guelma	Co- supervisor
<b>Mr Hakim MADANI</b>	<b>Prof</b>	Univ. of Batna	Examiner
<b>Meme Bisma MELLAH</b>	<b>Prof</b>	Univ. of Tunisia	Examiner
<b>Mr Abdelgani HESSAINIA</b>	<b>MCA</b>	Univ. of May 8, 1945 Guelma	Examiner

**Academic year: 2023-2024**

## **Acknowledgements**

*I express my gratitude to Allah, the Most Powerful, the Most Merciful, for giving me the strength, determination, and courage to accomplish this task.*

*it is with great pleasure that I express my gratitude for the extraordinary opportunity. I had to conduct my thesis work in collaboration with the Industrial Analysis and Materials Engineering Laboratory (LAIGM) at the 8 May 45 University of Guelma and laboratory of materials composite and clay minerals (LMCMA). The chance to work with these prestigious institutions was made possible through a residency training program abroad, generously granted by the Ministry of Higher Education and Scientific Research (MESRS). I would like to extend my sincere appreciation to everyone who supported me financially and demonstrated unwavering interest in my scientific pursuits.*

*I wish to express my sincere gratitude to my thesis supervisor, Pr. Hayet MOUMENI. Her expertise, guidance, and support throughout the course of this project have been invaluable. I am grateful for her willingness to welcome me into her team and for her dedication to ensuring the success of this thesis. Her encouragement and constructive feedback have been instrumental in shaping my research and improving my writing. I deeply appreciate her timely assistance with manuscript revisions and her thoughtful discussions, which have helped me to refine my ideas and methodology. I am honored to have had the opportunity to work with such a knowledgeable and supportive advisor. Thank you, Pr. MOUMENI, for all that you have done for me during this journey.*

*I want to express my sincere appreciation to Professor Abderrafik NEMAMCHA, my co-advisor from the University 8 Mai 1945 Guelma, for his invaluable guidance and encouragement during the completion of my thesis. I am grateful for his proposal, thoughtful insights, constructive feedback, and extensive knowledge in the field, which have been instrumental in my success. His unwavering confidence, patience, and support throughout these years of thesis are highly appreciated. I feel honored to have had him as my co-advisor and thankful for his contribution to my academic journey. Thank you, Professor NEMAMCHA.*

*I am grateful to Dr AMEL BOUTASTA Laboratory of Theoretical Physics, University Abou Beker Belkaid Tlemcen, for her help.*

*I am grateful to M. BESMA MELLAH, Research Director at (LMCMA), Borj Cedri, Tunisia, for their collaboration and generous support during my stay in Borj Cedri. Their availability, invaluable assistance, insightful remarks, unwavering encouragement, and guidance were instrumental in making my time there productive and enjoyable.*

*I am very grateful to Professor and Director of the Industrial Analysis and Materials Engineering Laboratory, Mohamed Elhocine BENHAMZA, for the honor he has bestowed upon me by agreeing to preside over my thesis committee.*

*I would like to express my sincere gratitude to Mr. Hakim MADANI, Professor at the University of Batna, and Mr. Abdelgan HESSAINIA, Professor at the University of Guelma, for agreeing to review this work.*

*I am deeply grateful to all the individuals who hold a special place in my heart, especially my husband HOCINE, for being a constant source of encouragement during my moments of doubt, anxiety, and high stress. Your unwavering support is truly appreciated and has been invaluable to me. I also extend my thanks to my family and my children for their daily support and love.*

*I want to extend my heartfelt appreciation to my friends especial my best friend slimani HANANE, fellow doctoral students, and all those who contributed to the success of this project, whether through their assistance, encouragement, guidance, or simply by brightening my day with a friendly smile."*

## TABLE OF CONTENTS

Table of contents.....	i
List of tables.....	vi
List of figures.....	vii
Abbreviation index.....	xi
Abstract .....	xii
General introduction.....	1

### Chapter I

#### Literature Review

I.1. Thin films.....	3
I.1. 1. Definition.....	3
I.1. 2. Thin films properties and applications.....	3
I.2. Electrodeposition.....	4
I.2.1. Electrodeposition principles.....	6
I.2.2 Electrodeposition mechanism.....	6
I.2.2.1. Mass transfer.....	7
I.2.2.1.1 Diffusion .....	7
I.2.2.1.2. Migration.....	7
I.2.2.1.3. Convection .....	8
I.2.2.2. Charge transfer.....	8
I.2.2.3. Crystallization.....	9
I.2.4. Nucleation .....	9
I.2.4.1. Nucleation kinetics .....	10
I.2.4.2. Instantaneous nucleation mode .....	10
I.2.4.3. Progressive nucleation mode .....	10
I.2.4.4. Scarifier–Hills model.....	12
I.2.5. Growth modes .....	13
I.2.5.1. 2D growth mode (Frank–Van der Merwe mechanism).....	13
I.2.5.2. 3D growth mode (Volmer–Weber mechanism).....	13
I.2.5.3. Growth mode 2D followed by 3D growth (Stranski–Krastanov mechanism).....	13

I.2.6 Parameters influencing the deposits.....	14
I.3. Metal co–deposition.....	14
I.3.1. Normal or regular Co–deposition.....	14
I.3.2. Irregular Co–deposition.....	14
I.3.3. Co–deposition at equilibrium.....	14
I.3.4. Abnormal Co–deposition (anomalous) .....	14
I.3.5. Induced Co–deposition.....	15
I.4. Corrosion.....	15
I.4.1. Corrosion definition.....	15
I.4.2 Corrosion mechanisms .....	15
I.4.2.1. Anodic reaction.....	16
I.4.2.2. Cathodic reaction.....	16
I.4.3. Different types of corrosion.....	16
I.4.3.1. Chemical (or dry) corrosion.....	17
I.4.3.2. Bacterial corrosion.....	17
I.4.2.3. Electrochemical corrosion .....	18
I.4.4. Corrosion form’s .....	18
I.4.4.1. Uniform corrosion.....	18
I.4.4.2. Galvanic corrosion.....	18
I.4.4.3. Crevice corrosion.....	18
I.4.4.4. Pitting corrosion.....	19
I.4.4.5. Stress corrosion cracking.....	19
I.4.4.6. Intergranular corrosion.....	19
I.4.5. Protective methods.....	19
I.4.5.1. Barrier protection.....	19
I.4.5.2. Cathodic protection.....	19
I.4.5.3. Anodic protection.....	19
I.4.5.4. Inhibitors.....	20
I.4.5.5. Alloying.....	20
I.4.4.6. Design modification.....	20
I.4.5.7. Environmental modification.....	20
I.4.6. Factors of corrosion.....	20
I.5. Electrodeposition of Ni–Mn and Zn–Ni–Mn alloys.....	21

I.5.1. Nickel (Ni) .....	21
I.5.2. Zinc (Zn).....	23
I.5.3. Manganese (Mn) .....	24
I.5.4. Ni–Mn Thin films .....	25
I.5.5. Zn–Ni–Mn Thin films.....	27
I.6. Conclusion.....	29

## Chapter II

### Materials and experimental techniques

II. 1. Chemical products.....	30
II.2. Bath preparation.....	31
II.3. Experimental setup.....	31
II.3.1. Potentiostat.....	32
II.3.2. Electrochemical cell.....	33
II. 3. 3. Electrodes.....	33
II.3.3.1. Working electrode.....	33
II.3.3.2. Reference electrode.....	34
II.3.3.3 Auxiliary electrode.....	35
II. 3. 4. Other devices used in the experiments.....	35
II. 4. Preparation of the substrates.....	37
II. 5. Experimental Methodology.....	37
II.5.1. Electrochemical techniques used for the kinetic study.....	39
II.5.1.1. Cyclic voltammetry.....	41
II.5.1.2. Chronoamperometry.....	41
II.5.2. Electrochemical methods for corrosion test.....	42
II.5.2.2 Open Circuit Potential (OCP) .....	42
II.5.2.3. Linear Tafel Polarization (LTP) .....	44
II.5.2.4. Electrochemical impedance spectroscopy.....	44
II.5.2.4. 1. Principle.....	45
II.5.2.4. 2. Nyquist and Bode diagrams.....	45
II.5.2.4.3. Charge transfer.....	46
II.5.2.4.4. surface heterogeneities.....	47

II.5.2.4.5. Diffusion in an infinitely thick layer.....	47
II.5.2.4.4. Adsorption step.....	48
II.5.3. Physical characterization techniques .....	49
II.5.3.1. Scanning Electron Microscope (SEM) .....	49
II.5.3.2. Energy Dispersive Spectroscopy (EDS) .....	50
II.5.3.3. X-Ray diffraction technique.....	51
II.6. Conclusion.....	54

### Chapter III

#### Electrochemical Study and Chemical composition of Ni–Mn, and Zn–Ni–Mn coatings

III.1. Electrochemical study.....	55
III.1.1 CV study.....	55
III.1.1.1. CV study of Ni.....	56
III.1.1.2. CV study of Zn.....	57
III.1.1.3. CV study of Mn.....	58
III.1.1.4. CV study of Ni–Zn.....	59
III.1.1.5. CV study of Zn–Mn.....	60
III.1.1.6. CV study of Ni–Mn.....	61
III.1.1.7. CV study of Zn–Ni–Mn.....	62
III.1.2. CA study.....	64
III.1.2.1. CA study of Ni.....	65
III.1.2.3. CA of Mn.....	67
III. 1. 2. 4 Effect of the applied potential on the nucleation process.....	68
III.1.2. 4 .1. Effect of the applied potential on Ni–Mn nucleation.....	69
III.1.2.4. 2. Effect of the applied potential on Zn–Ni–Mn.....	71
III.1.2. 5 The influence of [Mn <sup>2+</sup> ] on the coating’s nucleation.....	72
III.1.2. 5 .1. The influence of [Mn <sup>2+</sup> ] on Ni–Mn coatings nucleation.....	72
III.1.2.5. 2. The influence of [Mn <sup>2+</sup> ] on Zn–Ni–Mn coatings nucleation.....	74
III.2. Chemical composition analyses.....	76
III.2 .1. Chemical composition of Ni–Mn coatings.....	76

III.2. 2. Chemical composition of Zn–Ni–Mn coatings.....	77
III. 3. Conclusion.....	78

## Chapter IV

### Morphology, Structural characterization, and corrosion resistance of Ni–Mn and Zn – Ni –Mn coatings

IV.1. influence Mn content on morphology and structure of coatings.....	80
IV.1.1. Coatings surface morphology of coatings.....	80
IV.1.1.1. Surface morphology of Ni-Mn films.....	80
IV.1. 1.2. Surface morphology of Zn–Ni–Mn films.....	83
IV.1.2. XRD analysis.....	87
IV.1.2.1 Ni–Mn XRD analysis.....	87
IV.1.2.2 XRD examination of Zn–Ni–Mn films.....	88
IV.2. Influence of Mn content on Corrosion behavior.....	90
IV.2.1. Loss mass method.....	91
IV.2.1.1. Morphology of Ni–Mn coatings after corrosion test.....	91
IV.2.1.2. Morphology of Zn–Ni–Mn coatings after corrosion test .....	92
IV.2.1.3 XRD analyses of Ni–Mn coatings after corrosion test.....	93
IV.2.1.3 XRD analyses of Zn–Ni–Mn coatings after corrosion test.....	94
IV.2.2. Linear polarization resistance analyses.....	94
IV.2.2.1. Linear polarization resistance of Ni, Zn, and Mn.....	94
IV.2.2.2 Linear polarization resistance of Ni-Mn films.....	95
IV.2.2.3. Linear polarization resistance of Zn–Ni–Mn .....	98
IV. 2. 3. Electrochemical impedance analysis.....	101
IV.2.3.1. Electrochemical impedance spectroscopy of Ni–Mn coatings.....	101
III.2.3.2 Electrochemical impedance spectroscopy of Zn–Ni–Mn.....	108
IV.3. Conclusion .....	110
General Conclusion.....	113



## List of tables

<b>Table II. 1:</b> Different chemical products used for the elaboration of thin films. ....	30
<b>Table II. 2.</b> Composition of the electroplating baths.....	31
<b>Table IV. 1.</b> Results of loss mass method .....	90
<b>Table IV. 2.</b> Corrosion parameters and chemical composition of Ni–Mn coatings obtained with different $[\text{Mn}^{2+}]$ .....	97
<b>Table IV. 3.</b> Corrosion parameters and chemical composition of Zn–Ni–Mn coatings obtained with different $[\text{Mn}^{2+}]$ . ....	100
<b>Table IV. 4.</b> Parameter of electrochemical impedance spectroscopy EIS. ....	103
<b>Table IV. 5.</b> Parameter of electrochemical impedance spectroscopy EIS .....	107

## List of figures

<b>Figure I. 1.</b> Schematic representation of different applications of thin film .....	4
<b>Figure I. 2.</b> Schematic representation of the electrodeposition equipment. ....	5
<b>Figure I. 3.</b> Different mechanisms involved during electro-deposition .....	7
<b>Figure I. 4.</b> Diagram of the Electrode-Electrolyte Interface .....	8
<b>Figure I. 5.</b> Normalized Transients for Progressive and Instantaneous Nucleation. ....	60
<b>Figure I. 6.</b> Models of thin films development types .....	61
<b>Figure I. 7.</b> Pourbaix diagram of Nickel-H <sub>2</sub> O system at 25 °C .....	62
<b>Figure I. 8.</b> Pourbaix diagram of Zn-H <sub>2</sub> O system at 25 °C .....	63
<b>Figure I. 9.</b> Pourbaix diagram of Mn-H <sub>2</sub> O system at 25 °C .....	65
<b>Figure II. 1.</b> Electrochemical measurements device. ....	32
<b>Figure II. 2.</b> a) Photograph of the potentiostat/ galvanostat. b) Schematic representation of a potentiostat/galvanostat and its electronic circuit. ....	32
<b>Figure II. 3.</b> Photograph of the electrochemical cell.....	33
<b>Figure II. 4.</b> Working electrode used in experimental set up (copper substrate). ....	34
<b>Figure II. 5.</b> Reference electrode Ag/AgCl electrode. ....	34

<b>Figure II. 6.</b> Photograph of platinum electrode.....	35
<b>Figure II. 7. a)</b> Polisher, <b>b)</b> electronic balance, <b>c)</b> desiccator, <b>d)</b> PH meter, <b>e)</b> Magnetic agitator.....	36
<b>Figure II. 8.</b> Schematic illustration of potential variation at a designated scan rate.....	38
<b>Figure II. 9.</b> Schematic illustration of different CV curves depending on the system's speed. ....	39
<b>Figure II. 10.</b> Theoretical potentiostatic transient curve (current-time).....	40
<b>Figure II. 11.</b> Schematic representation of a current-potential curve and Tafel lines .....	41
<b>Figure II. 12. a)</b> Schematic illustration of corrosion cell, <b>b)</b> "Voltage-Current Relationship: Impedance Insight" <b>c)</b> "Linear Electrochemical Response Measurement" .....	45
<b>Figure II. 13.</b> Bode diagram, Nyquist diagram and Equivalent Electrical Circuit.....	46
<b>Figure II. 14.</b> A Nyquist plot depicting the electrochemical impedance associated with a charge transfer process and its Equivalent Electrical Circuit.....	47
<b>Figure II. 15.</b> Representation of the electrochemical impedance of a heterogeneous surface electrode and an equivalent electrical circuit in the Nyquist plane.....	47
<b>Figure II. 16.</b> Representation, in the Nyquist plot, of the electrochemical impedance where diffusion through an infinite layer is the limiting process of corrosion and its equivalent electrical circuit .....	48
<b>Figure II. 17.</b> Representation of the Nyquist Plot of electrochemical impedance of adsorbed species on an electrode surface and its equivalent electrical circuit .....	49
<b>Figure II. 18.</b> A photograph of a scanning electron microscope : HITACHI TM-1000.....	50
<b>Figure II. 19.</b> Schematic illustration of EDS technique principle.....	51
<b>Figure II. 20.</b> Schematic illustration of experimental device of X-ray diffraction technique.	52
<b>Figure II. 21.</b> A photograph of the diffractometer X'PERT PRO MPD PANALYTICAL. ..	53

<b>Figure. III. 1.</b> Cyclic voltammogram of a copper electrode in an electrolyte containing 0.2M Na <sub>2</sub> SO <sub>4</sub> and 0.5M H <sub>3</sub> BO <sub>3</sub> at 10 mV/s .....	56
<b>Figure. III. 2.</b> Cyclic voltammogram of Cu electrode immersed in Ni <sup>2+</sup> ions bath. ....	57
<b>Figure. III. 3.</b> Cyclic voltammograms of Cu electrode immersed in Zn <sup>2+</sup> ions bath. ....	58
<b>Figure. III. 4:</b> Cyclic voltammograms of Cu electrode immersed in Mn <sup>2+</sup> ions bath.....	59
<b>Figure. III. 5.</b> Cyclic voltammograms of Cu electrode immersed in bath of Ni <sup>2+</sup> , Zn <sup>2+</sup> ions. ....	60
<b>Figure. III. 6.</b> Cyclic voltammograms of Cu electrode immersed in a bath of Zn <sup>2+</sup> and Mn <sup>2+</sup> ions. ....	61
<b>Figure. III. 7.</b> Cyclic voltammograms of Cu electrode in different baths with different [Mn <sup>2+</sup> ] (0.05, 0.1, 0.2, 0.4) .....	62
<b>Figure. III. 8.</b> Cyclic voltammograms of Cu electrode immersed in different baths containing both Ni <sup>2+</sup> , Zn <sup>2+</sup> and Mn <sup>2+</sup> ions with different [Mn <sup>2+</sup> ] (0.05, 0.1, 0.2, 0.4). ....	63
<b>Figure. III. 9.</b> Transient current density plot of Ni on Cu electrode obtained at 0.8V (vs. Ag/AgCl)).....	65
<b>Figure. III. 10.</b> Nondimensional plot of experimental transients of Ni in comparison with theoretical curves for instantaneous and progressive modes.....	65
<b>Figure. III. 11.</b> Transient current density plot of Zn on Cu electrode obtained at 1.1V (vs. Ag/AgCl)).....	66
<b>Figure. III. 12.</b> Dimensionnels plot (I/I <sub>max</sub> ) <sup>2</sup> vs. (t/t <sub>max</sub> ) of Zn and the theoretical curves (instantaneous and progressive modes).....	67
<b>Figure. III. 13.</b> Chronoamperometry curve of Mn deposited at 1.6 V (vs. Ag/AgCl)) in the sulfate bath. ....	68
<b>Figure. III. 14.</b> Dimensionless plot (I/I <sub>max</sub> ) <sup>2</sup> vs. (t/t <sub>max</sub> ) of Mn obtained in comparison with theoretical curves for instantaneous and progressive modes.....	68

<b>Figure. III. 15.</b> Transient current density plots of Ni-Mn on Cu electrode obtained at various applied potentials (-0.8V, -0.9V, 1V (vs. Ag/AgCl)).....	70
<b>Figure. III. 16.</b> Nondimensional plots of experimental transients of Ni-Mn obtained at various applied potentials (-0.8V, -0.9V, and -1V vs. Ag/AgCl) in comparison with theoretical curves for instantaneous and progressive modes. ....	71
<b>Figure. III. 17.</b> Transient current density plots of Zn-Ni-Mn on Cu electrode obtained at various applied potentials (-1.11V, -1.12V, 1.13V (vs. Ag/AgCl)).....	72
<b>Figure. III. 18.</b> Nondimensional plots of experimental transients of Zn-Ni-Mn obtained at various applied potentials (-1.11V, -1.12V, 1.13V (vs. Ag/AgCl) in comparison with theoretical curves for instantaneous and progressive modes.....	72
<b>Figure. III. 19.</b> Transient current density plots of Ni-Mn on Cu electrode obtained at -1 (vs. Ag/AgCl)) with different [Mn <sup>2+</sup> ] (0.05M, 0.1M, 0.2M and 0.3M). ....	73
<b>Figure. III. 20.</b> Nondimensional plots of experimental transients of Ni-Mn obtained at -1 (vs. Ag/AgCl)) for different [Mn <sup>2+</sup> ] (0.05M, 0.1M, 0.2M and 0.3M) in comparison with theoretical curves for instantaneous and progressive mods. ....	74
<b>Figure. III. 21.</b> Transient current density plots of Zn-Ni-Mn on Cu electrodes obtained at -1.12V (vs. Ag/AgCl)) for different [Mn <sup>2+</sup> ] .....	75
<b>Figure. III. 22:</b> Nondimensional plots of experimental transients of Zn-Ni-Mn coatings obtained with different [Mn <sup>2+</sup> ] (0.05M, 0.1M, 0.3M and 0.4M) in comparison with theoretical curves for instantaneous and progressive modes. ....	75
<b>Figure. III. 23:</b> EDX spectra of electrodeposited Ni-Mn coatings at different [Mn <sup>2+</sup> ] (0.05M, 0.1M, 0.2M, and 0.3 M) at -1V (vs. Ag/AgCl). ....	66
<b>Figure. III. 24:</b> EDX spectra of electrodeposited Zn-Ni-Mn coatings at different [Mn <sup>2+</sup> ] (0.05M, 0.1M, 0.3M, and 0.4 M) at -1.12V (vs. Ag/AgCl). ....	78

<b>Figure IV. 1.</b> SEM micrographs of Ni–Mn coatings for different $[Mn^{2+}]$ at -1V (vs. Ag/AgCl)	79
<b>Figure IV. 2.</b> Histograms of the distribution of particles size in Ni–Mn coatings for different $[Mn^{2+}]$ .	81
<b>Figure IV.3.</b> SEM images of Ni–Mn coatings for various $[Mn^{2+}]$ count at -1.12V (vs. Ag/AgCl).	83
<b>Figure IV. 4.</b> Histograms of the distribution of particles size in Zn–Ni–Mn coatings for different $[Mn^{2+}]$ .	84
<b>Figure IV. 5.</b> XRD patterns of Ni–Mn coatings with different Mn contents.	68
<b>Figure IV. 6.</b> XRD patterns of Zn–Ni–Mn coatings with different Mn contents.	88
<b>Figure IV. 7.</b> Surface morphology of the protective oxide film formed on the surface of Ni–Mn coating (B1).	89
<b>Figure IV.8.</b> Surface morphology of the protective oxide film formed on the surface of Zn–Ni–Mn coating (T1).	90
<b>Figure IV.9.</b> XRD patterns of Ni–Mn coatings after immersed after two weeks of immersion in 3.5 wt. % NaCl.	91
<b>Figure IV. 10:</b> XRD pattern of the corrosion products formed on Zn–Ni–Mn coating (T1) after immersion for two weeks in 3.5 wt.% NaCl testing solution.	92
<b>Figure IV. 11.</b> Potentiodynamic polarization curves of Zn, Ni, and Mn coatings.	93
<b>Figure IV. 12. a).</b> Potentiodynamic polarization curves of Ni–Mn films prepared in the sulfate bath with different Mn coatings were obtained after immersion for 1 hour in a 3.5 wt. % NaCl solution.	95
<b>Figure IV. 13: a)</b> Potentiodynamic polarization curves of Zn–Ni–Mn films prepared in the sulfate bath with different Mn countings which were obtained after immersion.	98

<b>Figure IV. 14.</b> (a) Nyquist plot of Ni–Mn coatings obtained from EIS test in NaCl solution. (b) comparison of the curves. ....	101
<b>Figure IV. 15.</b> (a) Bode-magnitude and (b) Bode-phase plot of Ni–Mn coatings obtained from EIS test in NaCl solution. (c) ECC used to fit Nyquist curves. ....	102
<b>Figure IV. 16.</b> (a) Nyquist plots of Zn–Ni–Mn coatings obtained from EIS test in NaCl solution. (b) comparison of curves. ....	105
<b>Figure IV. 17.</b> (a) Bode-magnitude and (d) Bode-phase plot of Zn–Ni–Mn coatings obtained from EIS test in NaCl solution. (c) ECC used to fit Nyquist curves. ....	105

## Abbreviation index

DRX	X-Ray Diffraction
$E^\circ$	Standard potential
EDS	Energy Dispersive X-ray Spectrometry
ENH	Normal hydrogen electrode
SEM	Scanning electron microscopy
Sol-gel	Solution-Jellification
PVD	Physical Vapor Deposition
CVD	Chemical Vapor Deposition
PLD	pulse laser deposition
wt.%	Percentage musique
2D-3D	Deux-Trois dimensions
T	Temperature ( $^\circ\text{C}$ )
$R_p$	Polarization resistance ( $\text{K}\Omega/\text{cm}^2$ )
$E_{\text{corr}}$	Corrosion potential
$I_{\text{corr}}$	Corrosion current density ( $\mu\text{A}/\text{cm}^2$ ).
$K.\Omega$	Unite
S	Surface
Ni	Nickel
Zn	Zinc
Mn	Manganese
t	Time (sec)
Ag/AgCl	saturated silver chloride electrode
$E_{eq}$	Equilibrium potential
CV	Cyclic voltammetry
CA	Chronoamperometry
$\beta_a$	The right anode constant of Tafel (mV).
$\beta_c$	The right cathodic constant of Tafel (mV).
OCP	open-circuit potential
mi	The mass of the sample before the test,in (g)
mf	The mass of the sample after the test, in (g).



## **Abstract**

Zn, Ni, and Mn are commonly in various industries for their unique properties. The present study, investigation the electrodeposition of Ni–Mn and Zn–Ni–Mn coatings onto a Cu substrate using a sulfate bath at ambient temperature, with a special focus on the effect of deposition potential and  $[\text{Mn}^{2+}]$ , on the coatings' nucleation, chemical composition, surface morphology, crystalline structure, and corrosion resistance. The coatings have been prepared and characterized using various techniques, including, CV and, CA. The nucleation and growth processes were investigated based on Scharifker and Hills' (S-H) model. The investigation demonstrates that the deposition potential and  $[\text{Mn}^{2+}]$  had significant effects on the nucleation mode of Ni–Mn and Zn–Ni–Mn alloys. (EDX) analysis of Ni-Mn coatings indicates that an increase in  $[\text{Mn}^{2+}]$  led to changes in the weight fractions of Ni and Mn in the coatings. The Ni content decreased from 96.9 to 94.1 wt.%, while the Mn content increased from 1.5 to 4.6 wt.%. Sulfur content remained constant at approximately 1.5 wt.%. For Zn–Ni–Mn coatings, the co-deposition behavior was anomalous, with Zn as the major element and its content ranging from 55.7 to 69.7 wt.%. Ni content varied from 37.7 to 22.2 wt.%, while the Mn content increased from 1.6 to 4 wt.%, and the S content decreased slightly from 5 to 3.4 wt.%. (SEM) showed that Ni–Mn coatings were uniform with a cauliflower-like morphology, globular-shaped particles, and a porous cracked surface, while the ternary Zn–Ni–Mn coatings had a compact and dense morphology with good uniformity, no cracks, and pyramidal-shaped particles. The crystal structure of XRD is primarily composed of Ni-Mn solid solution and nickel, exhibiting preferred orientations in the FCC structure, specifically along the (111), (200), and (220) planes. The phase diagrams of Zn–Ni–Mn alloys revealed the presence of both  $\eta$ -Zn and  $\text{NiZn}_3$  phases in Zn–Ni–Mn coatings, which enhance their corrosion resistance. Corrosion resistance was studied using LTP and (EIS). The optimized chemical composition for the most corrosion-resistant Ni-Mn coating was estimated as Ni 96.9 and Mn 1.6. In contrast, the optimized composition for the Zn-Ni-Mn coating included 55.7 wt.% Zn, 37.7 wt.% Ni, and 1.6 wt.% Mn. After 2 weeks of immersion in saline solution, SEM and XRD investigations reveals that the coatings offer effective cathodic protection through the formation of a protective oxide layer consisting of  $\text{MnO}_2$  oxide and Ni (OH)Cl<sub>2</sub> hydroxide. exhibiting a non-uniform, with highly porous microstructure, and Zn–Ni–Mn coating showed the formation of  $\text{Zn}_5(\text{OH})_8\text{Cl}_2$ , ZnO, and  $\text{ZnMn}_2\text{O}_4$  oxide and hydroxide chloride phases with a non-homogeneous highly porous morphology.

**Keywords:** Ni-Mn, Zn-Ni-Mn coatings, electrodeposition, corrosion resistance, S-H, nucleation, growth.

## **Résumé :**

La corrosion des métaux est le résultat de l'interaction du métal avec leur environnement. Les éléments zinc (Zn), nickel (Ni) et manganèse (Mn) peuvent être utilisés comme revêtements sacrificiels. Le travail présent porte sur l'électrodéposition de couches minces de Ni-Mn et Zn-Ni-Mn sur un substrat en Cu à l'aide d'un bain de sulfate à température ambiante. Le travail est basé spécifiquement sur l'étude de l'effet du potentiel de déposition et de la concentration des ions manganèse  $[Mn^{2+}]$  sur la nucléation, la composition chimique, la morphologie de surface, la structure cristalline et la résistance à la corrosion des revêtements. Les revêtements ont été préparés et caractérisés à l'aide de diverses techniques, y compris la voltamétrie cyclique (CV) et la chronoampérométrie (CA). Les processus de nucléation et croissance ont été étudiés en se basant sur le modèle de Scharifker et Hills (S-H). L'étude démontre que le potentiel de dépôt et  $[Mn^{2+}]$  ont des effets significatifs sur le mode de nucléation des alliages Ni-Mn et Zn-Ni-Mn. L'analyse (EDX) des revêtements Ni-Mn indique qu'une augmentation de  $[Mn^{2+}]$  entraîne des changements dans les fractions massiques de Ni et Mn dans les revêtements. La teneur en Ni est passée de 96,9 à 94,1 %, tandis que la teneur en Mn a augmenté de 1,5 à 4,6 %. La teneur en soufre est restée constante autour de 1,5 %. Pour les revêtements Zn-Ni-Mn, le comportement de co-déposition était anormal, avec le Zn comme élément principal et sa teneur variant de 55,7 à 69,7 %. La teneur en Ni a varié de 37,7 à 22,2 %, tandis que la teneur en Mn a augmenté de 1,6 à 4 %, et la teneur en soufre a légèrement diminué de 5 à 3,4 % en poids. La microscopie électronique à balayage (SEM) a montré que les revêtements Ni-Mn étaient uniformes avec une morphologie en forme de chou-fleur, des particules globulaires et une surface poreuse et fissurée, tandis que les revêtements ternaires Zn-Ni-Mn avaient une morphologie compacte et dense avec une bonne uniformité, sans fissures, et des particules en forme de pyramide. La structure cristalline de la diffraction des rayons X (XRD) est principalement composée d'une solution solide de Ni-Mn et de nickel, présentant des orientations préférées dans la structure FCC, spécifiquement le long des plans (111), (200) et (220). Les diagrammes de phase des alliages Zn-Ni-Mn ont révélé la présence des phases  $\eta$ -Zn et  $NiZn_3$  dans les revêtements Zn-Ni-Mn, ce qui améliore leur résistance à la corrosion. La résistance à la corrosion a été étudiée par LTP et de la spectroscopie d'impédance électrochimique (EIS). La composition chimique optimisée pour le revêtement Ni-Mn le plus résistant à la corrosion a été établie à Ni 96,9 % et

Mn 1,6 %, la composition optimisée pour le revêtement Zn-Ni-Mn comprenait 55,7 % de Zn, 37,7 % de Ni et 1,6 % de Mn. Après 2 semaines d'immersion dans une solution saline, les résultats de MEB et DRX indiquent que les revêtements assurent une protection cathodique efficace grâce à la formation d'une couche d'oxyde protectrice composée d'oxyde de  $MnO_2$  et d'hydroxyde de  $Ni(OH)Cl_2$ , présentant une structure microscopique non uniforme, hautement poreuse, et le revêtement Zn-Ni-Mn présentant la formation des phases d'oxyde et d'hydroxyde de chlorure de  $Zn_5(OH)_8Cl_2$ ,  $ZnO$  et  $ZnMn_2O_4$  avec une morphologie non homogène et poreuse.

Mots-clés : Ni-Mn, Zn-Ni-Mn, électrodéposition, résistance à la corrosion, S-H, nucléation, croissance

## المخلص

تستخدم العناصر الترابية مثل الزنك (Zn) والنيكل (Ni) والمنجنيز (Mn) في العديد من الصناعات نظراً لخصائصها الممتازة. يتناول العمل الحالي الترسيب الكهربائي لطبقات رقيقة من سبائك النيكل والمنجنيز (Ni-Mn) والزنك والنيكل والمنجنيز (Zn-Ni-Mn) على ركيزة من النحاس باستخدام حمام كبريتات في درجة حرارة الغرفة. يهدف هذا العمل إلى دراسة تأثير جهد الترسيب وتركيز أيونات المنجنيز  $[Mn^{2+}]$  على تطور بنية الطلاء وبشكل خاص يهدف إلى دراسة تأثير تركيز أيونات المنجنيز على التركيب الكيميائي، شكل السطح، البنية البلورية، ومقاومة التآكل لكل من سبائك النيكل والمنجنيز (Ni-Mn) والزنك والنيكل والمنجنيز (Zn-Ni-Mn) وتم تحضير وتوصيف الأغشية باستخدام تقنيات متعددة، بما في ذلك CV و CA. تمت مقارنة البيانات التجريبية للـ CA بالنموذج النظري لـ Scharifker و Hills (S-H). أظهرت الدراسة أن جهد الترسيب و  $[Mn^{2+}]$  له تأثيرات كبيرة على نمط ترسيب سبائك Ni-Mn و Zn-Ni-Mn. ويشير تحليل (EDX) لأغشية Ni-Mn إلى أن زيادة في  $[Mn^{2+}]$  أدت إلى تغييرات في كمية النيكل والمنجنيز في طلاء. انخفض محتوى النيكل من 96.9 إلى 94.1 وزن٪، بينما ارتفع محتوى المنجنيز من 1.5 إلى 4.6 وزن٪. بقي محتوى الكبريت ثابتاً عند حوالي 1.5 وزن٪. بالنسبة لأغشية Zn-Ni-Mn، كان سلوك الترسيب متغيراً، واعتبر الزنك كعنصر رئيسي لأن نسبة محتواه تتراوح بين 55.7 إلى 69.7 وزن٪. واختلف نسبة النيكل من 37.7 إلى 22.2 وزن٪، في حين ارتفع نسبة المنجنيز من 1.6 إلى 4 وزن٪، وانخفض نسبة الكبريت قليلاً من 5 إلى 3.4 وزن٪. أظهرت (SEM) أن أغشية Ni-Mn كانت متجانسة مع سطح يشبه القرنبيط، وجسيمات على شكل كرات، و سطح مسامي متصدع، بينما كان لدى أغشية Zn-Ni-Mn سطح ومتجانس مع عدم وجود شقوق وجسيمات على شكل هرمي. كذلك اثبت نتائج حيود الأشعة السينية XRD ان البنية البلورية لـ Ni-Mn تتكون أساساً من النيكل FCC الذي ظهر بعدت توجهات مفضلة (111)، (200)، و(220). أظهرت نتائج سبائك Zn-Ni-Mn وجود المركبات  $\eta$ -Zn و  $NiZn_3$  في أغشية Zn-Ni-Mn، مما يعزز من مقاومة التآكل لديها. وقد تمت دراسة مقاومة التآكل السبائك باستخدام LPT و (EIS). تم تحديد التركيبة الكيميائية المثلى لطلاء Ni-Mn الأكثر مقاومة للتآكل عند 96.9% نيكل و 1.6% منجنيز، بينما كانت التركيبة المثلى لطلاء Zn-Ni-Mn تحتوي على 55.7% زنك، و 37.7% نيكل، و 1.6% منجنيز. بعد أسبوعين من الغمر في محلول ملحي، أظهرت نتائج SEM و XRD أن العينات توفر حماية كاثودية فعالة من خلال تكوين طبقة أكسيدية واقية تتألف من أكسيد  $MnO_2$  وهيدروكسيد  $Ni(OH)_2$ ، مع وجود سطح غير متجانس ووجود مسامات بشكل كبير، وأظهرت أغشية Zn-Ni-Mn تكوين مركبات أكسيدية وهيدروكسيدية ك  $Zn_5(OH)_8Cl_2$  و  $ZnO$  و  $ZnMn_2O_4$

الكلمات المفتاحية: طبقات Ni-Mn، Zn-Ni-Mn، الوضع الكهربائي، مقاومة التآكل، S-H، التئوي، التقاطع.

### **General Introduction**

Corrosion is the natural deterioration of materials resulting from reactions with the surrounding environment and various factors [1–3]. The capacity to resist corrosion is essential in evaluating a material's stability and durability, particularly in industrial applications [4, 5]. Despite numerous efforts and extensive research, a definitive solution to corrosion remains elusive. Nowadays, several methods are available for preventing corrosion, such as cathodic protection, protective coatings, alloying, and galvanization. In particular, protective coatings are recognized as a common and effective way to prevent corrosion and maintain the structural integrity of metal components [6, 7]. These coatings create a barrier between the material and the environment, offering strength and corrosion protection. It is well known that the characteristics of these coatings are highly sensitive to production methods. In this sense, electrodeposition is a practical, simple, and versatile process used to prepare protective coatings with high corrosion resistance. This method provides a high level of precision and control by allowing adjustment of several parameters like current density, applied potential, and bath composition, enabling the production of coatings with specific and desired properties [8]. The coatings prepared by this method exhibit excellent adhesion to substrates, contributing to enhanced durability. This process is economically efficient, minimizing material wastage and promoting resource optimization.

Among numerous metallic protective coatings, Ni–Mn alloys shine in various excellent characteristics, notably excelling in corrosion resistance. The properties and formation of Ni–Mn coatings are significantly influenced by the Mn ions concentration in the bath,  $[\text{Mn}^{2+}]$ , due to its high reduction–oxidation potential ( $E_{\text{Mn}/\text{Mn}^{2+}} = -1.85\text{V}$  vs. SHE) which is considerably higher than that of Ni ( $E_{\text{Ni}/\text{Ni}^{2+}} = -0.257\text{V}$  vs. SHE) [9]. The variation in standard electrode potentials is regarded as a major challenge in Ni–Mn alloy deposition [10]. Furthermore, Ni–Mn coatings encounter several drawbacks due to the induced hydrogen evolution reaction during the deposition process [11, 12]. Moreover, it is well established that Zn plays a paramount role in protecting metals from corrosion, due to its great propensity for corrosion and relatively low potential ( $E_{(\text{Zn}^{2+}/\text{Zn})} = -0.761$  vs. SHE) [13, 14]. The Zn based coatings react with the surrounding environment, leading to the formation of a protective layer, such as zinc oxide and zinc hydroxide. These layers serve as a barrier, shielding the metal's surface from moisture and oxygen influx. In addition, several studies revealed that Zn–Ni–Mn alloys exhibit superior corrosion resistance compared to Zn–Ni, Ni–Mn, and Zn–Mn alloys

## *General introduction*

---

[15–18]. These coatings deposition depended on several factors especially Mn content and the deposition potential.

The objective of this work is to study the Ni–Mn and Zn–Ni–Mn deposition on a Cu substrate, using different  $[\text{Mn}^{2+}]$  in the bath. The influence of  $[\text{Mn}^{2+}]$  and deposition potential to improve the deposits efficiency is studied by (CV) and (CA) techniques. The surface morphology, chemical composition, and crystalline structure of the obtained coatings are respectively followed by (SEM), (EDX) and (XRD) techniques. Additionally, the study evaluates the corrosion resistance of the deposits in a chloride environment through electrochemical analysis by linear polarization plots (LPT), and (EIS) techniques.

This thesis manuscript is structured in four chapters:

1. The first chapter presents a theoretical background review in electrochemistry relevant to our study, focusing on the principles of electrocrystallization and codeposition of thin films. It also explores various corrosion and protection methods. Furthermore, the chapter provides an extensive review on Ni, Mn and Zn, presenting previous works on the Ni–Mn and Zn–Ni–Mn coatings.
2. In the second chapter, the focus is on introducing the experimental setup and operating conditions utilized in both the synthesis and characterization of the deposited coatings. A detailed description is given on the electrochemical techniques, namely CV, CA, LPT and EIS. Furthermore, the theoretical principles underlying the characterization methods, including SEM, EDX, and XRD are explained.
3. The chapter three is dedicated to the electrochemical characterization of the deposited coatings using CV and CA. Subsequently, the experimental results of the influence of  $[\text{Mn}^{2+}]$  and deposition potential on the nucleation and growth mechanism of the coatings are analyzed. The effect of  $[\text{Mn}^{2+}]$  on the Ni–Mn coating's chemical composition is also presented.
4. In chapter four, the significant experimental outcomes related to the influence of  $[\text{Mn}^{2+}]$  on the morphological, structural, as well as the alloy's ability to resist corrosion are presented and analyzed.

This thesis concludes with a general statement that highlights the key findings and potential directions for further research.

## *General introduction*

---

### References

- [1] N. Perez, “*Electrochemistry Science and Corrosion*”,(2004), *Springer Nature*,. ISBN 978-3-319-24847-9 (eBook). Switzerland, 20166.
- [2] Y. Ji, Y. Xu, B. Zhang, Y. Behnamian, D. Xia, and W. Hu, “Review of micro-scale and atomic-scale corrosion mechanisms of second phases in aluminum alloys,”(2021), *Trans. Nonferrous Met. Soc. China*, vol. 31, no. 11, pp. 3205–3227.
- [3] K. A. Emelyanenko, A. M. Emelyanenko, and L. B. Boinovich, “Laser Obtained Superhydrophobic State for Stainless Steel Corrosion Protection, a Review,” (2023), *Coatings*, v. 13, no. 1.
- [4] H. M. Hussein Farh, M. E. A. Ben Seghier, R. Taiwo, and T. Zayed, “Analysis and ranking of corrosion causes for water pipelines: a critical review,” (2023), *npj Clean Water*, v. 6, no. 1, pp. 1–17.
- [5] N. Eliaz, K. Venkatakrishna, and A. C. Hegde, “Surface & Coatings Technology Electroplating and characterization of Zn – Ni , Zn – Co and Zn – Ni – Co alloys,” (2010), *Surf. Coat. Technol.*, v. 205, no. 7, pp. 1969–1978,
- [6] N. Loukil and M. Feki, “Review — Zn – Mn Electrodeposition : A Literature Review Review — Zn – Mn Electrodeposition : A Literature Review,” (2020), *J. Electrochem. Soc.* 167 022503
- [7] P. P. Barreiros and M. J. M. Pires, “Analysis of the electrodeposition process of Fe-Mn films from sulfate electrolytes,” (2020), *Mater. Res. Express*, v. 7, no. 1, ,
- [8] F. Yang, L. Jiang, X. Yu, Y. Lai, and J. Li, “Hydrometallurgy The effects of SeO<sub>2</sub> additive on Mn electrodeposition on Al substrate in,” (2020), v. 192, no. January, pp. 1–10,
- [9] J. Guo, X. Guo, S. Wang, Z. Zhang, J. Dong, and L. Peng, “Applied Surface Science Effects of glycine and current density on the mechanism of electrodeposition , composition and properties of Ni – Mn films prepared in ionic liquid,” (2016), *Appl. Surf. Sci.*, v. 365, pp. 31–37,
- [10] P. Díaz-Arista and G. Trejo, “Electrodeposition and characterization of manganese coatings obtained from an acidic chloride bath containing ammonium thiocyanate as an additive,” (2006), *Surf. Coatings Technol.*, v. 201, no. 6, pp. 3359–3367.
- [11] F. Yang, L. Jiang, X. Yu, Y. Lai, and J. Li, “The effects of SeO<sub>2</sub> additive on Mn electrodeposition on Al substrate in MnSO<sub>4</sub>-(NH<sub>4</sub>)<sub>2</sub>SO<sub>4</sub>-H<sub>2</sub>O solution,” (2020),



## *General introduction*

---

- Hydrometallurgy*, v. 192, no. January, pp. 1–10.
- [12] S. K. Padhy, B. C. Tripathy, and A. Alfantazi, “Effect of sodium alkyl sulfates on electrodeposition of manganese metal from sulfate solutions in the presence of sodium metabisulphite,” (2018), *Hydrometallurgy*, v. 177, no. February, pp. 227–236,
- [13] Z. I. Ortiz, P. Díaz-Arista, Y. Meas, R. Ortega-Borges, and G. Trejo, “Characterization of the corrosion products of electrodeposited Zn, Zn-Co and Zn-Mn alloys coatings,” (2009). *Corros. Sci.*, v. 51, no. 11, pp. 2703–2715,
- [14] H. Kazimierzak, A. Hara, A. Bigos, and P. Ozga, “Electrochimica Acta Electrodeposition of Zn-Mn-Mo layers from citrate-based aqueous electrolytes,” (2016), *Electrochim. Acta*, v. 202, pp. 110–121,
- [15] F. H. Assaf, M. M. Abou-Krishna, O. K. Alduaij, A. M. A. El-Seidy, and A. A. Eissa, “The effect manganese concentration on the corrosion resistance and physical properties of Zn-Ni-Mn alloy films produced by electrodeposition,” (2015), *Int. J. Electrochem. Sci.*, v. 10, no. 8, pp. 6273–6287,.
- [16] B. Abedini, N. Parvini, S. Yazdani, and L. Magagnin, “Surface & Coatings Technology Structure and corrosion behavior of Zn-Ni-Mn / Zn e Ni layered alloy coatings electrodeposited under various potential regimes,” (2019), *Surf. Coat. Technol.*, vol. 372, no. March, pp. 260–267,
- [17] B. ABEDINI, N. PARVINI AHMADI, S. YAZDANI, and L. MAGAGNIN, “Electrodeposition and corrosion behavior of Zn–Ni–Mn alloy coatings deposited from alkaline solution,” (2020), *Trans. Nonferrous Met. Soc. China (English Ed.)*, vol. 30, no. 2, pp. 548–558,
- [18] K. Chat-Wilk, E. Rudnik, and G. Włoch, “Effect of Chloride and Sulfate Ions on Electrodeposition and Surface Properties of Alloys Produced from Zinc-Nickel-Manganese Gluconate Baths,” (2022), *J. Electrochem. Soc.*, vol. 169, no. 9, p. 092515,

# *Chapter I*

## *Literature Review*

---

*In this chapter, the electrodeposition process is presented through a comprehensive description of electrocrystallization and codeposition phenomena and an exploration of nucleation and crystal growth in liquid media. Subsequently, the theoretical concepts related to alloy corrosion are considered. Finally, the chapter provides an overview of the literature on the crystalline structure, physicochemical, and electrochemical properties of Ni–Mn, Zn–Ni–Mn alloys, and the pure elements Zn, Ni, and Mn.*

---

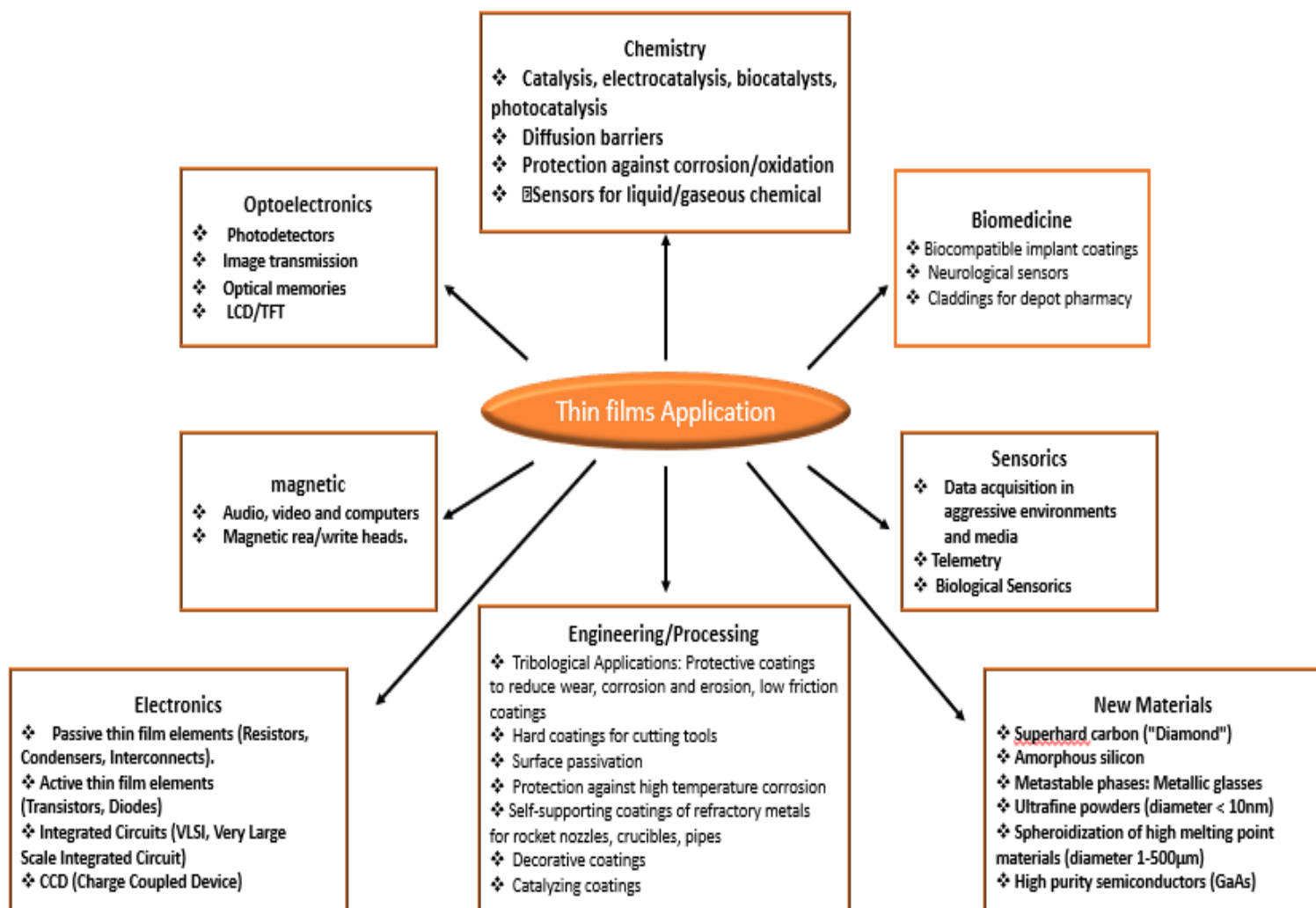
## **I.1. Thin films**

### ***I.1.1. Definition***

Thin films are a class of materials with a thickness ranging from a few nanometers to many micrometers. They are often produced by thin film's deposition methods, where the material is deposited onto a substrate through a variety of processes such as chemical vapor deposition, physical vapor deposition, sputtering...etc [1]. Thin films can be prepared using a diverse array of materials, such as metals, alloys, intermetallic compounds, refractory compounds (oxides, carbides, and nitrides), and polymers. The allure of these low-dimensional materials lies in their novel electrical, optical, chemical, and magnetic properties, which are frequently more desirable than those exhibited by bulk materials with the same composition [2–4].

### **I.1.2 Thin films properties and applications**

Thin films are materials with special physical, chemical, and electrical characteristics which render them practical in a variety of applications, including electronics, optoelectronics, energy production, and sensors (**Figure I. 1**) [5–8]. Thin films exhibit distinct optical properties, such as high reflectivity, transparency, and absorbance, which can be adjusted by modifying the film's thickness and composition [6]. Specifically, the electrical properties of thin films, including high conductivity, low resistance, and high dielectric constant, are deposition conditions dependent. Thin-film mechanical characteristics, such as rigidity, flexibility, and durability, can be customized by adjusting the deposition method, material composition, and thickness [9]. Thin films can also possess good chemical stability, high corrosion resistance and exceptional magnetic properties [10].

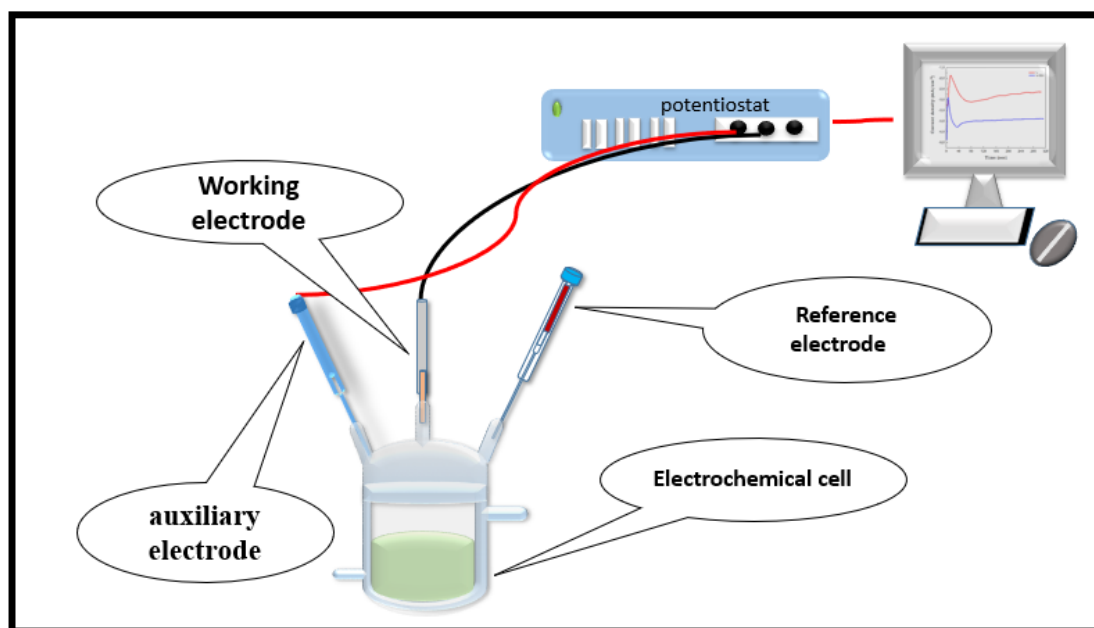


**Figure I.1.** Schematic representation of different applications of thin films [8].

## I.2. Electrodeposition

Electrodeposition is a flexible low cost technique largely used to produce thin films [9] that involves passing an electric current (charge transfer reaction) through an electrochemical cell containing the reagents to be deposited, which may be metals, oxides, other minerals, or organic molecules. It has been applied for over 200 years since it was first used in 1805, by Luigi Brugnatelli, to produce decorative and protective coatings [11]. Electrodeposition frequently aims to give the working electrode new properties, such as chemical stability, roughness, corrosion resistance, appearance (matte, semi-gloss, and gloss, satin...), optical properties, weldability, conductivity, hardness, ductility, resistance to wear, abrasion and friction, etc. Additionally, it is a method that provides a variety of advantages over physical techniques including its ease of use, ability to operate at room temperature and atmospheric pressure, and

capacity to adjust the properties of the deposited films, such as morphology, particles size, and thickness [12]. Electrodeposition is used to create solid thin films on the working electrode's surface (substrate) by electrochemical reduction of the metal ions of an aqueous solution through the application of electric current. The process involves several steps: (i) the substrate's surface cleaning and polishing, (ii) the preparation of the electrolytic solution containing metal ions, (iii) immersion of the substrate in the solution, and (iv) application of the electric current to reduce the metal ions onto the substrate. The deposition parameters, such as deposition potential, current density, electrolyte composition, pH, and temperature, are carefully controlled to achieve the desired thickness and features of the thin films. Electrodeposition technique has been largely used to deposit a wide range of metals and alloys on various substrates [13]. The electrodeposition setup, shown in **Figure I. 2**, consists of three electrodes (working electrode, reference electrode, and auxiliary electrode) immersed in the solution containing the metal ions to be deposited and connected to a potentiostat which controls the deposition process. The current flows between the working electrode and the auxiliary electrode. The reference electrode is used as the standard for measuring the potential [12].



**Figure I.2.** Schematic representation of the electrodeposition equipment.

The applied potential ( $E$ ) and the current density ( $I$ ) are the main factors governing this process. In the case of electroplating, two modes are used to supply energy and maintain the electrochemical process: the galvanostatic mode, which imposes a current on the system and

records the electrode potential over time (chronopotentiometry), and the potentiostatic mode, which imposes a potential with the possibility of following up the current as a function of time (chronoamperometry).

### I.2.1. Electrodeposition principles

Metal electroplating involves the reduction of metal ions from a solution onto a conductive substrate. In a simple electrochemical system, where a metal M electrode is submerged in a liquid solution with metal ions  $M^{n+}$ , equilibrium is established through electron transfer at the metal/solution interface. The obtained atoms subsequently deposit on the electrode surface.



The  $M^{n+}/M$  couple's normal redox potential and the  $M^{n+}$  species' activity in the solution are dependent on the electrode's potential  $E_{eq}$ , which is given by the Nernst equation.

$$E_{eq} = E_0 + \frac{RT}{nF} \ln a_{M^{n+}} \quad (\text{I. 2})$$

$E_0$ : Standard electrode potential (in volts)

R: Gas constant (8.314 J/mol·K)

T: Temperature in Kelvin (K)

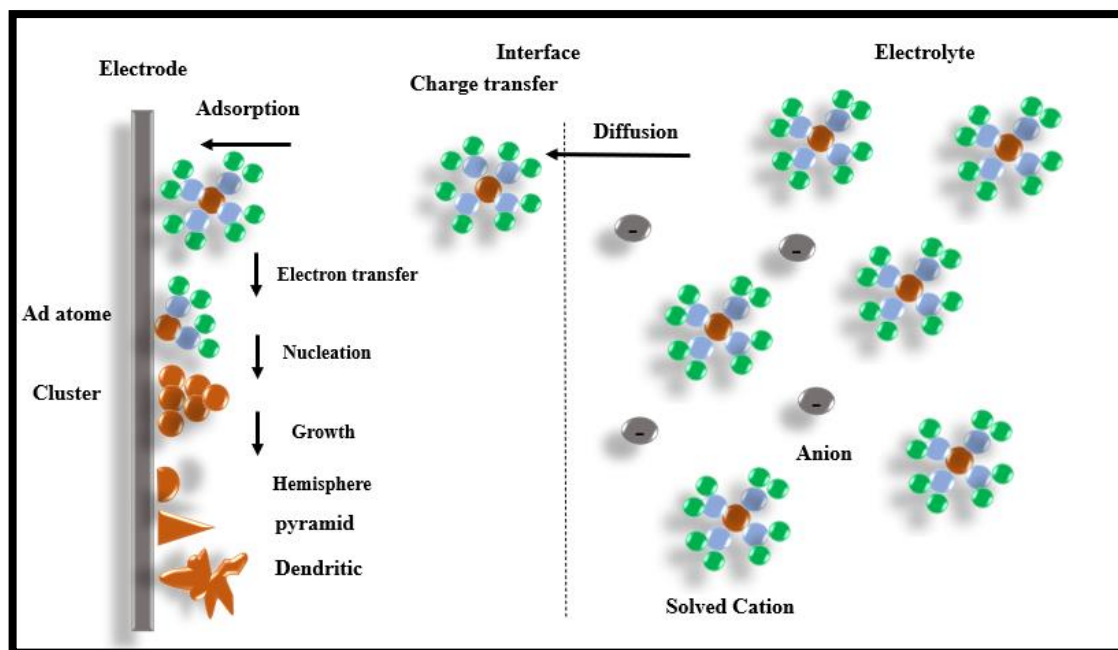
n: Number of electrons transferred in the redox reaction

F: Faraday's constant (96,485 C/mol)

$\ln a_{M^{n+}}$ : Natural logarithm of the activity of the metal ion  $M^{n+}$

### I.2.2 Electrodeposition mechanism

The electroplating process, involving the metal's deposition on a substrate, is a complex phenomenon comprising a series of sequential elementary steps. The overall electrochemical reactions, involves both charge transfer and the transport of matter. To establish a relationship between current (I), potential (E), and solution concentrations of Ox and Red, one must consider both aspects [14]. The different mechanisms involved in electrodeposition are summarized in figure I. 3.



**Figure I.3.** Different mechanisms involved during electrodeposition process [15].

### *1.2.2.1. Mass transfer*

The mass transfer involves the transport of ions through the electrolyte solution toward the electrodes, influencing the rate and uniformity of metal deposition. Factors such as concentration gradients, diffusion, and convection play significant roles in mass transfer process during electrochemical reactions.

#### *1.2.2.1.1 Diffusion*

In the context of electroplating, diffusion refers to the movement of ions through the electrolyte solution toward the electrode (cathode). The spontaneous movement is triggered by the emergence of a concentration gradient resulting from consumption and/or reduced and deposited as a solid metal layer. This process is crucial for ensuring a uniform and controlled deposition of the metal onto the substrate.

#### *1.2.2.1.2. Migration*

Migration is the displacement of charged particles in response to an applied electric field. The application of voltage in an electrochemical cell induces an electric field, compelling ions in

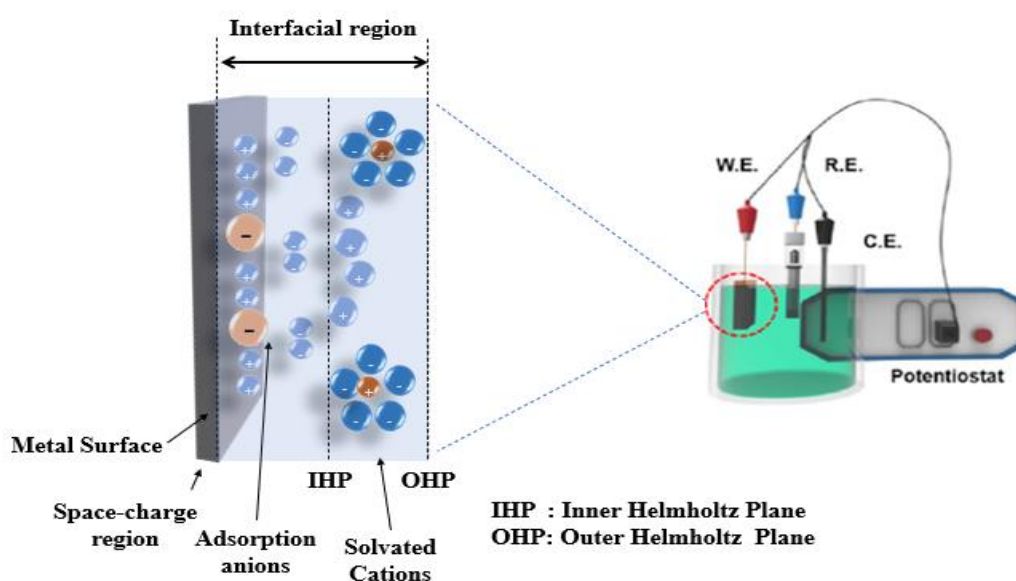
the electrolyte solution to move toward the electrodes. Cations migrate towards the negatively charged cathode, while anions move towards the positively charged anode.

### *1.2.2.1.3. Convection*

Within the framework of electrodeposition, convection signifies the mobilization of the electrolyte solution near the electrode, initiated by mechanical actions such as stirring or agitation. This dynamic fluid motion serves a pivotal role in upholding a consistent concentration of ions around the electrode, amplifying mass transfer, and facilitating a homogeneous deposition of metal. The adept management of convection is imperative to prevent concentration gradients, thus mitigating the risk of uneven coatings in the electrodeposition process.

### *1.2.2.2. Charge transfer*

The mechanism of charge transfer is rather complicated, corresponding to the association of the electrons of the metal with the ions located in the double layer (area very close to the electrode surface) and more precisely in the Helmholtz double electronic layer. As a result, the adatoms diffuse onto the surface and incorporated to an active site (Figure I.4). The most widely theory accepted is of Bockris [16] which explains that adatoms migrate by surface diffusion towards an imperfection in the crystal lattice in order to be incorporated. It is only after having reached these crystal sites that the adatoms dissolve and discharge, they are then incorporated into the crystal lattice [17].



**Figure I. 4.** Diagram of the Electrode–Electrolyte Interface



### I.2.2.3. Crystallization

The initial stage in the process is the development of germs, which is followed by their growth into crystals. During this phenomenon, new crystals will develop through consolidation of the crystalline structure already forming. If the seeds' rate of growth is slower than their rate of germination, tiny crystals will make up the deposit. The competition between these two processes constitutes a factor determining the morphology and microstructure of the deposits [18].

### I.2.4. Nucleation

The metal deposition process, in theory, relies on the Butler–Volmer relationship, which describes how the current density ( $i$ ) changes with the overpotential ( $\eta$ ) applied to the metal substrate. This relationship holds true when the electrochemical process is controlled by charge transfer and assumes a uniformly homogeneous surface, resulting in a uniform current density across the entire solid surface [14].

$$i = i_0 \left[ e^{(1-\alpha)n\frac{F}{RT}\eta} - e^{-\alpha n\frac{F}{RT}\eta} \right] \quad (\text{I. 3})$$

Nucleation plays an essential role in the process of electrodeposition. Effectively, during the initial stage of deposition, germs are formed as ad-ions (ad-atoms) on the surface come together to form clusters through diffusion. The shape of these germs is determined by the most energetically favorable arrangement, which is influenced by two factors: the energy required for atom transfer to the surface and the energy required to create the germ's surface. Ultimately, the formation of a stable crystal structure is dependent on these parameters [9].

#### I.2.4.1. Nucleation kinetics

The rate of formation of new stable growth centers is governed by first-order kinetics, which can be described by the following equation that relates the number of active growth sites ( $N_c$ ) to time ( $t$ ).

$$N_c = N_0 [1 - \exp(-k_n t)] \quad (\text{I.4})$$

$N_c$  : the number of active growth sites,  $t$ : the time and,  $K_n$  : the nucleation rate constant.

The number of active growth sites ( $N_c$ ) is influenced by several factors such as applied potential, concentration of different species, and the nature of substrate. Based on this equation, two primary modes of nucleation during electrodeposition can be distinguished: instantaneous and progressive types.

#### ***1.2.4.2. Instantaneous nucleation mode***

When the nucleation rate is high, the active nucleation sites on the surface become fully occupied during the initial stages of deposition. This phenomenon is referred to instantaneous nucleation and can be mathematically described by equation (I.5).

$$N_c = N_0 \quad (\text{I. 5})$$

If the constant  $K_n$  is extremely high, then all available sites are filled as soon as a potential jump is applied to the electrode at  $t = 0$ .

#### ***1.2.4.3. Progressive nucleation mode***

When the nucleation rate is slow, nuclei gradually develop on the surface sites over time. The following equation may be used to quantitatively characterize this kind of nucleation.

$$N_c = N_0 k_n t \quad (\text{I. 6})$$

When the nucleation rate is low corresponding to small values of  $K_n$ , only a portion of the available sites will be filled at the beginning of the process, while the rest will be filled gradually over the time. This dependence on the nucleation rate becomes particularly important when considering that  $K_n$  can be experimentally controlled by adjusting the applied potential to the cathode.

#### ***1.2.4.4. Scharifker–Hills model***

Scharifker–Hills (S–H) developed a theoretical model to characterize the nucleation process [19], which can be categorized into two distinct types: instantaneous and progressive. In the instantaneous nucleation mode, nuclei grow rapidly on a small number of active sites, and all clusters are activated simultaneously. Conversely, the progressive nucleation mode involves the gradual formation of nuclei on multiple active sites.

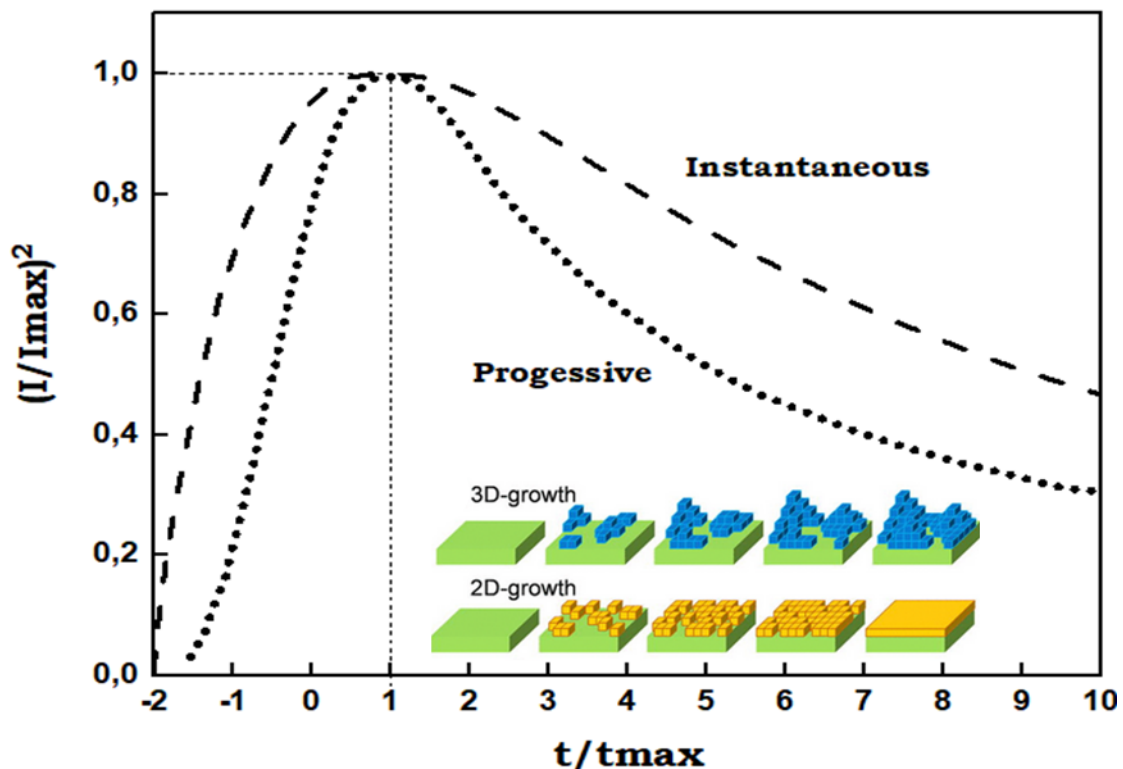
These two nucleation modes can be described using the following equation [19] :

$$\text{Instantaneous nucleation: } \frac{I^2}{I_m^2} = \frac{1.9542}{(t/t_m)} \left( 1 - \exp \left[ -1.2564 \left( \frac{t}{t_m} \right) \right] \right)^2. \quad (\text{I. 7})$$

$$\text{Progressive nucleation: } \frac{I^2}{I_m^2} = \frac{1.2254}{(t/t_m)} \left( 1 - \exp \left[ -2.3376 \left( \frac{t}{t_m} \right)^2 \right] \right)^2. \quad (\text{I. 8})$$

Where  $I$  represents the current density,  $I_m$  is the maximum current density,  $t$  is the time, and  $t_m$  is the time corresponding to the maximum current density.

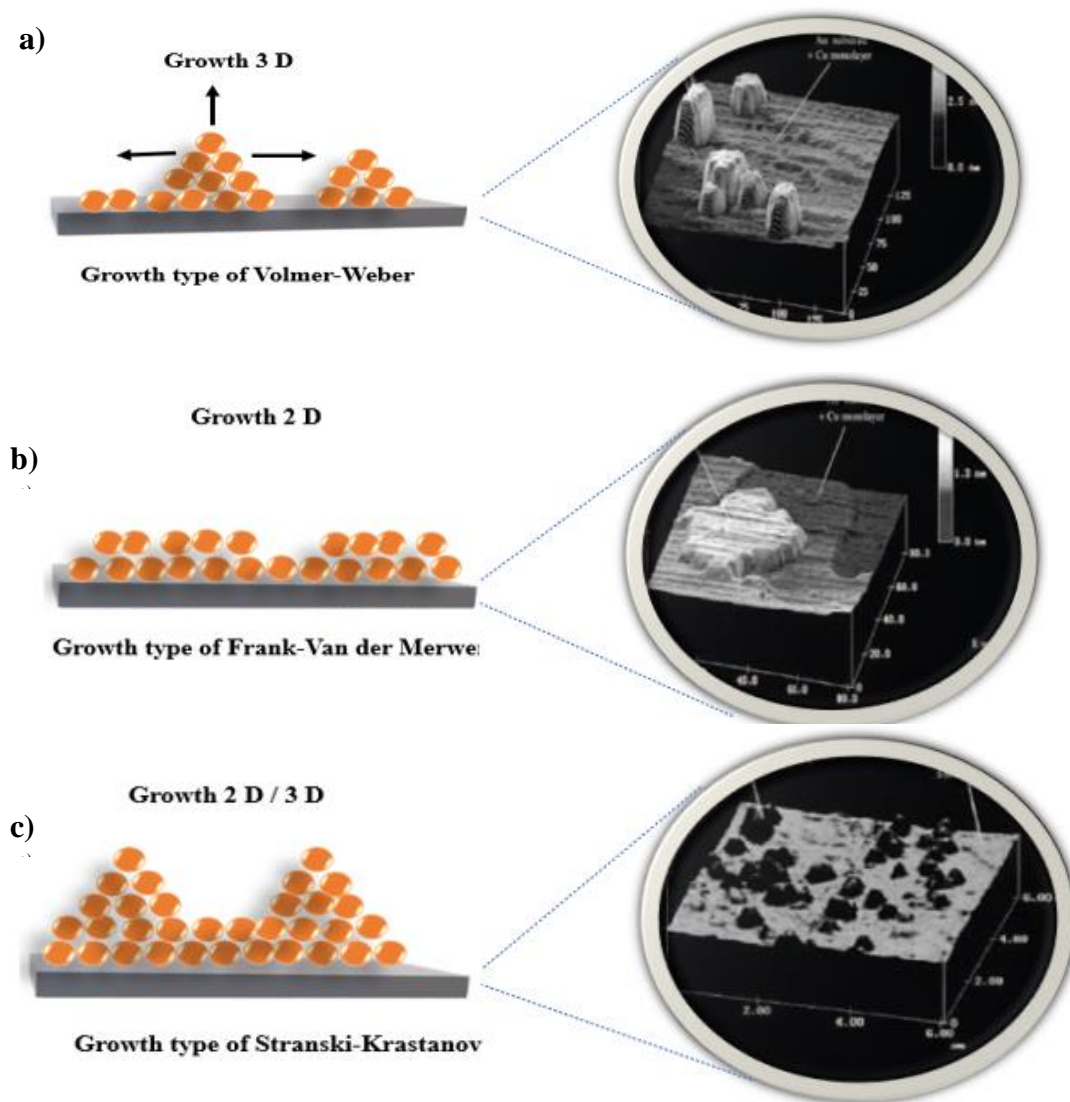
Figure I.5 displays the normalized current transients generated by this model. To validate the model, experimental data are used to plot similar normalized transients, which are then compared to those predicted by the theoretical model. This comparison allows for the determination of the nucleation mode and growth mechanism in the electroplating method [20].



**Figure I. 5.** Normalized Transients for Progressive and Instantaneous Nucleation.

### I.2.5. Growth modes

Nucleation and growth are critical stages in the electroplating process. They determine the appearance and structure of the deposited materials, which is affected by the crystal growth pattern [16]. The initial phase of forming a new layer on a substrate is characterized by 3D nucleation and growth, which typically involves adsorption reactions and the formation of low-dimensional structures that preferentially localize on the uneven surfaces of the substrate [17]. As a result, growth modes can be classified into three categories, as depicted in Figure I.6.



**Figure I.6.** Models of thin films development types with examples of : a) AFM image of a copper deposit on a conductive surface of polypyrene, b) AFM image of Copper deposition on a Gold substrate, c) AFM image of Copper deposition on a Gold substrate [17].

### ***1.2.5.1. 2D growth mode (Frank–Van der Merwe mechanism)***

This type of growth is generally encountered when the metal and substrate are of the same chemical nature. The deposit spreads over the entire surface of the substrate, each layer is fully completed before another layer begins to form. The 2D growth mode occurs when the adsorption energy of the metal on the substrate is higher than the cohesion energy of the metal.

### ***1.2.5.2. 3D growth mode (Volmer–Weber mechanism)***

In this case, the deposit does not spread over the entire surface of the substrate, three-dimensional growth develops. The full coverage of the substrate's surface necessitates the deposition of multiple atomic planes. This occurs when the surface energy (adsorption) of the metal atoms on the substrate is less than the surface energy (cohesion) of the metal. This growth mode can be exploited to create nanostructures.

### ***1.2.5.3. Growth mode 2D followed by 3D growth (Stranski–Krastanov mechanism)***

The first atomic layer covers the surface of the substrate according to the 2D growth mode. The growth of subsequent layers continues in the form of islands.

## **1.2.6 Parameters influencing the deposits**

Different factors can affect the electroplating process of alloys. These parameters play an essential role in determining the performance and quality of the deposited films, including the crystal structure, morphology, roughness, composition, and more [14]. Among these are:

- *Temperature*
- *PH*
- *Hydrodynamic conditions (agitation)*
- *Composition and characteristics of the bath*
- *Additives*
- *The substrate's characteristics and surface*
- *Electrical parameters (potential, current)*
- *Electrical responses*
- *Distance between cathode and anode.*

### **I.3. Metal co–deposition**

The co–deposition of metals results from a co–reduction of two metals present in the solution in ionic form on the working electrode and able to crystallize in one of the phases shown in their phase diagram. There are different types of codeposition distinguished by various mechanisms [21– 23].

#### **I.3.1. Normal or regular Co–deposition**

This type of co–deposition is generally observed when the redox potentials of the two metals are far from each other. In this case, the co–deposition of the metals does not form a solid solution. In this type, and as the name indicates "normal" the two metallic elements, are deposited in the order of their redox potentials, the more noble metal is deposited preferentially. This is the case of the Zn–Mn alloys [24, 25].

#### **I.3.2. Irregular Co–deposition**

The thermodynamic potentials are near in this situation, and the deposited metals create solid solutions or intermetallic complexes.

#### **I.3.3. Co–deposition at equilibrium**

This co–deposition type is only possible with very low electrolysis currents near the equilibrium levels in the redox systems.

#### **I.3.4. Abnormal Co–deposition (anomalous)**

This type is distinguished by a deposition under diffusion control of the cathodic reduction reaction of the nobler metal. The deposit composition is dictated by the concentration of ions in the diffusion layer. This phenomenon is commonly observed where the thermodynamic potentials of the alloying elements are very close together and the metals form intermetallic compounds or solid solutions. In such case, kinetic and, above all, thermodynamic factors play a role in determining alloy composition.

#### **I.3.5. Induced Co–deposition**

This type occurs with specific metals that, under normal circumstances, cannot be deposited alone in an aqueous solution. This phenomenon is defined by the electrodeposition of these metals as constituents of an alloy, typically alloyed with an element from the iron group.

## I.4. Corrosion

### I.4.1. Corrosion definition

Corrosion is a spontaneous process that occurs through the reaction of materials with their surrounding environment. It can result from a variety of factors, including exposure to moisture, oxygen, acids, salts, or other reactive substances. Corrosion can significantly affect a material's performance and durability, especially those used in critical applications such as infrastructure, transportation, or industrial equipment [26, 27].

### I.4.2 Corrosion mechanisms

A general reaction that describes the corrosion of a metal, M, can be expressed as:



These mechanisms are the outcome of a series of reactions involving electrons and chemical species that take place at the interface between the metal and the solution.

#### I.4.2.1. Anodic reaction

The anodic reaction of metal dissolution, also known as metal oxidation, involves the loss of metal ions from the surface of the metal to the surrounding environment. The general equation for this reaction is:



Where: M represents the metal that is being corroded,  $M^{n+}$  represents the metal ion that is formed, and  $e^{-}$  represents the electrons that are released during the reaction.

This reaction involves the oxidation of the metal, which is the loss of electrons, and the reduction of the environment, which is the gain of electrons. The rate of the anodic reaction depends on several factors, including the nature of the metal, the nature of the environment, and the conditions of exposure. The rate of the reaction can be accelerated by factors such as increased temperature, increased acidity, increased salt content, or the presence of other reactive compounds. The anodic reaction of metal dissolution is an essential part of corrosion, as it is the primary cause of the loss of metal and the degradation of materials. Understanding the factors that influence the rate of this reaction is important for developing effective corrosion prevention strategies.

### *I.4.2.2. Cathodic reaction*

The cathodic reaction of reduction involves the reduction of a species in the solution that comes into contact with the metal surface. The general equation for this reaction is:



Where: M represents the reduced species,  $ne^{-}$  represents the electrons that are gained during the reaction, and  $M^{n+}$  represents the oxidized species. Practically, there is a limited number of cathodic reactions in corrosion. In instances of corrosion within an acidic environment, this reaction involves the reduction of the hydrogen ions that produces atomic or molecular hydrogen. And in alkaline or neutral environments settings like water, the most vital cathodic reaction is the reduction of oxygen. This is expressed through the following reactions:

*In acid environment*



*In neutral or alkaline environment*



The cathodic reaction is important in the context of corrosion because it occurs simultaneously with anodic reaction of metal dissolution, and the two reactions must balance each other for corrosion to occur. In cathodic protection, a more reactive metal or an electric current is used to provide electrons to the metal surface, which drives the cathodic reaction and prevents the anodic reaction of metal dissolution.

The rate of the cathodic reaction depends on the concentration of the species in the electrolyte, as well as the potential difference between the metal and the electrolyte. In some cases, the cathodic reaction can be the limiting factor in the rate of corrosion [24]. Understanding the cathodic reaction is important for developing effective corrosion prevention strategies, such as cathodic protection or the use of corrosion inhibitors that affect the rate of the cathodic reaction.



---

### **I.4.3. Different types of corrosion**

#### ***I.4.3.1. Chemical (or dry) corrosion***

Chemical corrosion (dry corrosion) is a type of corrosion that occurs in the absence of a liquid medium, such as water or acid [28]. It is a type of high-temperature oxidation that can occur when metals are exposed to air at high temperatures, typically above 400 °C. Chemical corrosion can occur through several different mechanisms, including oxidation, sulfidation, and carburization. In oxidation, the metal reacts with oxygen in the air to form metal oxides, which can then further react to form other compounds such as sulfates or phosphates.

Chemical corrosion can be a significant problem in high-temperature applications, such as in boilers, furnaces, and exhaust systems. It can cause material degradation, loss of strength and ductility, and even catastrophic failure. Chemical corrosion can be controlled using protective coatings, such as ceramics or refractory materials, or high corrosion resistant materials. In addition to high-temperature applications, chemical corrosion can also occur in certain atmospheric environments, such as those containing high levels of sulfur or chlorine compounds. It can also occur in certain industrial processes, such as those involving combustion or chemical reactions, where high temperatures and reactive gases are present [26].

#### ***I.4.3.2. Bacterial corrosion***

Bacterial corrosion can be caused by the activities of microorganisms such as bacteria, fungi, and algae. These microorganisms can produce organic and inorganic acids, which can attack the metal surface and accelerate corrosion. Bacterial corrosion can occur in a variety of environments, including water systems, oil and gas pipelines, and marine structures [27].

#### ***I.4.2.3. Electrochemical corrosion***

Electrochemical corrosion, also known as wet corrosion, is a type of corrosion that occurs in the presence of an electrolyte, such as water, acid, or salt solutions. It involves electrochemical reactions at the metal's surface that lead to the metal's dissolution and the formation of corrosion products. Electrochemical corrosion occurs due to the transfer of electrons between the electrolyte and the metal. At the metal surface, anodic reactions occur, where metal atoms are oxidized and release electrons into the electrolyte. This process causes the creation of metal ions and electrons. The metal ions then dissolve into the electrolyte, leading to the corrosion of

the metal. At the same time, cathodic reactions occur in the electrolyte, where a reaction of reduction takes place, which consumes the electrons released from the metal surface. This reaction can be the reduction of oxygen, hydrogen ions, or other species in the electrolyte [28]. The rate of electrochemical corrosion depends on many factors, including the composition of the metal, the properties of the electrolyte, and the environmental conditions. Corrosion can be accelerated by several factors such as high temperature, high humidity, and the presence of contaminants in the electrolyte [29]. Electrochemical corrosion is a common form of corrosion that can cause significant damage to structures and materials. It is commonly observed in pipelines, marine structures, and aircraft. Effective corrosion prevention methods for electrochemical corrosion include the use of protective coatings, cathodic protection, and corrosion inhibitors. This type of corrosion involves an electrically conductive corrosive medium (aqueous media, molten salts). The corrosion of a material corresponds to an oxidation–reduction reaction, where cathodic and anodic reactions are inseparable [29].

#### **I.4.4. Corrosion form's**

##### ***I.4.4.1. Uniform corrosion***

This is the most typical kind of corrosion, occurring when the entire surface of a metal corrodes uniformly at a similar rate (rusting of iron or tarnishing of silver). It is typically induced by interaction with corrosive surroundings, such as saltwater or acidic gases.

##### ***I.4.4.2. Galvanic corrosion***

This type arises from the interaction of two different metals with an electrolyte, such as saline water. This results in an electron transfer between the two metals, causing corrosion of the less noble metal.

##### ***I.4.4.3. Crevice corrosion***

Crevice corrosion occurs in small gaps or crevices in a metal, such as between two overlapping surfaces. This type of corrosion is caused by a lack of oxygen or a buildup of corrosive chemicals in the crevice.

##### ***I.4.4.4. Pitting corrosion***

Pitting corrosion occurs when small pits or craters form on the surface of a metal. This type of corrosion is often caused by exposure to highly acidic or alkaline environments. Deeper pits

---

develop when significant corrosion is restricted to a small area of metal that acts as the anode. while shallower pits result from a broader assault with less depth. Pitting depth is measured by the pitting factor, which represents the ratio of the maximum metal penetration to the average penetration as determined by weight loss.

#### ***1.4.4.5. Stress corrosion cracking***

This corrosion form is developed when a metal is under stress and exposed to harsh surroundings. The stress weakens the metal, making it more susceptible to corrosion.

#### ***1.4.4.6. Intergranular corrosion***

Intergranular corrosion results from the selective erosion of grain boundaries due to environmental factors. This occurs because these boundaries often exhibit distinct chemical compositions and microstructures compared to the interior of grains, rendering them more susceptible to corrosion. The reasons and mechanisms of intergranular corrosion depend on the metal type and the surrounding conditions.

### **1.4.5. Protective methods**

There are several methods used to protect materials against corrosion. depending on the type of material, the environment, and the intended application. Here are some common corrosion protection methods:

#### ***1.4.5.1. Barrier protection***

This involves the use of a physical barrier between the material and the corrosive environment, such as coatings, paint, or plating. These barriers prevent the material from encountering the corrosive environment.

#### ***1.4.5.2. Cathodic protection***

This technique involves connecting the material to a sacrificial anode composed of a more reactive metal. This anode corrodes instead of the protected material, effectively providing a cathodic protection against corrosion [30].

#### ***1.4.5.3. Anodic protection***

---

This is the opposite of cathodic protection, where the protected material is made the anode in an electrochemical cell, and the cathode is made of an inert material. This prevents the material from corroding by creating a protective oxide layer.

#### ***1.4.5.4. Inhibitors***

Corrosion inhibitors are chemical or compound additives that are introduced into an environment to prevent or reduce the rate of corrosion. These inhibitors can be organic or inorganic compounds that adsorb onto the metal surface and form a protective film.

#### ***1.4.5.5. Alloying***

Some metals can be combined with other metals or nonmetals to improve their corrosion resistance. For example, adding chromium to steel produces stainless steel, which is highly resistant to corrosion.

#### ***1.4.5.6. Design modification***

Changing the design of a structure or equipment can help to reduce the risk of corrosion. For example, the use of non-corrosive materials or the use of a more corrosion-resistant material in a critical area can help to prevent corrosion.

#### ***1.4.5.7. Environmental modification***

Changing the environment around the material can help to prevent corrosion. This may include controlling the temperature, humidity, pH, or other chemical parameters to reduce the corrosive nature of the environment.

### **1.4.6. Factors of corrosion**

Corrosion is a complex process influenced by several factors that can accelerate or inhibit it. Understanding the factors that can affect corrosion is essential to developing effective corrosion prevention and mitigation strategies. Many important elements that can influence corrosion are listed below [31, 35] :

- ❖ **Environment:** The environment in which a material is placed plays a vital role in corrosion. Factors such as acidity, temperature, humidity, and exposure to chemicals and pollutants can accelerate or inhibit corrosion.
- ❖ **Material composition:** The composition of the material being corroded can also affect its susceptibility to corrosion. For example, the existence of alloying elements can improve the material's resistance to corrosion, while impurities can make it more susceptible to corrosion.
- ❖ **Surface condition:** The condition of the material's surface can also affect corrosion. A rough surface can provide more sites for corrosion to occur, while a smooth surface can inhibit corrosion.
- ❖ **Electrochemical factors:** Corrosion is an electrochemical process, so factors such as the presence of an electrolyte, the potential difference between two metals, and the rate of electron transfer can all influence the rate of corrosion.
- ❖ **Mechanical stress:** Mechanical stress can also affect corrosion. Stress can cause cracks, which can provide sites for corrosion to occur, and can also cause material fatigue, which can lead to corrosion.

### **I.5. Electrodeposition of Ni–Mn and Zn–Ni–Mn alloys**

Nickel (Ni), Zinc (Zn), and Manganese (Mn) are distinctive transition metals with high conductivity making them crucial in corrosion processes, both as catalysts and as materials that can undergo corrosion themselves [35, 37]. In fact, (Zn) is widely recognized as a common element employed in surface treatments due to its attractive physicochemical and mechanical properties, both as a basic ingredient and as an additive in the creation of different coatings [38, 39]. In addition, (Ni) coatings have found extensive applications in the chemical, mechanical, and electronic industries due to their excellent wear and abrasion resistance, as well as their corrosion resistance [8, 40]. The incorporation of Ni, and Mn during Zn deposition process can further augment distinct characteristics, thereby enhancing overall performance [41– 44].

The choice of Mn as an additional metal is justified by its electronegativity, which results in a significantly cathodic redox potential [45]. Furthermore, Mn has the capacity to form multiple oxides, contributing to the development of alloy coatings that are more resistant [46, 47]. Nevertheless, this electrochemical characteristic adds complexity to the co–deposition process,

necessitating precise conditions to achieve alloys that fulfill the desired properties. Specifically, its deposition potential that directly initiates the undesired hydrogen reduction reaction [48, 49].

### I.5.1. Nickel (Ni)

Ni is renowned for its conductivity, resistance to corrosion by forming a compact, adherent, and protective NiO oxide layer, excellent ability to alloy with other metals, and displays ferromagnetism. In the field of electroplating, Ni is employed to impart protective, decorative, or wear-resistant coatings onto diverse materials [50]. It has a face-centered cubic (FCC) structure form with a lattice parameter of  $a = 0.352$  nm which remains stable until it reaches its melting temperature of  $T_f = 1450$  °C. It can also assume a hexagonal close-packed (HCP) structure with lattice parameters  $a = 0.2622$  nm and  $c = 0.4321$  nm. This HCP phase does not naturally occur and forms within a temperature range of 220 to 440 °C, depending on the rate of heating [51]. Ni belongs to Group VIII of transition metals, and its remarkable malleability and ductility allow it to be easily shaped and stretched without breaking. Moreover, it boasts a high melting point, and its exceptional hardness emphasizes its strength and durability [51].

Ni has various oxidation states, with its most common and stable state being +2, represented as  $\text{Ni}^{2+}$ . However, it can also occur in less common oxidation states, including +1, +3, and +4, typically in specific chemical reactions or compounds. In electrochemistry, the standard reduction potential for the conversion of nickel ions ( $\text{Ni}^{2+}$ ) into elemental nickel ( $\text{Ni}^0$ ) in aqueous solutions is approximately  $-0.25$  volts (V) under standard conditions. This negative standard reduction potential indicates that Ni has a natural inclination to undergo reduction, meaning it readily gains electrons to form solid Ni metal when exposed to suitable reducing agents. This standardized reduction potential is a crucial parameter in the field of electrochemistry, providing valuable insights into nickel's reactivity across a range of chemical and electrochemical processes. It is used to assess the feasibility and direction of reactions involving Ni, aiding in the understanding of its behavior in various environments. A Pourbaix diagram (E–pH) for Ni (figure I. 8), provides a visual representation of different Ni species in aqueous environments. at different pH levels and electrode potentials. The diagrams commonly feature several important regions and species:

The diagram shows stable metallic nickel ( $\text{Ni}^0$ ) in high pH and oxidizing conditions, with successful electrodeposition below pH=6. Above pH=4.2, Ni can be deposited without releasing hydrogen, though practical applications tend to cause some hydrogen evolution due

to cathodic overpotential. In moderately alkaline conditions and under relatively low electrode potentials (reducing conditions), Ni can react with water to produce Ni hydroxides like Ni(OH)<sub>2</sub> and Ni(OH)<sub>3</sub>, serving as corrosion byproducts in specific scenarios. In oxidizing conditions, particularly at higher electrode potentials and within the moderately alkaline to neutral pH range, Ni can form various oxide phases, including NiO, Ni<sub>2</sub>O<sub>3</sub>, and Ni<sub>3</sub>O<sub>4</sub>, and these Ni oxides remain stable in such conditions [49, 52].

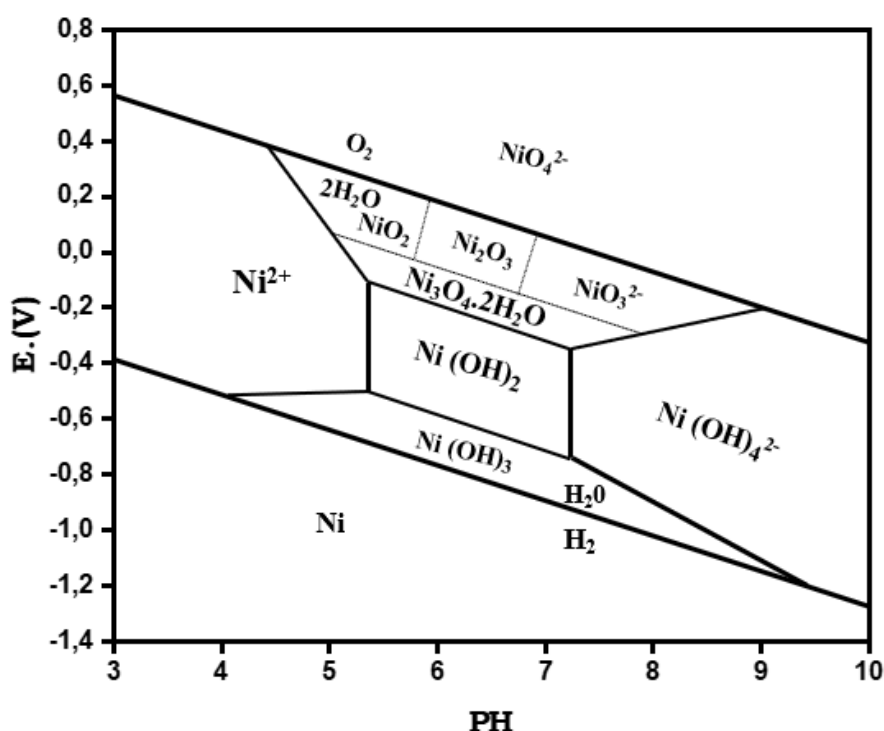


Figure I. 13. Nickel–H<sub>2</sub>O system's Pourbaix diagram at 25 °C [42].

### I.5.2. Zinc (Zn)

Zinc (Zn) has a hexagonal close-packed (HCP) structure with a lattice parameter of approximately 0.26652 nanometers [44]. Zn exhibits typical transition metal properties, including good electrical conductivity, the ability to assume multiple oxidation states, and the formation of complex ions. The E–pH diagram depicting Zn's behavior reveals that metallic Zn is most stable within its "immunity domain." When exposed to an acidic solution, it oxidizes into Zn<sup>2+</sup>. In strongly alkaline conditions, various dissolved species (HZnO<sup>2-</sup> and ZnO<sub>2</sub><sup>2-</sup>) come into existence. The corrosion of Zn can result in the formation of Zn(OH)<sub>2</sub> hydroxide, creating what is known as the "passivation zone." Irrespective of the solution's pH, when the potential reaches a sufficiently anodic level, ZnO<sub>2</sub> oxide is produced. These hydroxide and oxide compounds collectively act as inhibitors, decelerating the Zn corrosion process, and this phase

is termed the "passivation domain." In an aqueous environment, hydroxide ( $\text{Zn}(\text{OH})_2$ ) remains stable within the pH range of 7 to 13. To precipitate zinc oxide ( $\text{ZnO}(\text{s})$ ) or its hydroxide form ( $\text{Zn}(\text{OH})_2$ ), a significantly higher pH level is necessary [53, 54].

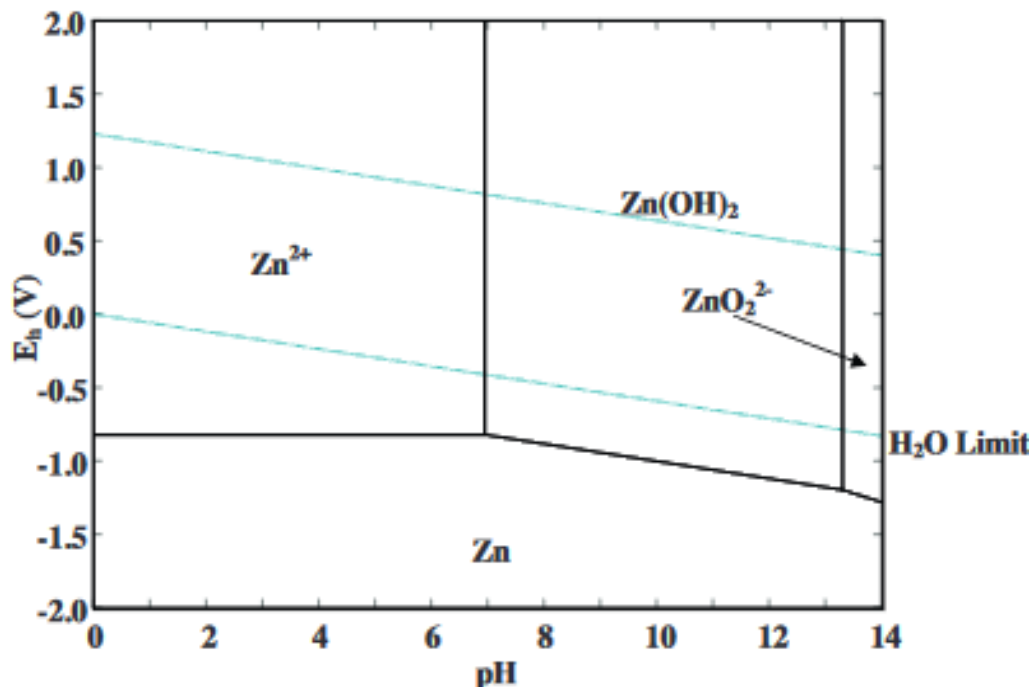


Figure I.9. Zn–H<sub>2</sub>O system's Pourbaix diagram at 25 °C [46]

### I.5.3. Manganese (Mn)

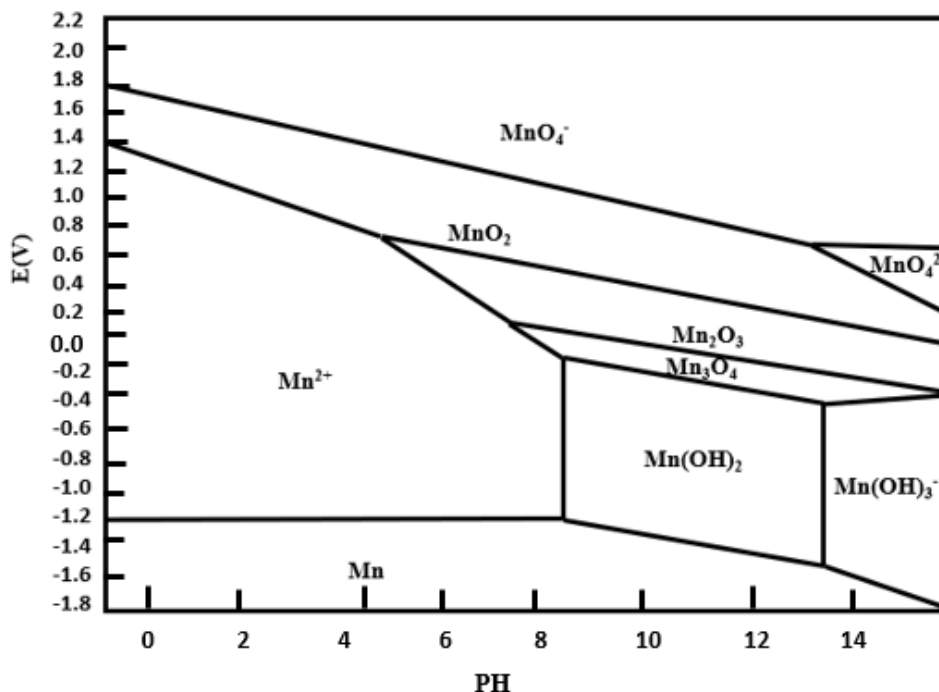
In its solid state at standard conditions, Mn adopts a body-centered cubic (BCC) crystal structure with a lattice parameter of  $a = 0.288$  nm. Though it can assume different structures under varying temperature and pressure conditions, such as HCP or FCC, depending on environmental factors and phase transitions. Mn exhibits a relatively high density, measuring in at approximately  $7.21$  g/cm<sup>3</sup>. This density enhances its overall sturdiness and resilience, making it a comparatively dense element. Mn can adopt less common oxidation states, spanning a wide range from  $-3$  to  $+7$ , typically observed in specific chemical reactions or compounds. Moreover, Mn stands as the least noble and most electronegative among all metals. The standard reduction potential ( $E^\circ$ ) of Mn fluctuates depending on the specific redox reaction and environmental conditions. For instance:

In the reduction of  $\text{MnO}_4^-$  to  $\text{Mn}^{2+}$  in the presence of  $8\text{H}^+$  and  $5\text{e}^-$ :  $E^\circ = +1.51$  volts

In the reduction of  $\text{MnO}_2$  to  $\text{Mn}^{2+}$  with  $4\text{H}^+$  and  $2\text{e}^-$ :  $E^\circ = +1.23$  volts.



The E–pH diagram for Mn is notably more intricate due to the extensive range of possible oxidation states, as illustrated in figure I.10. In the case of corrosion within a neutral or slightly alkaline environment, Mn can exhibit two outcomes: it may either dissolve into solution as  $\text{Mn}^{2+}$  ions or contribute to the formation of  $\text{Mn}(\text{OH})_2$  hydroxides [53, 55].



**Figure.I.14.** Mn–H<sub>2</sub>O system's Pourbaix diagram at 25 °C [56].

#### I.5.4. Ni–Mn Thin films

In light of the captivating properties of Ni–Mn thin films, several works have extensively examined the influence of various electroplating parameters, such as bath composition, pH, deposition potential, temperature...etc [48, 49]. It has been found that different plating solutions might easily deposit Ni–Mn films [52, 57]. For example, Dini and Johnson achieved significant results by plating Ni–Mn coatings with a Mn content of 1420 ppm, using sulfate salt, which demonstrated notably superior mechanical strength and flexibility compared to pure Ni coatings that underwent sulfamate electroplating [43, 48]. Meanwhile, Goods and Yang have utilized a sulfamate electrolyte for plating Ni–Mn deposits. It's worth noting that the Mn content in the deposits was relatively low, generally equal to or less than about 1 wt.%. They also noted that simultaneous deposition of Mn with Ni is insensitive to feature aspect ratio, demonstrating process stability [53]. Wei–Yu and Sen–lin Wang conducted a study on the plating solution, introducing sodium citrate as a complexing agent to form a complex that effectively stabilized the reduced potential of Mn(II) and Ni(II) ions, facilitating their co–deposition [48].

The corrosion properties of electrodeposited Ni–Mn coatings on mild steel have been investigated, examining various influencing factors such as current density, different Ni–Mn compositions in the bath, and the presence of different additives like glycerol, n-butanol, benzene, pyridine, thioglycolic acid, Gelatin and ammonium sulfate. They found that the corrosion properties of electrodeposited Ni–Mn coatings depend significantly on plating variables. A higher Mn content in the deposit resulted in an increased sacrificial nature of the coatings [58].

Similarly, Jiacheng Guo et al delved into the corrosion properties of Ni–Mn alloys, controlling the effects of different Mn content, current density and glycine on the composition, and the microstructure of the films. They reveal that the presence of glycine altered the Ni–Mn coatings growth mode. As the current density and glycine concentration decrease, the Mn content in the Ni–Mn film increases. Additionally, a Ni–Mn alloy film containing 3.1 at. % Mn displayed the best corrosion resistance among the films, surpassing that of pure Ni coating [59].

Yang. N and all studied the influence of Mn concentration on the microhardness, microstructure, and texture of Ni–Mn films. A comparison between the properties of Ni–0.5wt.% Mn deposits and those of pure Ni deposits obtained from a sulfate solution has been performed. It can be stated that the inclusion of Mn in the alloy refines the grains and enhances twin density. This is explained by the Mn solute lowering the stacking fault energy, a behavior observed in other Ni–based alloys [52].

Furthermore, Kuan–Hui Cheng and all, examined the influence of current density and  $Mn^{2+}$  concentration within the electrolyte on the electrodeposition of Ni–Mn alloys onto a copper substrate from a sulfate bath. The results indicated that raising the  $Mn^{2+}$  concentration by itself did not improve the Mn content but, rather, reduced cathodic efficiency. Conversely, higher current density promoted Mn co–deposition, resulting in finer crystallites, increased coating hardness, and internal stress. Utilizing a current density of 1 A/dm<sup>2</sup> for probe fabrication met the criteria of high hardness, low internal stress, sufficient fatigue life, and non–sticking properties for microelectronics applications [49].

Also, Marquis, E. A and all investigate the effect of current density and the addition of  $MnCl_2$  in the electrolyte on the microstructure and texture of Ni electrodeposits. The results show that the introduction of  $MnCl_2$  into the bath alters the film's texture by promoting the (110) direction and results in fine–grained materials at all current density levels. While the overall Mn

concentration correlates with current density, the local Mn concentration exhibits significant variation, ranging from 0 to 6 at. % Mn, for both DC plated and pulse-plated Ni–Mn deposits [60]

Fathi and S. Sanjabi carried out electroplating of a Ni–Mn alloy coatings onto copper substrate within a chloride-based bath at different current densities with varying Mn concentrations in the bath. They established that the Mn concentration increased as the current raised. However, the Ni/Mn ratio didn't substantially affect the alloy's composition [37].

### **1.5.5. Zn–Ni–Mn Thin films**

Over several decades, Zn has functioned as a sacrificial anode to combat corrosion. The industry's pursuit of heightened corrosion resistance has resulted in the creation of longer-lasting Zn-based coatings such as Zn–Co [61], Zn–Ni [62], Zn–Fe [54] and Zn–Mn [21]. Zn–Mn alloys are preferred for their cost-effectiveness, ease of casting, and resistance to corrosion [63– 65]. However, Zn–Ni alloys are known for their excellent combination of properties, including corrosion resistance, high strength, and the ability to maintain their performance at elevated temperatures [66, 67]. Combining these alloys can result in advanced materials like Zn–Ni–Mn alloys, exhibiting diverse properties for various applications [68, 69]. R. Kashyap prepared nano-crystalline Zn–Ni–Mn films from a sulfate bath. Their findings revealed that the proportions of Ni and Mn in the deposits increased for higher current density, temperature, and electrolysis duration. Conversely, an increase in the solution's pH led to higher Zn content. They also recorded the influence of reducing temperature, altering solution pH, and adjusting current density on the mechanical properties of the alloys [63]. In another study, they recorded the deposition of Ni and Mn at (–0.75 V vs Ag/AgCl) and (–1.18 V vs Ag/AgCl), respectively, from aqueous electrolytes. Additionally, they noted that the concentrations of Ni and Mn in the alloy escalated with an increase in electrodeposition current density, temperature, and electroplating duration [70].

Electrodeposited Zn–Ni–Mn coatings have been prepared from the citrate bath, exploring their viability as a potential alternative to electroplated cadmium thin films [71]. The results reveal the successful deposition of compositionally modulated Zn–Ni and Zn–Ni–Mn coatings from single baths, with different Ni (5–20 %) and Mn (0–12% Mn) contents. Notably, measurements of current efficiency indicated lower efficiency, particularly for the Zn–Ni–Mn coatings. Reporting that both coatings had reduced corrosion resistance compared to cadmium,

particularly in accelerated tests. This decrease in corrosion resistance was mainly due to higher Ni content, resulting in a less dense electroplated layer. Consequently, the increased thickness porosity, promoted the nobility of Zn–Ni and Zn–Ni–Mn coatings, making them non-sacrificial to the substrate in accelerated tests. Zn–Ni–Mn coatings exhibited superior resistance to white rust formation compared to Zn–Ni and displayed higher micro-hardness than Zn and Cd coatings [71].

F. H. Assaf studied the effect of current density on the electrochemical behavior of Zn–Ni–Mn coatings deposited on steel substrate. They observed that  $Zn^{2+}$  ions concentration in the bath inhibited Ni and Mn deposition. It is also reported that an increase in plating current density led to higher Ni and Mn contents in the deposits, with higher Ni content correlating with improved corrosion resistance and cathodic current efficiency [64].

In another study led by F. H. Assaf et al, the electrodeposition of Zn–Mn–Ni alloys in an aqueous sulfate solution has been investigated. They established that the Zn–Ni–Mn alloy's electrodeposition mechanism followed an anomalous type, exhibiting exceptional corrosion resistance and a preferred surface appearance compared to electrodeposited Zn–Ni alloy under same conditions. Significantly, they observed that, under specific conditions, Mn could be co-deposited with Ni or with Ni and Zn, preventing its deposition in its pure form. When Mn was electrodeposited alone or in Mn alloys, a dark brown deposit is formed on the platinum electrode surface due to its oxidation into Mn dioxide [65].

Fashu and R. Khan introduced the electrodeposition of ternary Zn–Mn–Ni alloys using a choline chloride-based ionic liquid. They examined the effect of deposition potential on the composition and corrosion resistance of the resulting Zn–Mn–Ni deposits, comparing them to Zn–Mn deposits. Noting distinct behaviors compared to Zn–Mn and Zn–Ni alloys. Mn deposition occurred at more positive potentials in the Zn–Mn–Ni electrolyte. They additionally documented the expansion of the Zn lattice with Mn and Ni embedment at low potentials, shifting to the  $MnZn_{13}$  phase with embedded Ni at higher potentials. Corrosion tests affirmed that incorporating Ni improved corrosion resistance in the Zn–Mn–Ni alloys compared to the Zn–Mn binary alloys, while maintaining passivation behavior [72].

The effect of deposition potential on Zn–Ni–Mn alloy coatings has been investigated [73]. It is found that within the  $-0.5$  to  $-1$  V deposition potential range, normal co-deposition occurred, while more cathodic potentials below  $-1$  V led to anomalous co-deposition. Additionally,

negative shifts in potentials leads to the refinement of the crystal size, indicating hexagonal Zn, and cubic/tetragonal Ni–Zn phases in the deposit. This shift enhances corrosion resistance, microhardness, and wear resistance properties [73].

B. Abedini investigated the electrodeposition of Zn–Ni–Mn/Zn–Ni multi-layers of coatings by varying the potential range in an alkaline solution. It has been found that the samples prepared through pulse electrodeposition exhibited a smoother surface as compared to that of the coatings deposited at a constant potential. Electrochemical analyses revealed that coatings deposited at a constant potential had higher polarization resistance, and their surface's passive layer was more compact compared to pulse–electrodeposited coatings [74].

In another study, the effects of electrolyte  $\text{Mn}^{2+}$  concentration and deposition potential on the surface characteristics, phase structure, and corrosion resistance of the coatings have been examined. It was disclosed that a higher Mn content in Zn–Ni–Mn coatings promoted a good corrosion resistance. Moreover, Zn–Ni–Mn coatings exhibited a passive layer composed of Zn hydroxide chloride, Zn oxide, Zn hydroxide carbonate, and Mn oxides [67].

The morphology and composition of Zn–Ni–Mn alloys, deposited from gluconate baths have been investigated. The influence of the deposition potential rather than the bath composition has been established. Multiphase ternary alloys are formed only at deposition potential values more negative than  $-1.5 \text{ V}$  (Ag/AgCl). An anomalous co–deposition of metals in accordance with the instantaneous nucleation model was found. Additionally, at more negative potentials and in the presence of chloride ions, a transition from progressive to instantaneous nucleation stages was observed. A comparison of surface wettability revealed enhanced hydrophobicity due to the spontaneous oxidation of Zn–rich alloys. Sulfate anions distinctly affected cathodic processes, leading to higher deposit masses, lower Mn percentages, and the creation of coarser, more compact, hydrophobic deposits with high corrosion resistance in neutral solutions [68].

## **I.6. Conclusion:**

This chapter provides a theoretical overview of thin films, the electrodeposition of metals and alloys, as well as the mechanisms of nucleation and electrochemical growth. The subsequent section delves into the theoretical aspects of corrosion, its various forms, and protective methods. Finally, the chapter presented a detailed literature review on the electrodeposition of Ni–Mn and Zn–Ni–Mn alloys, emphasizing the importance and relevance of these alloy systems.

---

**References**

- [1] P. Panjan, A. Drnovšek, P. Gselman, M. Čekada, and M. Panjan, “Review of growth defects in thin films prepared by PVD techniques,” (2020), *Coatings*, v. 10, N°. 5.
- [2] R. Della Noce *et al.*, “Structural, morphological and magnetic characterization of electrodeposited Co – Fe – W alloys,” (2014), *J. Alloys Compd.*, v. 611, pp. 243–248,
- [3] A. Nouri, L. Hadjeris, M. S. Aida, N. Attaf, M. L. Benkhedir, and A. Djelloul, “Élaboration et caractérisation de couches minces d’oxydes métalliques destinées à des applications optoélectroniques,” (2016), Doctorat thesis, *Université Larbi Ben M'hidi – Oum El Bouaghi*.
- [4] N. Ahmed, B. A. Ali, M. Ramadan, and N. K. Allam, “Nanosheets for High Performance Asymmetric Supercapacitor,” (2019), *ACS Appl. Energy Mater.*, v. 2, pp. 3717–3725.
- [5] Y. Han *et al.*, “Redox-active nanostructure electrode of Mn/Ni bimetal organic frameworks anchoring on multi-walled carbon nanotubes for advanced supercapacitor,” (2021), *J. Electroanal. Chem.*, v. 882, p. 114993.
- [6] J. Jiao, M. Zhang, and S. Pan, “Aluminoborates as Nonlinear Optical Materials,” (2023), *Angew. Chemie*, v. 202217037.
- [7] D. Commandeur, C. Sabado, T. E. Ashton, and J. A. Darr, “Combinatorial Performance Mapping of Near-NMC111 Li-ion Cathodes,” (2021), *Journal of Materiomics*,
- [8] X. Long, J. Li, Z. Shen, and Y. Su, “Dimensionless Analysis to Determine Elastoplastic Properties of Thin Films by Indentation,” (2022), *Coatings*, v. 12, N°. 11,
- [9] M. Bu, J. Rogan, S. I. Stevanovi, S. Stankovi, and J. B. Bajat, “The influence of anion type in electrolyte on the properties of electrodeposited Zn Mn alloy coatings,” 2013, *Surface & Coatings Technology*, v. 228, pp. 221–228.
- [10] R. S. Bhat, K. B. M. R. Prasanna, S. K. Venkatakrisna, and A. C. Hegde, “Electrochemical studies on the corrosion resistance of Zn – Ni – Co coating from acid chloride bath,” (2020), *Appl. Phys. A*, v. 126, N°. 10, pp. 1–9.
- [11] Pelloux Albert. Luigi Brugnatelli (1859–1928), *Bulletin de la Société française de Minéralogie*, v, 52, 1–3, 1929. pp. 69–71.
- [12] L. N. Mendome, “Surfaces nanostructurées de nickel électrodéposé sur divers substrats de dépôt : étude de la croissance d’interface et des caractéristiques magnetiques,” (2007), p. 155, Doctorate thesis, *université de Reims Champagne-Ardenne*
- [13] K. Eiler, S. Suriñach, J. Sort, and E. Pellicer, “Applied Catalysis B: Environmental Mesoporous Ni-rich Ni-Pt thin films: Electrodeposition, characterization and

- performance toward hydrogen evolution reaction in acidic media,” (2020), *Appl. Catal. B Environ.*, v. 265, 2019, p. 118597,
- [14] M. Schlesinger and M. Paunovic, *Fundamentals of Deposition*. (2006) University of Windsor Windsor, Ontario, Canada. Milan Paunovic, Mordechai Schlesinger. 2nd ed
- [15] B. Moufida, “Tenue à la corrosion en milieu acide d’un dépôt de Zn Sn sur acier inoxydable,” (2014), Memoire magister, *Université Ferhat ABBAS – Sétif I*
- [16] F. ZAKIA, “Electrodéposition des métaux (Fe, Ni, Mo, Co...) sur silicium et silicium poreux,” (2013), Doctorat thesis, *université abou bakr belkaïd – tlemcen.*
- [17] M. Loubna, “Effets des Additifs Organiques sur les Propriétés de Films Minces Granulaires de Co–Cu,” (2013), Doctorat thesis, *Université Ferhat ABBAS – Sétif I*.
- [18] J. O. M Bockris, B. E Conway, R. E White “Modern aspects of electrochemistry,” (2002), *Nucl. Phys.*, v, 13, no. 1, pp. 104–116, 1959.
- [19] B, SCHARIFKER, and G, Hills “Theoretical and experimental studies of multiple nucleation,” (1982), *.Electrochim. Acta*, v. 28, N°. 2, pp. 879–889,
- [20] S. Basavanna and Y. Arthoba Naik, “Study of the effect of new brightener on Zn–Ni alloy electrodeposition from acid sulphate bath,” (2011), *J. Appl. Electrochem.*, v. 41, N°. 5, pp. 535–541,
- [21] N. Loukil and M. Feki, “Electrodeposition: A Literature Review,” (2020), *Electrochem. Soc.* 167 022503
- [22] R. Sudha and K. Rathinam, “Characterization of electrodeposited nanocrystalline Ni–Mn thin films for MEMS applications,” (2014), *J. Optoelectron. Adv. Mater.*v. 16, N°. 5–6.
- [23] M. Stratmann, “Atmospheric corrosion of iron. A discussion of the physico–chemical fundamentals of this omnipresent corrosion process invited review,” (1990), *Berichte der Bunsengesellschaft/Physical Chem. Chem. Phys.*, v. 94, N°. 6, pp. 626–639,
- [24] M. E. D. Turner, “Corrosion Engineering and Corrosion Science.,” (1980), *Materials Performance*, v. 19, N°. 10. pp. 51–52.
- [25] Luciano Lazzari and MariaPia Pedefferri, “*Statistical Analysis of Corrosion Data*,” (2018). *Springer Nature Switzerland AG*, ISSN 1868–1212 (electronic).
- [26] D. Sylla, J. Creus, C. Savall, O. Roggy, M. Gadouleau, and P. Refait, *Corrosion and corrosion control. An introduction to corrosion science and engineering. Third Edition*. (1985).
- [27] J. Luo, “Corrosion of copper in antibacterial efficiency test,” (2020), Doctorat thesis, *Université de Lorraine*.

- [28] Z. Khiati, "Inhibition de la corrosion du cuivre en milieu chlorure et sulfate neutre par une nouvelle molécule dérivée de 1,2,4-triazole," (2013), Doctorate thesis. L'université des Sci. la Technol. d'Oran.
- [29] P. Tamurejo–Alonso, M. L. González–Martín, and M. Á. Pacha–Olivenza, "Electrodeposited Zinc Coatings for Biomedical Application: Morphology, Corrosion and Biological Behaviour," (2023), *Materials (Basel)*, v. 16, N°. 17, pp. 1–42.
- [30] F. Martinelli–Orlando, S. Mundra, and U. M. Angst, "Cathodic protection mechanism of iron and steel in porous media," (2024), *Commun. Mater.*, v. 5, N°. 1, pp. 1–11,
- [31] J. E. Oh and Y. H. Kim, "The corrosion resistance characteristics of Ni, Mn, and Zn phosphates in automotive body panel coatings," (2012), *J. Ind. Eng. Chem.*, vol. 18, N°. 3, pp. 1082–1087.
- [32] J. Gong, G. Wei, J. A. Barnard, and G. Zangari, "Electrodeposition and characterization of sacrificial copper–manganese alloy coatings: Part II. Structural, mechanical, and corrosion–resistance properties," (2005), *Metall. Mater. Trans. A Phys. Metall. Mater. Sci.*, v. 36, N°. 10, pp. 2705–2715.
- [33] Z. I. Ortiz, P. Díaz–Arista, Y. Meas, R. Ortega–Borges, and G. Trejo, "Characterization of the corrosion products of electrodeposited Zn, Zn–Co and Zn–Mn alloys coatings," (2009), *Corros. Sci.*, v. 51, N°. 11, pp. 2703–2715,
- [34] H. Kazimierczak, A. Hara, A. Bigos, and P. Ozga, "Electrodeposition of Zn–Mn–Mo layers from citrate–based aqueous electrolytes," (2016), *Electrochim. Acta*, v. 202, pp. 110–121,
- [35] Abdel Rahman El–Sayed, H. S. Mohran, and H. M. Abd El–Lateef, "Corrosion study of zinc, nickel, and zinc–nickel alloys in alkaline solutions by Tafel plot and impedance techniques," (2012), *Metall. Mater. Trans. A Phys. Metall. Mater. Sci.*, v. 43, N° 2, pp. 619–632.
- [36] W. Cable, "Magnetic short–range order and magnetic moments of Co–Mn and Ni–Mn alloys J." (2008), American Physical Society, v. 50, N°. 13.
- [37] R. Fathi and S. Sanjabi, "Electrodeposition of nanostructured Ni(1–x)Mnx alloys films from chloride bath," (2012), *Curr. Appl. Phys.*, vol. 12, N°. 1, pp. 89–92,
- [38] R. S. Bhat, K. B. Munjunatha, S. I. Bhat, K. Venkatakrisna, and A. C. Hegde, "Electrochemical Studies of Zn–Ni–Fe Alloy Coatings for Better Corrosion Resistance Applications," (2022), *J. Mater. Eng. Perform.*,
- [39] H. S. Lee *et al.*, "Corrosion mechanism and kinetics of Al–Zn coating deposited by arc thermal spraying process in saline solution at prolong exposure periods," (2019), *Sci.*



- Rep.*, v. 9, N<sup>o</sup>. 1, pp. 1–17,
- [40] W. Reeks, H. Davies, and S. Marchisio, “A review: Interlayer joining of nickel base alloys,” (2020), *J. Adv. Join. Process.*, v. 2, 100030.
- [41] R. Oriňáková, A. Turoňová, D. Kladeková, M. Gálová, and R. M. Smith, “Recent developments in the electrodeposition of nickel and some nickel–based alloys,” (2006), *J. Appl. Electrochem.*, v. 36, N<sup>o</sup>. 9, pp. 957–972.
- [42] L. F. Huang, M. J. Hutchison, R. J. Santucci, J. R. Scully, and J. M. Rondinelli, “Improved Electrochemical Phase Diagrams from Theory and Experiment: The Ni–Water System and Its Complex Compounds,” (2017), *J. Phys. Chem. C*, v. 121, N<sup>o</sup>. 18, pp. 9782–9789.
- [43] T. I. Petrova and E. A. Selivanov, “Using of Pourbaix diagram for evaluation of water chemistry recommended for ultra–supercritical parameter of water coolant,” (2017), *J. Phys. Conf. Ser.*, v. 891, N<sup>o</sup>. 1, pp. 3–10.
- [44] M. Zinke–Allmang, L. C. Feldman, and M. H. Grabow, “Clustering on surfaces,” (1992), *Surf. Sci. Rep.*, v. 16, N<sup>o</sup>. 8, pp. 377–463.
- [45] P. Díaz–Arista and G. Trejo, “Electrodeposition and characterization of manganese coatings obtained from an acidic chloride bath containing ammonium thiocyanate as an additive,” (2006), *Surf. Coatings Technol.*, v. 201, N<sup>o</sup>. 6, pp. 3359–3367.
- [46] A. T. Al–Hinai, M. H. Al–Hinai, and J. Dutta, “Application of Eh–pH diagram for room temperature precipitation of zinc stannate microcubes in an aqueous media,” (2014), *Mater. Res. Bull.*, vol. 49, N<sup>o</sup>. 1, pp. 645–650,
- [47] J. Lu, D. Dreisinger, and T. Glück, “Manganese electrodeposition – A literature review,” (2014), *Hydrometallurgy*, v. 141, pp. 105–116.
- [48] S. L. Wang and W. W. Yu, “Influence of the plating conditions on the structure and corrosion resistance of the Ni–Mn alloy,” (2008), *Key Eng. Mater.*, v. 373–374, pp. 442–445,
- [49] K. H. Cheng *et al.*, “Fabrication of Ni–Mn microprobe structure with low internal stress and high hardness by employing DC electrodeposition,” (2014), *Adv. Mater. Sci. Eng.*
- [50] W. R. Wearmouth, “Nickel Alloy Electrodeposits for Non–Decorative Applications,” (1982), *Trans Inst Met Finish*, v. 60, pp. 68–73.
- [51] H. Boudjehem, H. Moumeni, A. Nemamcha, S. Pronkin, and J. L. Rehspringer, “Effect of deposition conditions on the properties of Ni–Mo–W coatings as electrocatalysts for hydrogen evolution reaction,” (2022), *J. Appl. Electrochem.*, v. 52, N<sup>o</sup>. 2, pp. 217–229.

- [52] N. Y. C. Yang, T. J. Headley, J. J. Kelly, and J. M. Hruby, "Metallurgy of high strength Ni–Mn microsystems fabricated by electrodeposition," (2004), *Scr. Mater.*, v. 51, N°. 8 SPEC. ISS., pp. 761–766.
- [53] S. H. Goods, J. J. Kelly, and N. Y. C. Yang, "Electrodeposited nickel–manganese: An alloy for microsystem applications," (2004), *Microsyst. Technol.*, v. 10, N°. 6–7, pp. 498–505.
- [54] C. Arrighi *et al.*, "Optimization of the morphology, structure and properties of high iron content Zn–Fe coatings by pulse electrodeposition," (2021), *Mater. Chem. Phys.*, v. 263,
- [55] C. Savall, C. Rebere, D. Sylla, M. Gadouleau, P. Refait, and J. Creus, "Morphological and structural characterisation of electrodeposited Zn–Mn alloys from acidic chloride bath," (2006), *Mater. Sci. Eng. A*, v. 430, N°. 1–2, pp. 165–171.
- [56] C. Fahima, "Matériau d'électrode à base du carbone modifié par un film de polymère et contenant du bioxyde de Manganèse," Memory of Magister, Ferhat Abbas University of Setif, p. 77, 2011.
- [57] A. Stephen, M. V Ananth, V. Ravichandran, M. S. Centre, and G. Campus, "Magnetic properties of electrodeposited nickel  $\pm$  manganese alloys: Effect of Ni / Mn bath ratio," (2000). *Journal of Applied Electrochemistry*, 30: pp. 1313–1316,
- [58] M. V. Ananth, "Corrosion studies on electrodeposited nickel–manganese coatings," (1997), *Trans. Inst. Met. Finish.*, v. 75, N°. 6, pp. 224–227.
- [59] J. Guo, X. Guo, S. Wang, Z. Zhang, J. Dong, and L. Peng, "Applied Surface Science Effects of glycine and current density on the mechanism of electrodeposition, composition and properties of Ni – Mn films prepared in ionic liquid," (2016), *Appl. Surf. Sci.*, v. 365, pp. 31–37.
- [60] E. A. Marquis, A. A. Talin, J. J. Kelly, S. H. Goods, and J. R. Michael, "Effects of current density on the structure of Ni and Ni–Mn electrodeposits," (2006), *J. Appl. Electrochem.*, v. 36, N°. 6, pp. 669–676.
- [61] R. S. Bhat, K. B. Manjunatha, K. Venkatakrishna, and A. C. Hegde, "Electrodeposition of Zn – Co Coating and its Electrochemical Performance," (2022), *Protection of Metals and Physical Chemistry of Surface*, v. 58, N°. 1, pp. 99–108.
- [62] C. A. M. Dutra, J. W. J. Silva, and R. Z. Nakazato, "Corrosion Resistance of Zn and Zn–Ni Electrodeposits: Morphological Characterization and Phases Identification," (2013), *Materials Sciences and Applications*, N°. 4, 644–648.
- [63] D. Sylla, J. Creus, C. Savall, O. Roggy, M. Gadouleau, and P. Refait, "Electrodeposition of Zn–Mn alloys on steel from acidic Zn–Mn chloride solutions," (2003), *Thin Solid*

- Films*, v. 424, N°. 2, pp. 171–178.
- [64] R. Kashyap, S. N. Srivastava, and S. C. Srivastava, “Influence of variables in nickel–manganese–zinc alloy plating from a sulphate bath,” (1985), *J. Appl. Electrochem.*, v. 15, N°. 1, pp. 23–27.
- [65] F. H. Assaf and A. A. Eissa, “Electrodeposition and Characterization of Zn–Ni–Mn Alloy from Sulfate Bath: Influence of Current Density,” (2015), *Electrochem. Sci.*, v. 10, pp. 5465–5478.
- [66] F. H. Assaf, A. A. Eissa, and M. M. Abou–Krisha, “Electrodeposition Mechanism of Zn–Ni–Mn Alloy at Different Time Intervals,” (2018), *Russ. J. Appl. Chem.*, v. 91, N°. 3, pp. 510–519.
- [67] S. Fashu, C. D. Gu, J. L. Zhang, H. Zheng, X. L. Wang, and J. P. Tu, “Electrodeposition, Morphology, Composition, and Corrosion Performance of Zn–Mn Coatings from a Deep Eutectic Solvent,” (2015), *J. Mater. Eng. Perform.*, v. 24, N°. 1, pp. 434–444.
- [68] B. Abedini, N. Parvini Ahmadi, S. Yazdani, and L. Magagnin, “Electrodeposition and corrosion behavior of Zn–Ni–Mn alloy coatings deposited from alkaline solution,” (2020), *Trans. Nonferrous Met. Soc. China*, v. 30, N°. 2, pp. 548–558.
- [69] K. Chat–Wilk, E. Rudnik, and G. Włoch, “Effect of Chloride and Sulfate Ions on Electrodeposition and Surface Properties of Alloys Produced from Zinc–Nickel–Manganese Gluconate Baths,” (2022), *J. Electrochem. Soc.*, v. 169, N°. 9, p. 092515.
- [70] R. KASHYAP, S. K. SRIVASTAVA and S. C. SRIVASTAVA, “The role of addition agents In the Electrodeposition Of ni-mn-zn alloys From a Sulphate bath, “1986, *Surface and Coatings Technology*, v. 28, pp 129 – 137.
- [71] Harriet Jill Kimpton, “The Production and Properties of Zinc–Nickel Zinc–Nickel–Manganese electroplat,” 2002, PhD thesis, Loughborough University.
- [72] S. Fashu and R. Khan, “Studies on electrochemical deposition of novel Zn–Mn–Ni ternary alloys from an ionic liquid based on choline chloride,” (2017), *Prot. Met. Phys. Chem. Surfaces*, v. 53, N°. 1, pp. 118–126.
- [73] M. M. Abou–Krisha, F. H. Assaf, O. K. Alduaij, and A. A. Eissa, “Deposition Potential Influence on the Electrodeposition of Zn–Ni–Mn Alloy,” (2017), *Trans. Indian Inst. Met.*, v. 70, N°. 1, pp. 31–40.
- [74] B. Abedini, N. Parvini, S. Yazdani, and L. Magagnin, “Structure and corrosion behavior of Zn–Ni–Mn / Zn–Ni layered alloy coatings electrodeposited under various potential regimes,” (2019), *Surf. Coat. Technol.*, v. 372, pp. 260–267.

# ***Chapter II***

## ***Materials and experimental techniques***

---

*This chapter outlines the procedure used in the experiments and conditions employed in this study for preparing Ni–Mn and Zn–Ni–Mn coatings. It also describes the fundamental aspects of various employed characterization techniques. These techniques include Scanning Electron Microscopy (SEM), Energy Dispersive Spectroscopy (EDS), and X–ray Diffraction (XRD), which are respectively used to analyze the morphology, chemical composition, and crystalline structure of the obtained coatings. Additionally, the chapter focuses on the use of Linear Tafel Polarization (LTP) and electrochemical impedance (EIS) methods for investigating the corrosion resistance of the as prepared coatings.*

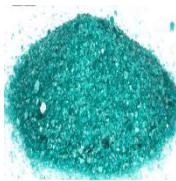
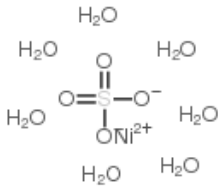

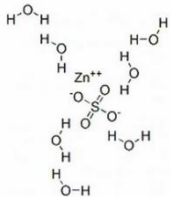

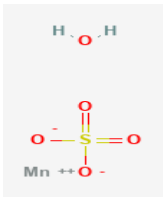

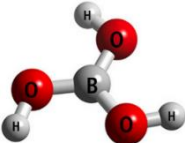
---


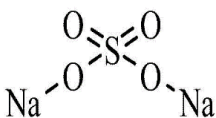

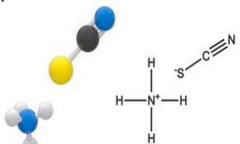
In this study, Ni–Mn and Zn–Ni–Mn coatings were prepared, onto a conductive Cu surface, by electrodeposition method. The essential instruments consist of the potentiostat, the electrolyte solution containing metal ions, and the electrochemical cell equipped with different electrodes. Further details for each component will be provided below.

## II.1. Chemical products

The chemical products, which are of analytical grade, are employed in their original state, without undergoing any purification (Table II.1).

**Table II.1:** Different chemical products used for the elaboration of thin films.

Chemicals products	Structure	Chemical formula	scientific name	The function of chemical products
		$\text{NiSO}_4 \cdot 7\text{H}_2\text{O}$	Nickel Sulfate hepta-hydrate	$\text{Ni}^{2+}$ source
		$\text{ZnSO}_4 \cdot 7\text{H}_2\text{O}$	Zinc sulfate hepta-hydrate	$\text{Zn}^{2+}$ source
		$\text{MnSO}_4 \cdot 7\text{H}_2\text{O}$	Manganese sulfate hepta-hydrate	$\text{Mn}^{2+}$ source
		$\text{H}_3\text{BO}_3$	Boric acid	Improve the alloy quality by the generation of hydrogen bubbles

		NaSO <sub>4</sub>	Sodium sulfate	electrolytic support
		NH <sub>4</sub> SCN	Ammonium thiocyanate	Complexing agent

## II.2. Bath preparation

The electrodeposition of Ni–Mn and Zn–Ni–Mn films relies on different baths [1, 2]. In this investigation, we favored a sulfate bath with the addition of ammonium thiocyanate. The preparation of all aqueous solutions exclusively involved distilled water. All experiments were conducted in an open–air environment at room temperature. Each test uses a freshly made sample solution to avoid compositional changes that can affect the materials' electrochemical responses. The pH solution value was maintained constant at pH = 3.5 and different additives concentrations were also kept constant: H<sub>3</sub>BO<sub>3</sub> (0.2 M), NaSO<sub>4</sub> (0.3 M) and NH<sub>4</sub>SCN (0.05 M).

**Table II.2.** Composition of the electroplating baths.

Bath	NiSO <sub>4</sub> (M)	MnSO <sub>4</sub> (M)	ZnSO <sub>4</sub> (M)
Ni	0.2	-	-
Mn	-	0.2	-
Zn	-	-	0.2
Ni-Mn	0.2	0.5/0.1/0.2/0.3	-
Ni-Zn	0.2		0.2
Zn-Mn	-	0.2	0.2
Ni-Zn-Mn	0.2	0.5/0.1/0.2/0.4	0.2

## II.3. Experimental setup

All the electrochemical measurements were performed utilizing a PGP201 Potentiostat/Gavanostat under the control of a microcomputer equipped with "Volta Master" software and directly connected to a three–electrode cell system. A saturated Ag/AgCl electrode, Pt wire and a high–purity rectangular copper (Cu) sheet were

utilized as reference electrode, counter electrode, and working electrode, respectively, as illustrated in figure II.1.

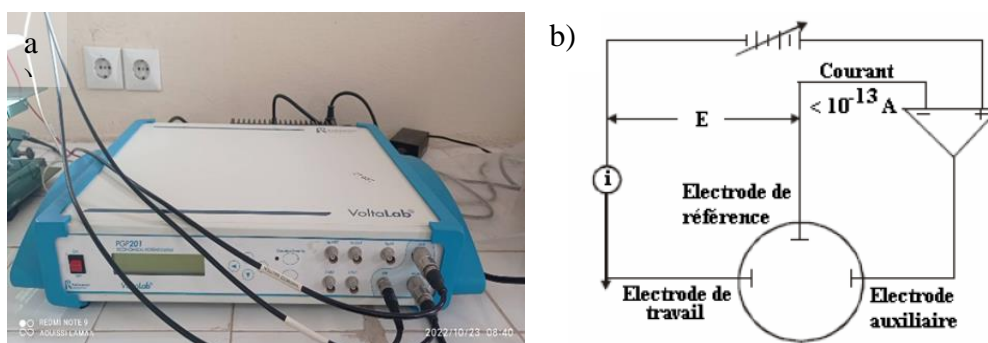


**Figure II.1.** Electrochemical measurements device.

### II.3.1. Potentiostat

The potentiostat is commonly used in electrochemistry research and analysis, it is a specialized electrical instrument used in electrochemistry for studying electrochemical phenomena and the electrochemical characterization of various metals, it can control and measure electrochemical reactions with high accuracy and precision, making it a valuable tool in the study of electrochemical kinetics and thermodynamics. The potentiostat is connected to the cell through

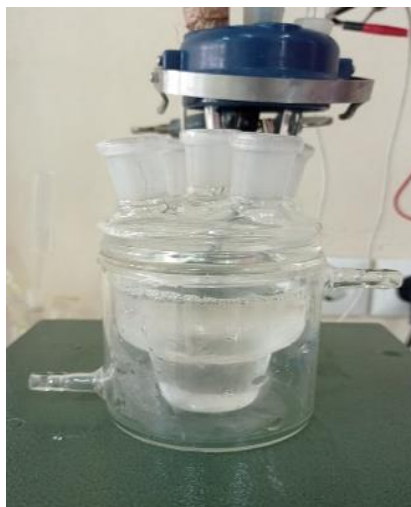
electrodes (cathode, anode, reference). Its principle is based on measuring the potential difference between the working electrode and the reference electrode. To achieve this, the electrodes are placed in the cell, the electrical connections are made between electrodes, potentiostat, and computer. The Volta Master software is used to apply the current or cell voltage, along with the desired duration for the electrodeposition experiment.



**Figure II.2.** a) Photograph of the potentiostat/ galvanostat. b) Schematic representation of a potentiostat/galvanostat and its electronic circuit.

### II.3.2. Electrochemical cell

The electrochemical cell is a Pyrex glass cell with a 100 ml capacity that contains an electrolyte (the compositions are given in table II.2). The cell (Figure II.3) is capped with a lid featuring five openings for the insertion of three electrodes (working, auxiliary, and reference), a thermometer, and a degassing tube if required. These electrodes, immersed in the electrolytic bath, play a crucial role in facilitating redox reactions.



**Figure II. 3.** Photograph of the electrochemical cell.

### II. 3. 3. Electrodes

#### II.3.3.1. Working electrode

The working electrode is the site where the oxidation or reduction reactions occur in response to potential variations. Its potential is contingent on the activity and, consequently, the concentration of the ionic species under measurement. The working electrode can be composed of various conductive materials, such as metals (gold, silver, nickel, copper...), organic materials (conductive polymers) and non-metallic materials (graphite or glassy carbon).

The selection of the working electrode is determined by considerations such as stability, polarization range, lattice parameters, and the studies intended for later characterization of the deposited material. In our research, we employed copper as the working electrode (figure II. 4).





**Figure II.4.** Working electrode used in experimental set up (copper substrate).

### II.3.3.2. Reference electrode

In our experimental setup, the reference electrode, depicted in figure II.5, is a saturated Ag/AgCl electrode (VWR, France). This electrode operates as a half-cell with a known and constant potential. It consists of silver wire partially covered with AgCl and immersed in a saturated KCl solution. At room temperature, its potential relative to the normal hydrogen electrode is approximately 205 mV. vs. NHE. This potential may vary based on the temperature of the electrolytic bath. Crucially, the reference electrode serves as a benchmark for the potentiostat, allowing it to apply a precise potential difference between this electrode and the working electrode. This precision ensures accurate control over the potential applied to the working electrode.



**Figure II.5.** Reference electrode Ag/AgCl electrode.

### II.3.3.3 Auxiliary electrode

The auxiliary electrode is the electrode that is used in electrochemical systems to complete the electrical circuit and support the electrochemical reaction at the working electrode. The auxiliary electrode, also known as a counter electrode, is typically fabricated from an inert material that does not participate in the chemical reaction or process. In a three–electrode system, used in electrochemical measurements, the auxiliary electrode is also used to apply a voltage or a current to the system to control the reaction rate or potential of the working electrode. The auxiliary electrode serves for several important functions, including completing the electrical circuit, maintaining the charge balance in the system, and preventing the buildup of reaction byproducts. It is often positioned near the working electrode to ensure efficient electron exchange between the two electrodes.

For our experiments, the auxiliary electrode is the platinum electrode (Figure II.6). Positioned parallel to the working electrode, it aims to achieve deposits of more or less uniform quality. Nevertheless, this metallic electrode is prone to fouling through processes like adsorption or oxidation.



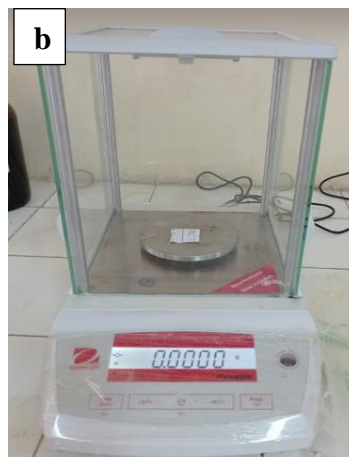
**Figure II. 6.** Photograph of the auxiliary electrode.

### II. 3. 4. Other devices used in the experiments

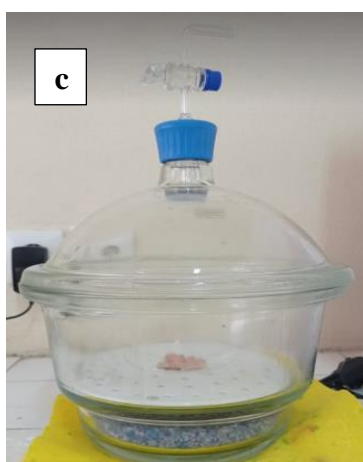
Other devices including polisher, electronic balance, desiccator, PH meter, and magnetic agitator are used in our experiments and shown in figure II.7.



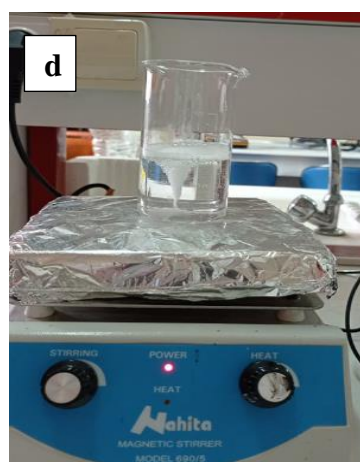
**Polisher**



**Electronic balance**



**Desiccator**



**pH meter**



**Magnetic agitator**

**Figure II.7** a) Polisher, b) electronic balance, c) desiccator, d) PH meter, e) Magnetic agitator.

## II. 4. Preparation of the substrates

In order to establish a condition where the metallic surface layer will adhere and to create a thin layer with a smooth surface, the employed substrates must be treated before each manipulation. Surface preparation plays a crucial role in electroplating, involving a number of steps, the order of which is based on the general state of the surface. Before undergoing a surface electrochemical treatment, the substrate's surface is mechanically prepared by using successively emery paper with decreasing granulometry (800, 2000, and 2400). Next, the surface is chemically prepared by being stripped for a minute using 0.2 M of diluted H<sub>2</sub>SO<sub>4</sub> sulfuric acid to remove any foreign objects that may be present on the surface and to dissolve or separate any chemical compounds that may be there (oxide layer or other metallic compounds). Then, the surfaces of the substrates were degreased and cleaned for 5 min in a 99.5% acetone solution, followed by a rinse with distilled water, carefully dried with absorbent paper, and stored in airtight containers.

## II. 5. Experimental Methodology

### II.5.1. Electrochemical techniques used for the kinetic study

In this work, several electrochemical techniques were used. These methods can be applied to investigate both the reaction mechanisms occurring during an electrodeposition process and the actual deposit created. The employed techniques are cyclic voltammetry, and chronoamperometry.

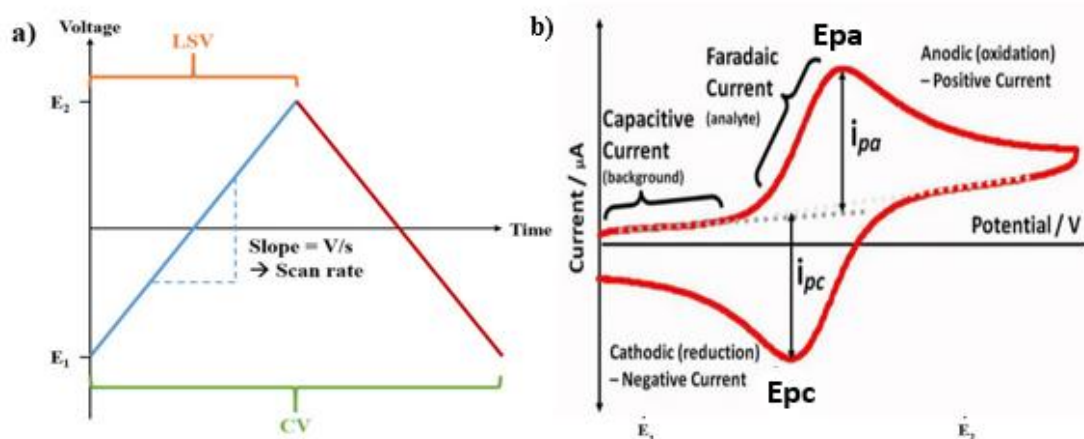
#### II.5.1.1. Cyclic voltammetry

CV is a commonly used electroanalytical method for the investigation of the interface between an electrode and an electrolyte providing a comprehensive overview of all electrochemical processes taking place at the electrode. In this method, three electrodes are submerged in the solution and connected to the potentiostat. The working electrode has a regularly changing potential compared to the reference electrode. The reference electrode maintains a constant potential, irrespective of the solution. The resulting electric current from charge transfer at the electrode–electrolyte interface is measured between the working and counter electrodes.

### a) Cyclic Voltammetry principle

The concept of cyclic voltammetry is based on immediately following a potential scan (in a regime of pure diffusion) with a return scan to the initial potential, typically at the same speed, completing a full potential cycle. The "return" curve is obtained by reversing the direction of the potential scan at a time  $t_\lambda$ , corresponding to an inversion potential  $E_\lambda$ . The current  $I$  in the circuit is measured either continuously or at specific intervals. This current, associated with the electronic transfer facilitating the reduction of metal ions at the electrode surface (cathode), is primarily composed of two distinct currents: the faradaic current ( $I_f$ ) originating from the redox reactions of the analyzed elements at the electrode/solution interface, and the capacitive current  $I_c$ .

$$I = I_f + I_c \quad (\text{II. 1})$$



**Figure. II. 9.** Schematic illustration of potential variation at a designated scan rate.

$i_{pa}$  (anodic peak current) and  $i_{pc}$  (cathodic peak current).

$E_{pa}$ ,  $E_{pc}$ : Anodic and cathodic peak potentials.

This method rapidly detects reaction steps by adjusting the scan rate, revealing insights into reaction nature and mechanisms through peak characteristics. Voltammetry assesses redox system reversibility using a triangular signal on a stationary electrode in a non-agitated electroactive substance solution, with the potential difference between oxidation and reduction peaks indicating reversibility (Figure II.10) [2].

- **Reversible (fast) system:** In situations where electron transfer kinetics are rapid (reversible) compared to reactant diffusion, the peak current is determined by the following expression: (Randles–Sevcik relationship).

$$I_p = 0.269An^{3/2}D_{ox}V^{1/2} \quad (\text{II.2})$$

$$E_p = E_{1/2} - \frac{0.029}{n} \quad (\text{II.3})$$

- **Quasi-reversible system:** For semi-rapid electron transfer kinetics, the current is described by the following relationship:

$$I_p = 0.269n^{3/2}D^{1/2}C_{ox}KV^{1/2} \quad (\text{II.4})$$

- **Irreversible (slow) system:** In the case of slow (irreversible) electron transfer kinetics, the expression of the peak current is represented by the following equation:

$$I_p = 0.269 \cdot A \cdot n\alpha^{3/2} \cdot D_{ox}^{1/2} \cdot C_{ox} \cdot V^{1/2} \quad (\text{II.5})$$

$D_{ox}$ : the diffusion coefficient of the reactive species ( $\text{cm}^2/\text{s}$ ),

$C_{ox}$ : the concentration of the reacting species within the electrolyte in  $\text{mol}/\text{cm}^3$ .

$n$ : the total number of transferred electrons,

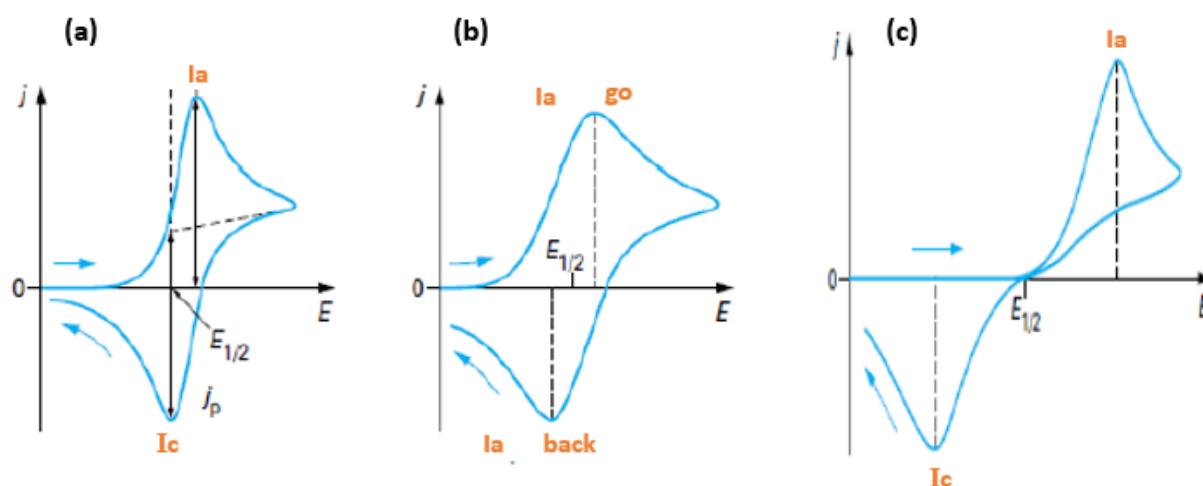
$V$ : the scan rate ( $\text{V}/\text{s}$ ),

$A$ : the electrode surface area ( $\text{cm}^2$ ),

$I_p$ : the peak current intensity (A),

$\alpha$ : the transfer coefficient,

$K$ : the reaction rate constant.



**Figure II. 10.** Schematic illustration of different CV curves depending on the system's speed.

(a) Reversible system, (b) Quasi-reversible system, and (c) Irreversible system.

### II.5.1.2. Chronoamperometry

In natural convection environments, chronoamperometry serves as a transient technique associated with voltammetry. Within voltammetric studies, the continual fluctuation of the electrode potential in a non-stationary natural convection setting poses a challenge in analyzing the response,  $i = f(t)$ . To enhance the quantitative interpretation of the system's electrochemical response, one of the two controlled electrical parameters is kept constant. This approach entails applying a potential for a specific duration ( $t$ ) and noting the resulting current over time. The resulting graph is termed a current transient (Fig.II.11). Such a transition is consistently followed by the current transition as described by the Cottrell equation. (II. 6)

$$i = n.F.C(D/\pi t)^{1/2} \quad (\text{II.6})$$

$i$ : the current density ( $\text{A}\cdot\text{cm}^{-2}$ ),

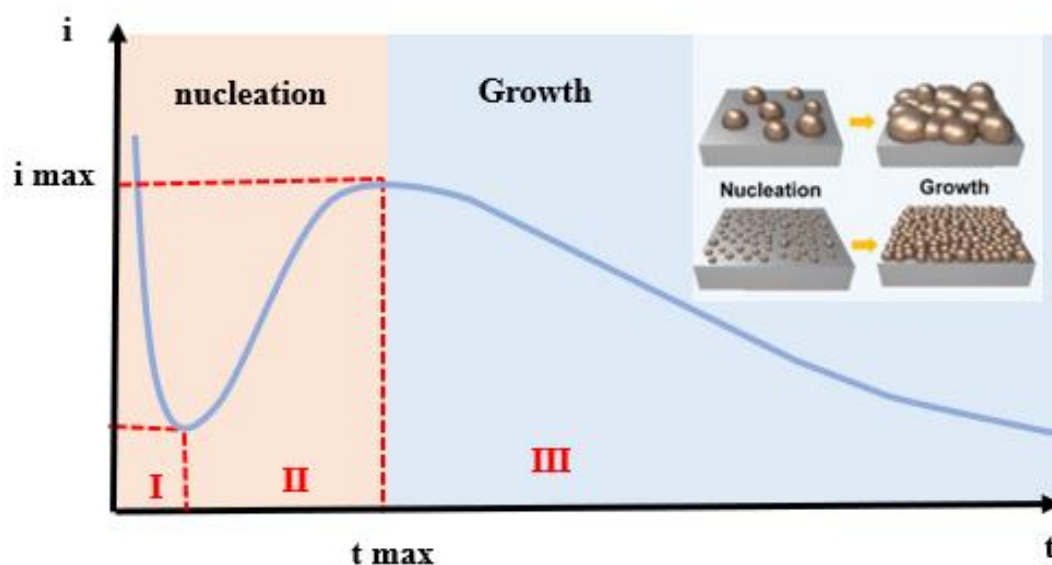
$n$ : the number of exchanged electrons,

$F$ : the Faraday constant ( $\text{C}/\text{mol}$ ),

$D$ : the diffusion coefficient of species ( $\text{cm}^2\cdot\text{s}^{-1}$ ),

$C$ : the concentration of species ( $\text{mole}\cdot\text{cm}^{-3}$ ),

$t$ : the time of reaction (s).



**Figure II.11.** Theoretical potentiostatic transient curve (current–time).

- i) In section I, the burden of the double layer and the time required for germ development are both addressed.
- ii) In phase II, the current rises concurrently with the seeds' expansion over the electrode surface, reaching a maximum value at time  $t_{\max}$ .
- iii) In section III, the diffusion of electroactive species toward the totally covered electrode surface limits the current.

## II.5.2. Electrochemical methods for corrosion test

Several commonly used corrosions testing techniques are utilized to assess a material's resistance to corrosion. These testing methods span from basic visual inspections, such as the Loss Mass Method, to more advanced tests like Linear Tafel Polarization (LTP) and Electrochemical Impedance Spectroscopy (EIS).

### II.5.2.1 Loss mass method

The "loss mass method" in corrosion testing quantifies the mass reduction of a material exposed to a corrosive environment over a specified period, providing a means to evaluate the corrosion rate. This method involves weighing the test specimen both before and after exposure to the corrosive environment. The difference in mass before and after the test provides an indication of the amount of material that has been corroded. This approach is frequently used to evaluate the corrosion resistance of different materials and coatings. It is a frequently used approach because it is straightforward, dependable, and able to provide quantitative data on the corrosion performance of materials-

The corrosion rate is characterized as the weight loss per unit of surface area and time, expressed in ( $\text{g}/\text{cm}^2/\text{year}$ ). It can be calculated using the following equation:

$$\tau = 360 \frac{\Delta m}{St} \quad (\text{II.7})$$

$$\Delta m = m_f - m_i \quad (\text{II.8})$$

$m_i$ : Mass of the sample before the test (g).

$m_f$ : Mass of the sample after the test (g).



S: Immersed surface area (in our study,  $S = 1\text{cm}^2$  for all samples).

t: Duration of the experiment in hours, in our study,  $t = 48\text{ h}$  for corrosion tests.

### II.5.2.2 Open Circuit Potential (OCP)

In order to stabilize the system throughout the electrochemical experiment, all subsequent electrochemical measurements were performed at the open circuit potential (OCP) for 20 minutes. OCP is known as rest potential or the spontaneous system potential when the circuit is open, over time this potential tends to stabilize. When both oxidant and reducer species of the same redox pair coexist at the same time, the potential in the quasi-stationary state represents the thermodynamic potential " $E_{th}$ ". However, the presence of same multiple redox couples, as in the corrosion process, the measured rest potential will correspond to the mixed (out-of-equilibrium) potential or corrosion potential [3].

The corrosion mechanism at the passive film/electrolyte interface was analyzed using linear EIS. Measurements were conducted at the OCP with a 10-mV amplitude, covering a frequency range from 0.01 to 10000 Hz, and a specified sampling rate. In this frequency range, stable EIS results can be obtained.

### II.5.2.3. Linear Tafel Polarization (LTP)

Linear Tafel Polarization (LTP) is a frequently used method for determining the rate of corrosion. This method involves applying a systematic potential variation to a sample immersed in an electrolyte, polarizing it from cathodic to anodic potentials, and measuring the current density that results [3]. The Butler-Volmer equation serves as a fundamental electrical equation, providing a general description of the relation between potential,  $E$ , and current density,  $i$ , in electrochemical systems, expressed as  $i = f(E)$ .

$$i = i_c e^{\frac{(\alpha)nf}{RT}\eta} - i_a e^{-\frac{(1-\alpha)nF}{RT}\eta} \quad (\text{II.9})$$

In the mixite potential  $i_c = i_a = i_0$  (II.10)

$$i = i_0 \left( e^{\frac{(\alpha)nf}{RT}\eta} - e^{-\frac{(1-\alpha)nF}{RT}\eta} \right) \quad (\text{II.11})$$

- $i$ : total current density ( $\text{A. m}^{-2}$ )

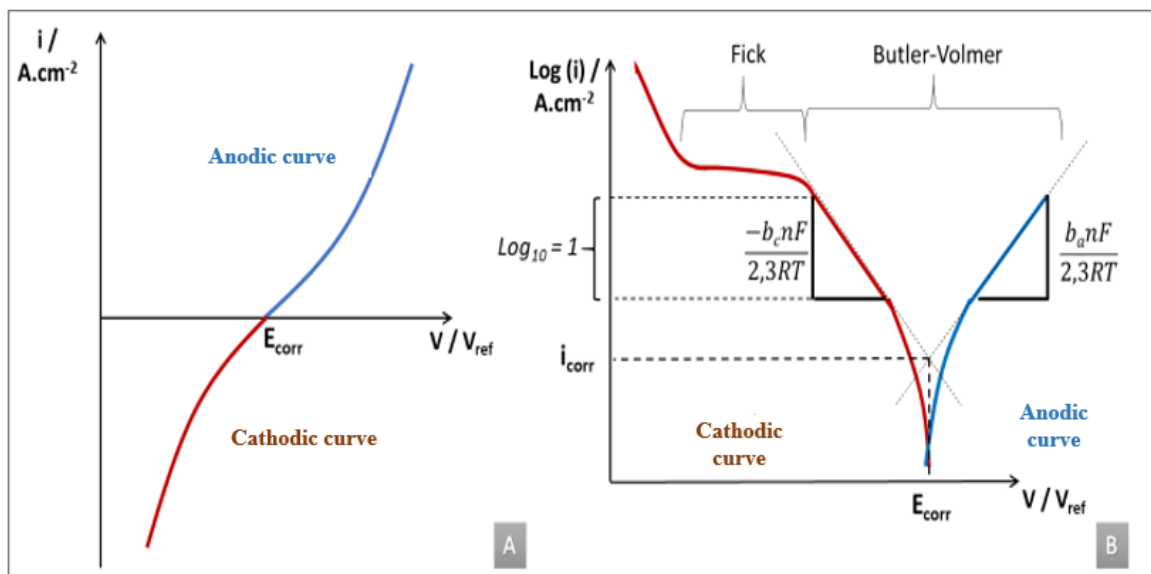
- $i_0$ : exchange current density (including the rate constant)
- $i_c$ : cathodic current density.
- $i_a$ : anodic current density
- $\eta = E - E_{eq}$ : overpotential or polarization (V)
- $n$ : number of electrons involved in the reaction rate-determining step.
- $F$ : Faraday's constant ( $C \cdot mol^{-1}$ )
- $R$ : gas constant ( $J \cdot K^{-1} \cdot mol^{-1}$ )
- $\alpha$ : Transfer charge coefficient.

For  $\eta \gg 100$  mV, the term  $i_c$  is negligible, and only the anodic term remains.

$$i = i_0 \left( -e^{\frac{(1-\alpha)nF}{RT}\eta} \right) \quad (II.12)$$

For  $\eta \ll 100$  mV, the term  $i_a$  is negligible, and only the cathodic term remains.

$$i_T = i_0 e^{\frac{\alpha nF}{RT}\eta} \quad (II.13)$$



**Figure II.12.** Schematic representation of a current–potential curve and Tafel lines [3].

The intersection of the corresponding two lines (Tafel slopes) allows for the determination of the corrosion potential ( $E_{corr}$ ) and the corrosion current ( $i_{corr}$ ) as indicated in figure II. 12.  $E_{corr}$  potential serves as an indicator of a material's susceptibility to corrosion, with a more negative value indicating a greater tendency for the metal to corrode. In contrast, the corrosion current ( $i_{corr}$ ) is linked to the corrosion rate of the immersed metal.

The polarization resistance is determined by evaluating the tangent to the polarization curve at  $i=0$  near the corrosion potential. However, assessing the corrosion current with this equation requires prior determination of the Tafel slopes ( $\beta_a$  and  $\beta_c$ ). Polarization resistance ( $R_p$ ) is calculated using the Stern and Geary equation:

$$R_p = \frac{\beta_c \beta_a}{2.303 i_{cor} (\beta_c + \beta_a)} \quad (\text{II.14})$$

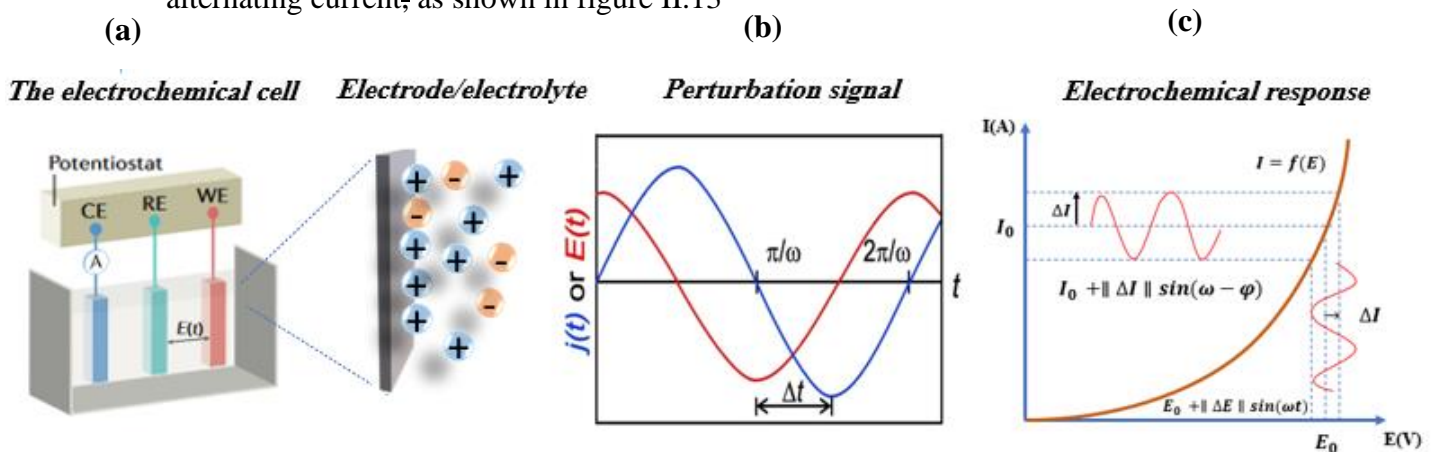
In our work, LTP experiments were performed last in the sequence of measurements following approximately 1 hour of immersion in acid medium NaCl 3.5 %, at ambient temperature. LTP experiments were conducted at  $-0.1 \text{ VOCP} < \text{OCP} < 0.1 \text{ VOCP}$  with a scan rate of 10 mV/s.

#### II.5.2.4. Electrochemical impedance spectroscopy

EIS is one of the most important electrochemical methods that enables the separation of contributions from different chemical and electrochemical phenomena occurring at the interface electrode /electrolyte.

##### II.5.2.4. 1. Principle

The fundamental concept of (EIS) is to polarize the cell at a constant voltage initially, followed by applying a slight additional voltage (or sometimes a current) to disturb the system. The input disturbance oscillates harmonically over time, thereby generating an alternating current, as shown in figure II.13



**Figure. II. 13.** a) Schematic illustration of corrosion cell, b) "Voltage–Current Relationship: Impedance Insight" c) "Linear Electrochemical Response Measurement"

The system's response analysis provides details on the interface, including its structure and the reactions occurring. The perturbing signal  $E(t)$  applied to electrochemical impedance and the resulting current  $I(t)$  are often expressed as follows.

$$E(t) = E_0 + \Delta E \sin(\omega t)$$

The relationship between the applied frequency ( $f$ ) and the radial frequency ( $\omega$ ) is determined by the following equation.

$$\omega = 2\pi f \quad (\text{II.16})$$

The signal in a linear system has an amplitude that differs from  $I_0$  and is phase-shifted  $\theta$  (Equation).

$$I(t) = I_0 \sin(\omega t + \theta) \quad (\text{II.17})$$

$t$  is the time and  $I_0$  is the oscillation amplitude of the current.

#### II.5.2.4. 2. Nyquist and Bode diagrams

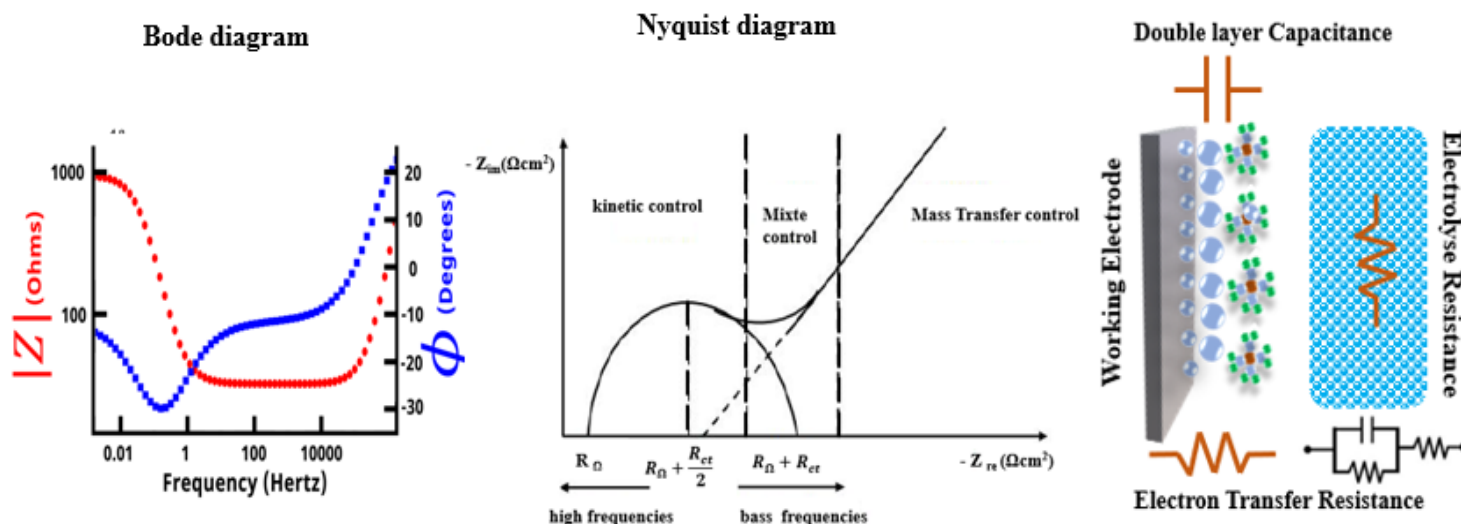
The EIS technique can be used to get a wide range of electrical data. Using this technique, it becomes possible to illustrate the processes occurring within an electrochemical cell represented as an electrical impedance  $Z$  by employing equivalent circuits comprising different combinations of resistances ( $R$ ), capacitors ( $C$ ), and/or inductances ( $L$ ). The plot of the two polar components  $Z$  and  $\phi$  as a function of frequency is known as the Bode diagram. Also, the representation in the complex plane ( $Z_r$  vs.  $Z_j$ ) is the Nyquist diagram.

The system's impedance ( $Z$ ) can be estimated using an equation that resembles Ohm's law.

$$Z = \frac{E(t)}{I(t)} = \frac{E_0 \sin(\omega t)}{I_0 \sin(\omega t + \theta)} = Z_0 \frac{\sin(\omega t)}{\sin(\omega t + \theta)} \quad (\text{II.18})$$

where  $Z$ ,  $E$ ,  $I$ ,  $\omega$ , and  $\theta$  are impedance, potential, current, angular frequency, and phase shift between  $E$  and  $I$ , respectively.

The Nyquist representation enables the observation of diverse loops and lines on the impedance diagram, while the Bode representation provides a comprehensive view of the frequency domain. Interpreting the diagrams enables the identification of various processes occurring at the electrode. In specific cases, particularly when the time constants of elementary steps are not well-separated, it becomes essential to model the impedance of the electrochemical system using that of an equivalent electrical circuit.



**Figure. II.14.** Bode diagram, Nyquist diagram and Equivalent Electrical Circuit

The frequency analysis of electrochemical impedance allows for the differentiation of various elementary elements based on their characteristic frequency (or time constant). Rapid electrochemical phenomena, such as charge transfer, are observed in the high-frequency domain, while slower processes like diffusion and adsorption occur at lower frequencies.

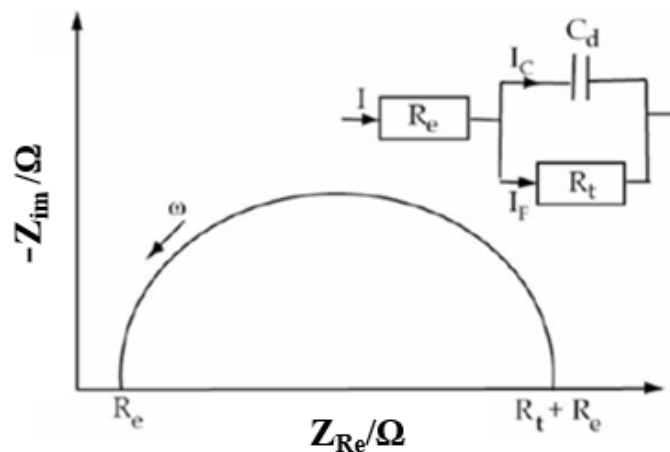
#### II.5.2.4.3. Charge transfer

In electrochemical models, the faradic current  $I_F$  involves electron transfer during redox reactions at interface and double layer charge current  $I_C$  are expression of the overall current ( $I$ ) flowing through the system.

$$I = I_F + I_C \quad (\text{II.19})$$

The interface can be represented, in the case of low amplitude perturbations, by a semicircle in the Nyquist plot, and can be represented by an equivalent electrical circuit,

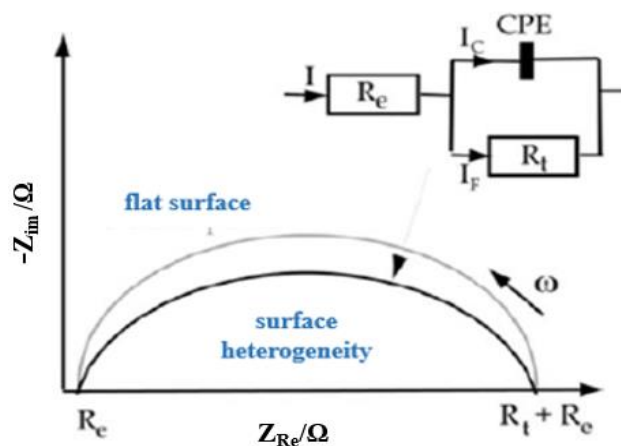
called the Randles circuit (Figure II.15). The resistance,  $R_e$ , of the Randles circuit corresponds to the resistance of the electrolyte of finite conductivity. The phenomenon of charging at the electrode/solution interface causes the appearance of a capacitive current (represented by the capacitance  $C_d$ ). The charge transfer resistance,  $R_t$ , is traversed by the faradaic current,



**Figure II.15.** A Nyquist plot depicting the electrochemical impedance associated with a charge transfer process and its Equivalent Electrical Circuit [4]

#### II.5.2.4.4. surface heterogeneities

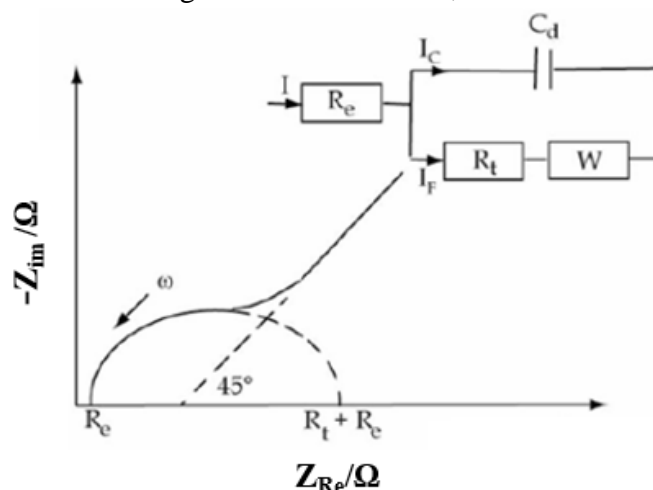
In some cases, modeling the capacitive loop at high frequencies with an equivalent electrical circuit is difficult due to the presence of surface heterogeneities on the electrode. The reaction sites are not uniformly distributed and the half-circle representing the charge transfer resistance and the double layer capacitance in the Nyquist plot is flattened (Figure II. 16). Modeling the behavior of the double layer with a capacitance becomes imperfect. It is then necessary to add a time constant to this capacitance, called a constant phase element (CPE).



**Figure II. 16.** Representation of the electrochemical impedance of a heterogeneous surface electrode and an equivalent electrical circuit in the Nyquist plane [5].

#### II.5.2.4.5. Diffusion in an infinitely thick layer

When the transport of matter within a layer of infinite thickness limits the process to the surface of the electrode, the impedance, in the Nyquist plot, is represented by a capacitive loop, related to charge transfer, for high frequencies and by a straight line forming an angle of  $45^\circ$  with the x-axis for low frequencies (Figure II.17). This corresponds to the diffusion of species through the layer of infinite thickness (through the immobile electrolyte, for example). The equivalent electrical circuit corresponds to a capacitance of the double layer,  $C_d$ , in parallel with the diffusion impedance,  $W$ , connected in series with the charge transfer resistance,  $R_t$ .

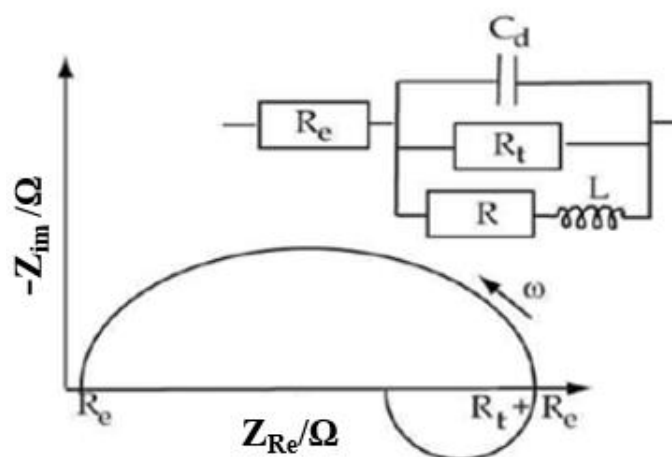


**Figure II. 17.** Representation, in the Nyquist plot, of the electrochemical impedance where diffusion through an infinite layer is the limiting process of corrosion and its equivalent electrical circuit [6].

The equivalent electrical circuit substitutes the Warburg impedance,  $W$ , with the impedance of diffusion through macroscopic pores, represented as  $C_d$ . This parameter considers both the thickness of the diffusion layer and the diffusion coefficient of the diffusing species within the layer.

#### II.5.2.4.4. Adsorption step

In corrosion processes, an intermediate adsorption step of a species can occur at the electrode. This is manifested on the impedance diagram, represented in the Nyquist plot, by an inductive loop (Figure II.18). It is modeled by a resistance  $R$  and an inductance  $L$  in parallel with the Randles circuit (Figure II.18).



**Figure II. 18.** Representation of the Nyquist Plot of electrochemical impedance of adsorbed species on an electrode surface and its equivalent electrical circuit [7].

### II.5.3. Physical characterization techniques

Physical characterization techniques involve examining materials by measuring their interaction with electromagnetic radiation. A range of methods offers crucial insights into the composition, structure, and properties of materials, such as Scanning Electron Microscope (SEM), and Energy–Dispersive X–ray Spectroscopy (EDX)

In our study, we employed a scanning electron microscope (SEM), specifically the HITACHI TM–1000 model, in conjunction with energy dispersive X–ray analysis (EDX). Additionally, we utilized an X–ray diffractometer, X’ Pert Pro MPD Analytical,

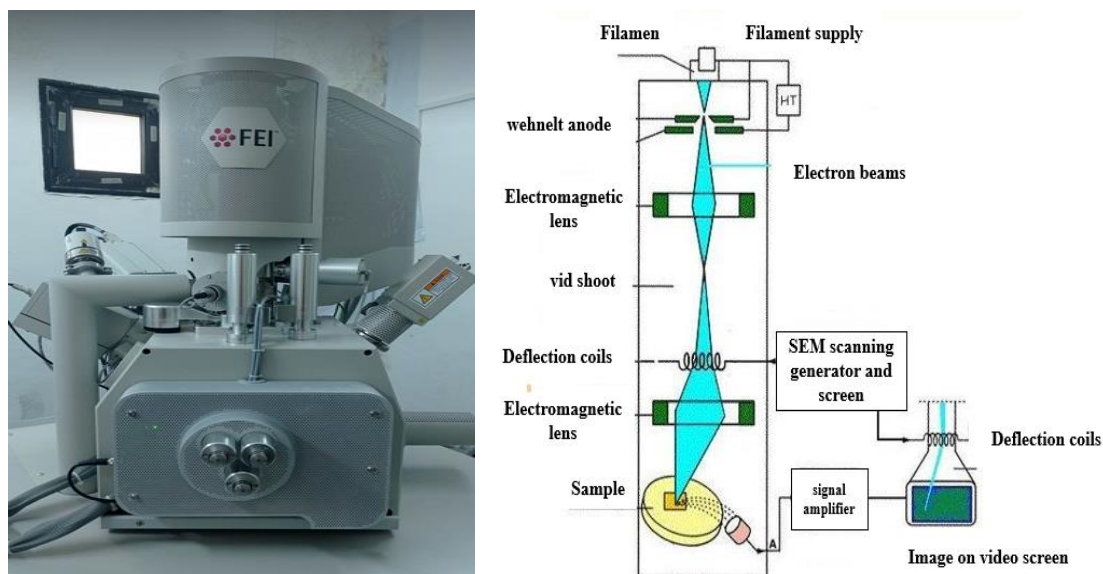


with a Cu K $\alpha$  radiation source ( $\lambda_{\text{Cu}} = 1.54059 \text{ \AA}$ ). X-ray diffraction (XRD) data were gathered within the angular range of  $2\theta$  ( $10\text{--}80^\circ$ ) with a step size ( $\Delta 2\theta = 0.02^\circ$ ).

### II.5.3.1. Scanning Electron Microscope (SEM)

SEM allows for morphological observations and the distinction of details on the scale of hundredths to nanometers, thanks to its depth of field. The resulting images have a three-dimensional quality of definition. Under the impact of the electrons beam, there is backscattering of electrons from the incident beam, emission of low-energy secondary electrons resulting from the ionization of atoms in the sample, and emission of Auger electrons and X-rays characteristic of the elements present in the sample. The SEM detector recovers a mixture of variable proportions of secondary electrons and backscattered electrons, the proportion of which depends on the primary energy, the distance between the sample and the objective, the angle of incidence of the primary beam, and the observed material. Secondary electrons allow the distinction of surface topography details of the sample, while backscattered electrons allow for observation of chemical contrast [8].

The fundamental concept of this method is based on synchronizes an electron beam's movement on a sample with a cathode-ray screen (figure.II.19). As the beam penetrates the sample, elastic interactions with the nucleus cause scattering, and inelastic interactions lead to gradual energy loss through ionization and radiative processes.



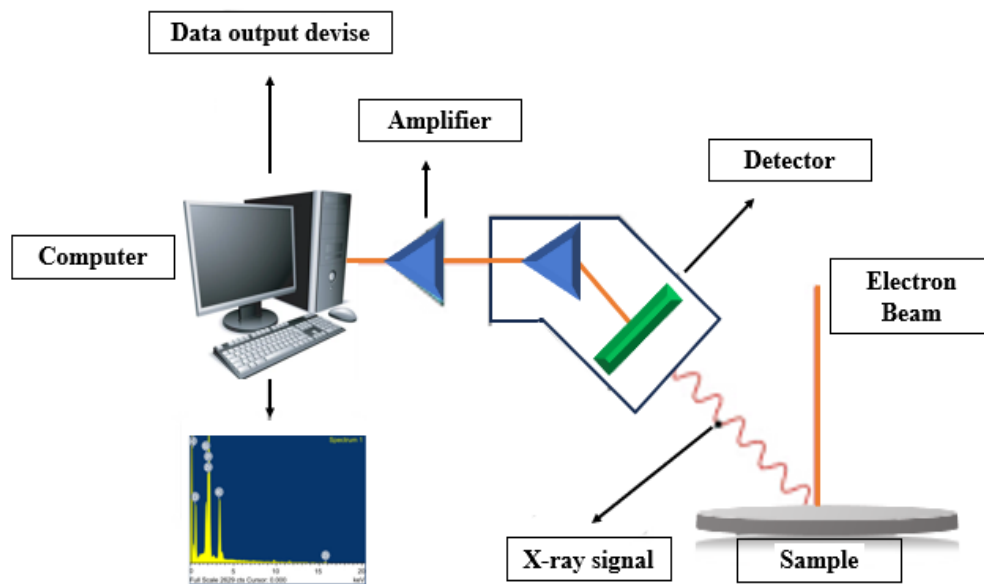
**Figure II. 19.** A photograph of a scanning electron microscope: HITACHI TM-1000.

### II.5.3.2. Energy Dispersive Spectroscopy (EDX)

EDX is a method that utilizes X-rays to characterize the elemental composition of materials, providing a nondestructive testing method for determining the composition of the material. Its use is further expanded to include examining the chemical structure and features of materials. The EDX technique is essential and can be obtained as a complement to SEM images.

- **EDS's fundamental principle**

The foundational principle of the EDX technique aligns with the periodic table's basic concept, wherein each element's unique atomic configuration leads to distinct peaks in an X-ray radiation spectrum. When a sample is exposed to a high-energy beam of particles like electrons, protons, or X-rays, it emits characteristic X-ray radiation. An energy-dispersive spectrometer can measure the energy of X-rays emitted from the specimen. During electron transitions from the L and M to the K shell, specific lines, K-alpha and K-beta, are generated in each electron shell. The detector has the ability to produce both K-beta and K-alpha emissions, giving rise to fluorescence photons through these transitions. The energy of an identifiable fluorescent photon corresponds to the energy difference between its initial and final orbitals.



**Figure II. 20.** Schematic illustration of EDS technique principle.

### II.5.3.3. X-Ray diffraction technique

(XRD) is a non-destructive method employed to examine the structure of crystalline materials, regardless of whether they are in bulk form, thin films, or nanowires. This method offers information about the nature of the deposited material, as well as crystal lattice parameters and average crystallite size. The symmetric method ( $\theta/2\theta$  analysis) is used to detect planes parallel to the sample surface. X-rays with a specific wavelength,  $\lambda$ , are directed at the material at a specific angle, known as the Bragg angle,  $\theta$ , causing the X-rays to reflect at the same angle on a family of lattice planes with a specific lattice distance  $d_{hkl}$ .

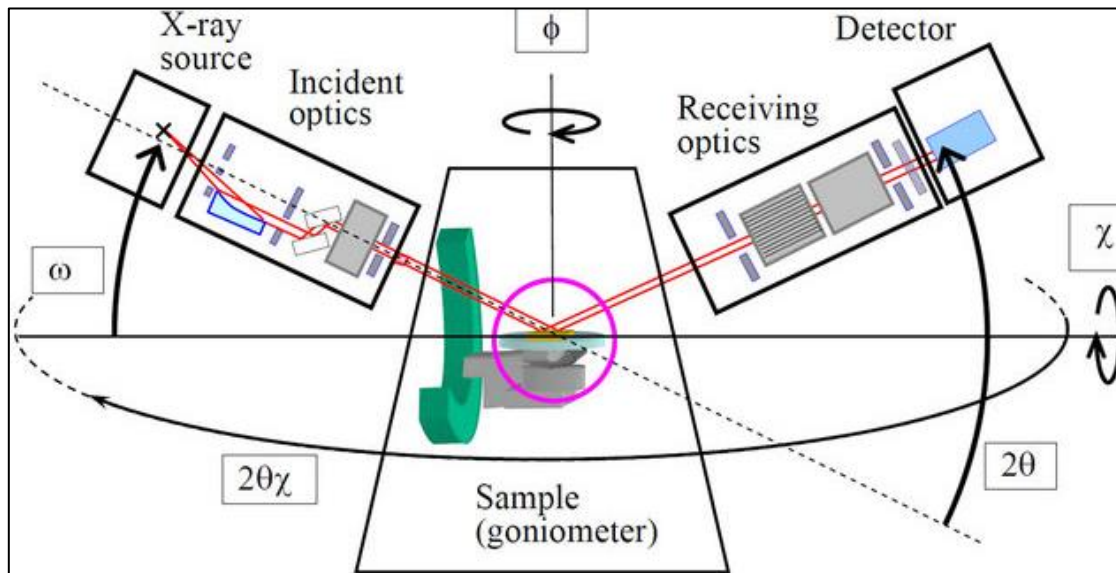
$$2d_{hkl} \sin(\theta) = n \cdot \lambda \quad (\text{II.20})$$

$d_{hkl}$ : Inter reticular distance separating planes of the same family (hkl).

$\lambda$ : Incident x-ray wavelength.

$n$ : The order of reflection in the family of parallel planes (hkl).

$\theta$ : The diffraction angles.



**Figure II. 21.** Schematic illustration of experimental device of X-ray diffraction technique[9]

For every set of lattice planes (hkl), a corresponding diffraction peak occurs in the sample at the angle  $\theta$ . These peaks collectively form a diffraction pattern that shows the intensity of diffracted X-rays relative to the diffraction angle. By the analysis of the

positions, intensities, widths, and shapes of these peaks, important information about the material's structural and microstructural properties can be obtained. The diffraction angles  $\theta$  provide insight into the interplanar distances  $d_{hkl}$ , which can be utilized to determine the phases present in the material by comparing the calculated interplanar distances with those stored in databases such as JCPDS files [9].

In certain instances, diffraction peaks may appear broader, indicating a potential decrease in the crystallites' size. The Scherrer equation is generally used to estimate the crystallites size. Initially developed for crystals with identical dimensions, shapes, and cubic symmetries, this equation allows for the estimation of the average crystallite size perpendicular to the diffraction planes.

$$D = \frac{K\lambda}{\beta \cdot \cos\theta} \quad (\text{II.21})$$

D: Average crystallite size (m)

k: is a Scherrer constant whose value is generally close to 1, with no dimensionless.

$\beta$ : is the full width at the half maximum (FWHM) (in rd).

$\lambda$ : Incident x-ray wavelength (m).

$\theta$ : The diffraction angle (rd).

The systematic study of the crystalline state was carried out on all the coatings using a diffractometer X'PERT PRO MPD PANALYTICAL in Bragg–Brentano ( $\theta$ – $2\theta$ ) geometry (Figure.II.22). The monochromatic radiation used was the  $K\alpha$  line of copper ( $\lambda_{Cu} = 1.54059 \text{ \AA}$ ). XRD data were gathered over the angular range  $2\theta$  ( $10 - 80^\circ$ ) with a step size of ( $\Delta 2\theta = 0.02^\circ$ ).



**Figure II. 22.** A photograph of the diffractometer X'PERT PRO MPD PANALYTICAL.

## II.6. Conclusion

To sum up, this chapter outlines the different experimental techniques and elaboration conditions utilized to investigate the nucleation, growth, and characterization of alloy deposits through electrochemical and physical methods. The characterization methods employed, providing valuable insights into the properties of the deposits are clearly described.

**References**

- [1] E. Brück, O. Tegus, D. T. Cam Thanh, N. T. Trung, and K. H. J. Buschow, “A review on Mn based materials for magnetic refrigeration: Structure and properties,” (2008), *Int. J. Refrig.*, vol. 31, N°. 5, pp. 763–770,
- [2] A. Benchettara, “Modification d’une électrode de graphite par des oxydes de métaux de transition—Application à la détection électrochimique de substances oxydable,” (2016), Doctorate thesis, *University of Houari Boumediene*
- [3] M. Minola, “Study of corrosion and corrosion protection mechanisms to reduce the electromagnetic signature of ship,” (2016). Doctorate thesis, *University Grenoble*.
- [4] M. Yazid, “Effet des additifs organiques sur les propriétés de nanostructures de Co–Mo obtenues par déposition électrochimique,” (2014), Doctorat thesis, *University Ferhat Abbas–Setif 1*.
- [5] A. Meroufel and S. Touzain, “EIS characterisation of new zinc–rich powder coatings,” (2007), *Prog. Org. Coatings*, vol. 59, N°. 3, pp. 197–205,
- [6] L. A. Azpeitia, C. A. Gervasi, and A. E. Bolzán, “Electrochemical aspects of tin electrodeposition on copper in acid solutions,” (2019), *Electrochim. Acta*, vol. 298, pp. 400–412,
- [7] S. Manov, A. M. Lamazouère, and L. Ariès, “Electrochemical study of the corrosion behaviour of zinc treated with a new organic chelating inhibitor,” (2000), *Corros. Sci.*, vol. 42, N°. 7, pp. 1235–1248,
- [8] D. E. Hamza, “Electrodéposition et électropolymérisation de monocouches organiques conductrices,” (2018), pp. 21–122. Doctorate thesis, *University Ferhat Abbas–Setif 1*.
- [9] K. Inaba, S. Kobayashi, K. Uehara, A. Okada, S. L. Reddy, and T. Endo, “High Resolution X–Ray Diffraction Analyses,” (2013), *Adv. Mater. Phys. Chem.*, vol. 03, N°. 01, pp. 72–89.

## ***Chapter III***

# *Electrochemical Study and Chemical composition of Ni–Mn, and Zn–Ni–Mn coatings*

---

*This chapter presents the results of CV and CA experiments performed using various bath solutions. To ensure a thorough and precise investigation, we will go over the results of electrodeposition behavior of Ni, Zn, Mn, Zn–Ni, and Zn–Mn, along with to Zn–Ni–Mn, and Ni–Mn CV results. Afterward, we will present the chronoamperometric curves and discuss the effects of different  $[Mn^{2+}]$  concentrations and applied deposition potential using Scharifker and Hills' (S–H) nucleation model. Subsequently, the ensuing section will focus on analyzing the chemical composition of the deposits obtained with varying  $[Mn^{2+}]$  concentrations through energy–dispersive X–ray spectroscopy (EDX).*

---

### III.1. Electrochemical study

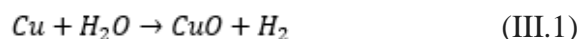
The optimization of electrochemical process parameters is a critical step for the synthesis of Ni–Mn and Zn–Ni–Mn coatings with desired properties. The study of a solution containing several electroactive species (Zn, Ni, and Mn) is very complex, leading to the occurrence of numerous electrochemical reactions. Therefore, an exhaustive investigation is initially carried out to analyze each component (Zn, Ni, and Mn) of the solution individually.

The samples prepared with different  $[\text{Mn}^{2+}]$  values in the binary Ni–Mn and ternary Zn–Ni–Mn systems are labeled as (B<sub>1</sub>, B<sub>2</sub>, B<sub>3</sub>, and B<sub>4</sub>) and (T<sub>1</sub>, T<sub>2</sub>, T<sub>3</sub>, and T<sub>4</sub>), respectively.

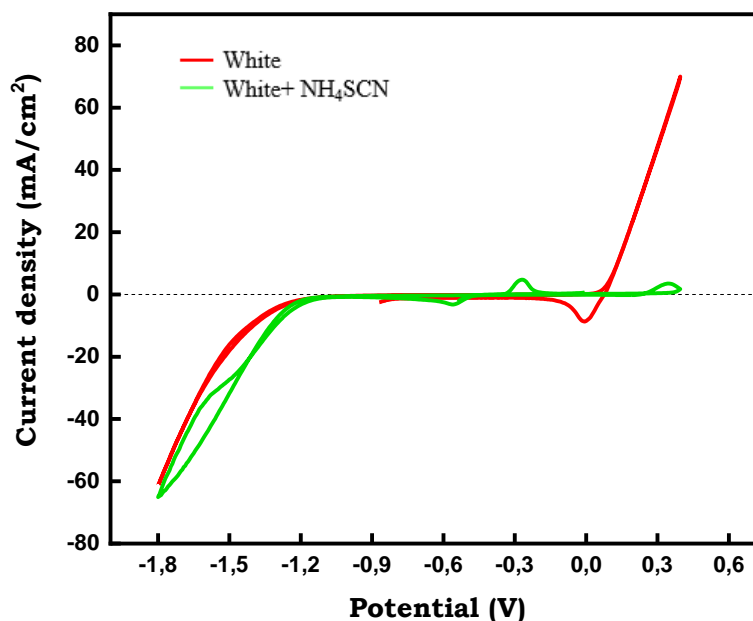
#### III.1.1 CV study

The obtained voltammograms enable the determination of the potential range for the reduction reaction of various redox species. To conduct a comprehensive and precise investigation, we examined the Cu substrate's electrochemical activity and identified its stability zone. The study also sought to evaluate the effect of ammonium thiocyanate (NH<sub>4</sub>SCN) within the Ni<sup>2+</sup> electrolyte. The use of ammonium thiocyanate is intended to enhance the reduction of Ni<sup>2+</sup> and Mn<sup>2+</sup> ions, it is noteworthy that ammonium thiocyanate has significant effects on the Ni and Mn deposits, while it has no impact on the deposition of Zn [1–3].

Figure III.1 shows the voltammograms of Cu substrate immersed in a solution containing the supporting electrolyte (0.3M Na<sub>2</sub>SO<sub>4</sub>, 0.2M H<sub>3</sub>BO<sub>3</sub>) both with and without NH<sub>4</sub>SCN at pH= 3.5 ± 1. The plot spans a potential between 0.3 and –1.8 (vs. Ag/AgCl). It is noted that for the solution without NH<sub>4</sub>SCN the substrate is stable in the potential range (0.3, –1.8V), with no observable reactions on the surface of the electrode except for the reduction of Cu<sup>2+</sup> ions into Cu<sub>2</sub>O (equation III.1) and the reduction of hydrogen which is inevitable in aqueous solutions starting from –1.2 V (vs. Ag/AgCl). Nevertheless, by the introduction of NH<sub>4</sub>SCN in the solution, no reactions occurred other than hydrogen evolution (equation III.3) demonstrating that there is no activity on the substrate's surface [3]. The absence of an anodic current is likely due to NH<sub>4</sub>SCN's capacity to avoid the oxygen reaction.





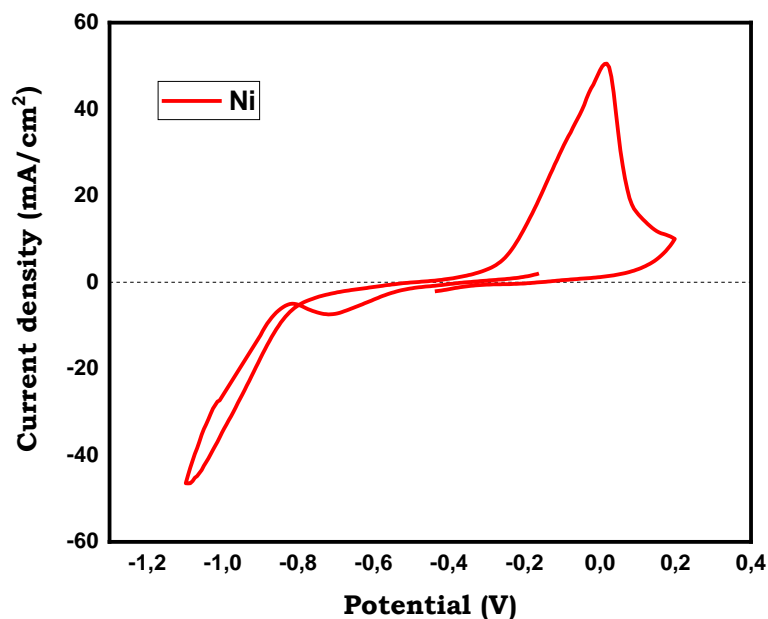


**Figure III. 1:** Cyclic voltammograms of a copper electrode immersed in an electrolyte containing 0.2M Na<sub>2</sub>SO<sub>4</sub> and 0.5M H<sub>3</sub>BO<sub>3</sub> at 10 mV/s with and without NH<sub>4</sub>SCN.

#### III.1.1.1. CV study of Ni

Ni Voltammogram was recorded to obtain general information about the Ni electrodeposition process on Cu substrate. Figure. III. 2 displays the voltammogram of a Cu electrode immersed in a bath with Ni<sup>2+</sup> ions at 10 mVs<sup>-1</sup>. As the potential increases in the scan's negative direction, and at -0.71 V (vs. Ag/AgCl), a cathodic peak is evident, indicating the reduction of Ni<sup>2+</sup> ions. In addition, a distinct crossover loop observed around -0.79 V (vs. Ag/AgCl), can be attributed to the nucleation process. Afterward, there is a noticeable increase in the cathodic current density, related to the hydrogen reaction, around -1.2 V. Subsequently, during the positive direction scan, an intense anodic peak is observed at 0.015 V (vs. Ag/AgCl), assigned to the dissolution of the Ni film previously deposited during the cathodic scan.



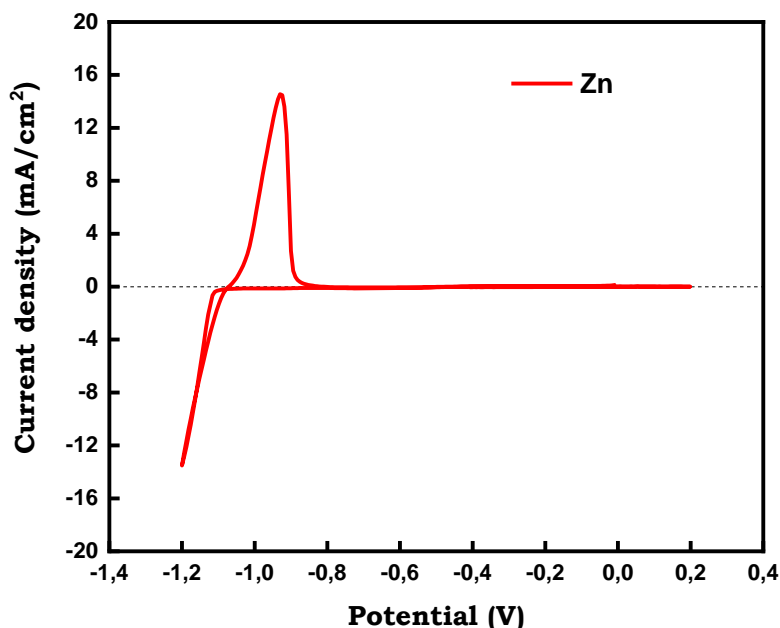


**Figure III. 2.** Cyclic voltammogram of a Cu electrode immersed in Ni<sup>2+</sup> ions bath.

### III.1.1.2. CV study of Zn

The cyclic voltammogram corresponding to the solution containing Zn<sup>2+</sup> ions (Figure III.3) illustrates a sharp increase in cathodic current density around -1.2 V (vs. Ag/AgCl), attributed to parasitic hydrogen evolution. the parasitic hydrogen reaction coincides with Zn reduction, resulting in a notable increase in the cathodic current density [4]. Also, there is a noticeable nucleation loop observed around -1.07 V (vs. Ag/AgCl), indicating phase formation. During the positive anodic scan, an anodic peak appears around -0.93 V (vs. Ag/AgCl), due to the oxidizing of the Zn film.



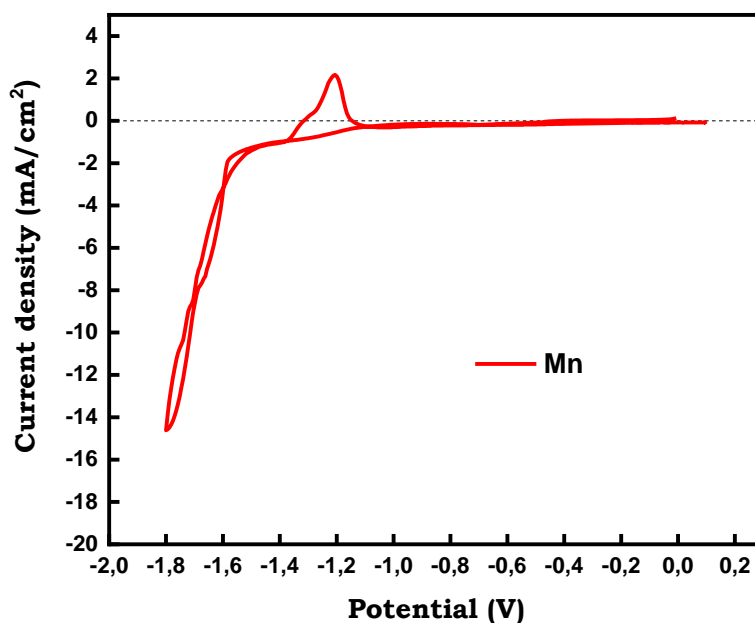


**Figure III.3.** Cyclic voltammogram of a Cu electrode immersed in  $Zn^{2+}$  ions bath.

### III.1.1.3. CV study of Mn

The typical voltammogram, measured on the copper substrate immersed in the  $Mn^{2+}$  solution, is presented in Figure III.4. During the negative direction scan, the cathodic current density exhibits a slight increase around  $-1.26$  V (Ag/AgCl) suggesting the start of the Mn deposit. Moreover, the current density decreases further and extends a maximum at a potential value of about  $-1.8$  V (Ag/AgCl), due to the accompanying hydrogen reaction. [5]. It is noteworthy to mention that hydrogen evolution in liquid solutions occurs simultaneously with Mn deposition [7,8]. Which supports the rising the discharge capacity of  $Mn^{2+}$  ions and promoting the creation of Mn–ammonia complexes, which serve to avoid the development of manganese hydroxides and oxides. [8]. During positive potential sweeps, a crossover potential is detected at  $-1.60$  V (vs. Ag/AgCl), related to the nucleation process as well as the enveloped of supporting material's surface. An anodic peak, initiating at  $-1.2$  V (vs. Ag/AgCl), is attributed to the dissolution of the Mn deposit.

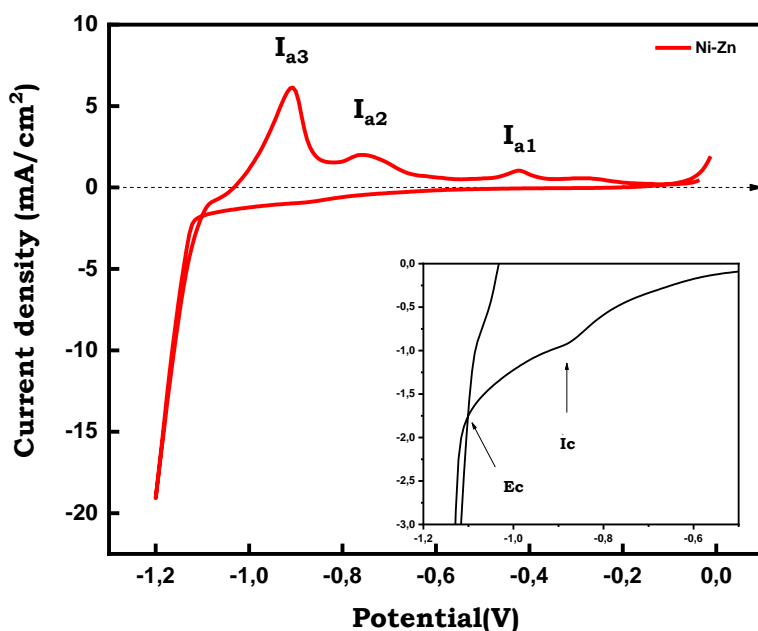




**Figure III. 4.** Cyclic voltammogram of Cu electrode immersed in  $\text{Mn}^{2+}$  ions bath.

#### III.1.1.4. CV study of Ni–Zn

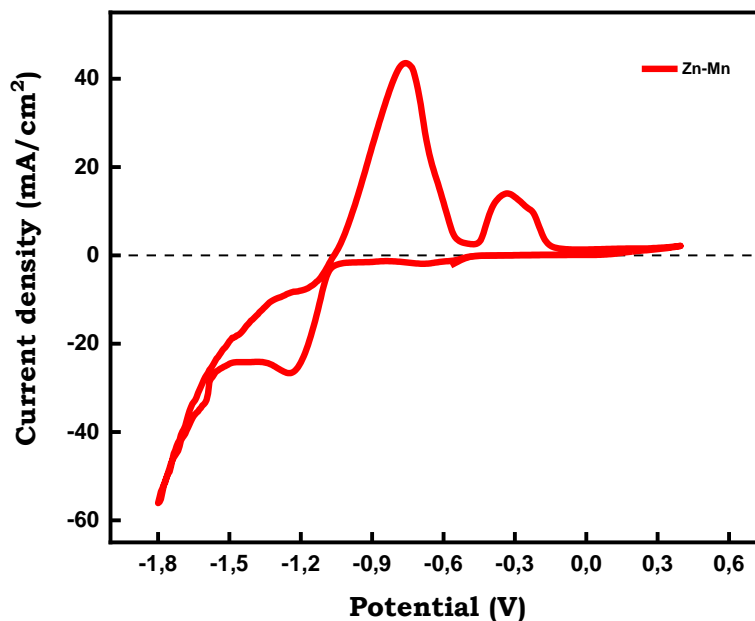
The CV voltammogram, acquired from the electrolyte bath with both  $\text{Ni}^{2+}$  and  $\text{Zn}^{2+}$  ions, is shown in Figure III .5. In cathodic scan, a slight rise in current density is noted at around  $-0.6$  V (vs. Ag/AgCl) due to the reduction of  $\text{Ni}^{2+}$  ions. Subsequently, the cathodic current sharply increases from  $-1.2$  V (vs. Ag/AgCl) because of simultaneous hydrogen reaction and  $\text{Zn}^{2+}$  ions reduction, The positive–direction scan exhibits a crossover loop, indicating a nucleation step. In the anodic part of the voltammogram, three anodic peaks are detected at approximately  $-0.42$ ,  $-0.75$ , and  $-0.9$  V(vs. Ag/AgCl), attributed to the dissolution of different intermediate phases already formed during the direct scan [10,11]. A dissolution peak at  $-0.42$  V, signifying the dissolution of Ni. Concurrently, peaks at more negative potentials are associated with the dissolution of Zn, present in distinct phases within the Zn–Ni alloy [12, 13].



**Figure III.5.** Cyclic voltammograms of a Cu electrode immersed in bath of ( $\text{Ni}^{2+}$ ,  $\text{Zn}^{2+}$ ) ions.

#### III.1.1.5. CV study of Zn–Mn

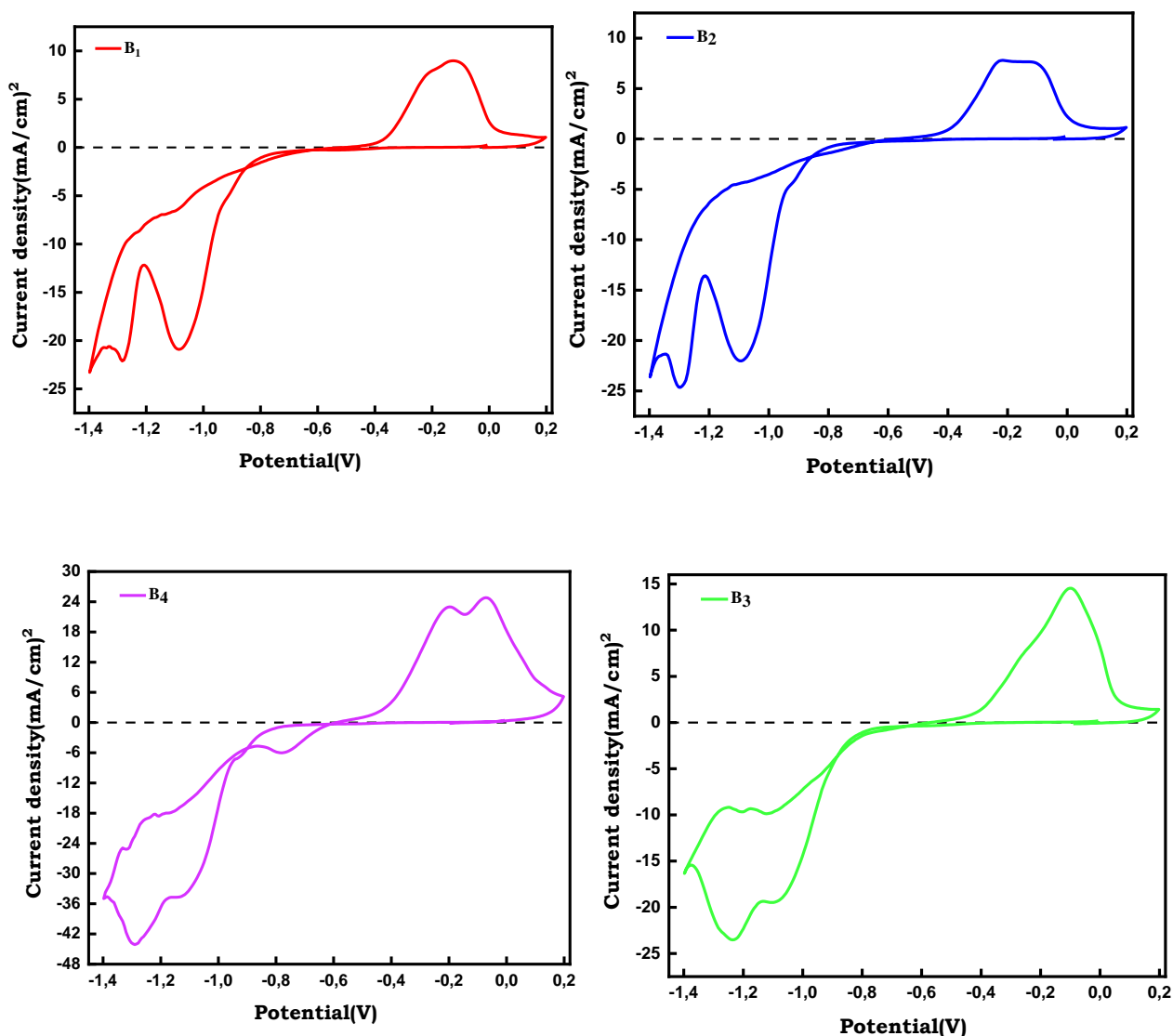
Figure III.6 displays a cyclic voltammogram obtained from an electrolyte bath containing both  $\text{Zn}^{2+}$  and  $\text{Mn}^{2+}$  ions. The scan of negative part, the reduction of  $\text{Zn}^{2+}$  and  $\text{Mn}^{2+}$  ions can be detected around  $-1.24$  and  $-1.61$  V (vs. Ag/AgCl), respectively. It is also observed that the current density increases at more negative potentials, due to hydrogen evolution. During the positive direction scan, two anodic peaks are observed around  $-0.76$  and  $-0.32$  V (vs. Ag/AgCl), corresponding to the metals' dissolution from different previously deposited phases. These results suggested that the Mn atoms were incorporated into the Zn deposit, forming multiple phases [16].



**Figure III.6.** Cyclic voltammograms of a Cu electrode immersed in a bath of ( $\text{Zn}^{2+}$  and  $\text{Mn}^{2+}$ ) ions.

#### III.1.1.6. CV study of Ni–Mn

The cyclic voltammograms of Cu substrate in different aqueous electrolyte solutions containing  $\text{Ni}^{2+}$  and different  $[\text{Mn}^{2+}]$  are illustrated in Figure III.7. In the negative scan,  $\text{Ni}^{2+}$  and  $\text{Mn}^{2+}$  ions reduction is evidenced by the presence of two cathodic peaks, around  $-1.08$  V (vs. Ag/AgCl) and  $-1.28$  V (vs. Ag/AgCl) observed on different voltammograms. The increase of  $[\text{Mn}^{2+}]$  in the bath is accompanied by a slight shift of the cathodic peaks towards the more negative potential values. This confirmed the incorporation of Mn and Ni atoms and the creation of Ni–Mn coatings. During the co-deposition of Ni and Mn atoms, the presence of  $\text{Mn}^{2+}$  ions in the bath influences the Ni nucleation mechanism. The Mn atoms are transported and loosely adsorbed on the cathode surface leading to an increase of the active sites on the interface of the electrode that provide more nucleation sites for the reduction of  $\text{Ni}^{2+}$  ions. The reaction of hydrogen evolution is always associated with the formation of Ni–Mn alloys. On the reverse scan, two noted peaks are observed on the voltammograms that may be linked to the oxidation of the previously deposited phases. The position of the anodic peaks is slightly dependent on the  $[\text{Mn}^{2+}]$  in the bath.

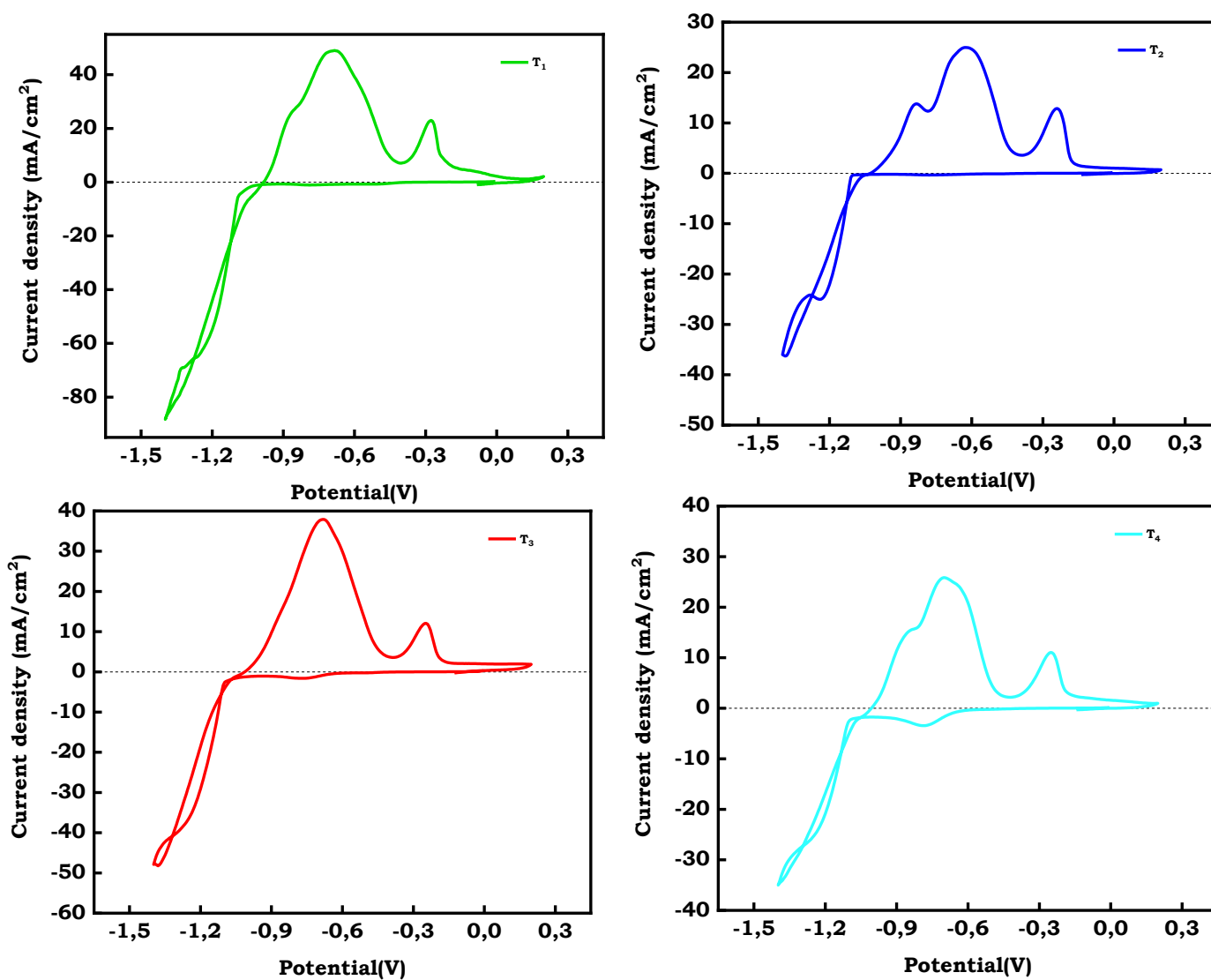


**Figure III. 7.** Cyclic voltammograms of Cu electrode in different baths with different  $[Mn^{2+}]$  (0.05, 0.1, 0.2, 0.4)

### III.1.1.7. CV study of Zn–Ni–Mn

The obtained voltammograms, from the electrolyte bath containing  $Zn^{2+}$ ,  $Ni^{2+}$  and  $Mn^{2+}$  ions with different  $[Mn^{2+}]$  are displayed in Figure III.8. The form of the voltammograms differs from those of pure (Ni, Mn, Zn) elements. This is an outcome of the existence of diverse species in the bath and the production of several phases. During the cathodic scan, two cathodic peaks emerge at approximately  $-0.77$  V (vs. Ag/AgCl) and  $-1.1$  V (vs. Ag/AgCl) corresponding to the reduction of  $Ni^{2+}$  and  $Zn^{2+}$  ions, respectively. The reduction of  $Mn^{2+}$  ions remain unnoticed due to the simultaneous occurrence of the hydrogen reaction. Subsequently, two crossover

potentials are observed, indicating the nucleation of distinct phases. In the positive scan, three anodic peaks are detected, signifying the dissolution of various phase structures. The anodic peak positions deviate from those noted for Zn, Ni, and Mn elements due to difference between the phases produced by distinct bath compositions.



**Figure III.8.** Cyclic voltammograms of Cu electrode immersed in different baths containing both Ni<sup>2+</sup>, Zn<sup>2+</sup> and Mn<sup>2+</sup> ions with different [Mn<sup>2+</sup>] (0.05, 0.1, 0.2, 0.4).



### III.1.2. CA study

Chronoamperometry (CA), is a suitable method for investigating the electro-crystallization kinetics and the early stages of the nucleation and growth mechanisms of electrodeposition. Scharifker–Hills (S–H) proposed a theoretical model to describe the nucleation process (instantaneous and progressive) [18]. This part focused on the study of the effect of different  $[\text{Mn}^{2+}]$  on the nucleation and growth mechanisms of Ni–Mn and Zn–Ni–Mn deposition coatings. The analysis of the nucleation process for Ni–Mn and Zn–Ni–Mn coatings on the Cu electrode involved the examination of transient current–time curves ( $I = f(t)$ ). These curves were recorded at various applied potentials ( $-1.11$ ,  $-1.12$ , and  $-1.13$  V (Ag/AgCl) and ( $-0.8$ ,  $-0.9$ , and  $-1$  V Ag/AgCl) for Ni–Mn and Zn–Ni–M coatings, respectively. The deposition time for this analysis was set at 1800 seconds. The concentrations of  $\text{Ni}^{2+}$  and  $\text{Zn}^{2+}$  were kept constant at (0.2 M) while  $[\text{Mn}^{2+}]$  varied in the range (0.05, 0.1, 0.2, 0.3 M) for Ni–Mn, and (0.05, 0.1, 0.2, 0.4) M for Zn–Ni–Mn coatings respectively.

#### III.1.2.1. CA study of Ni

After determining the reduction potentials by analyzing the cyclic voltammograms of Ni, the potentiostatic current–time curve obtained at  $-0.8$  V (vs. Ag/AgCl) during the electrodeposition of a Ni coating on the copper substrate is shown in Figure III.9. It is noted that the current density increases quickly in the first few seconds (around 15 s) of deposition, followed by a decrease for further deposition time. The rise in current density is attributed to the beginning of the electrodeposition process, whereas the subsequent decrease is a result of the diffusion process [19]. Subsequently, a steady state characterized by a constant current density was established, extending from the end of the deposition process. According to a comparison between the theoretical and experimental curves (Figure. III. 10), the mechanism under analysis goes through a progressive nucleation process.

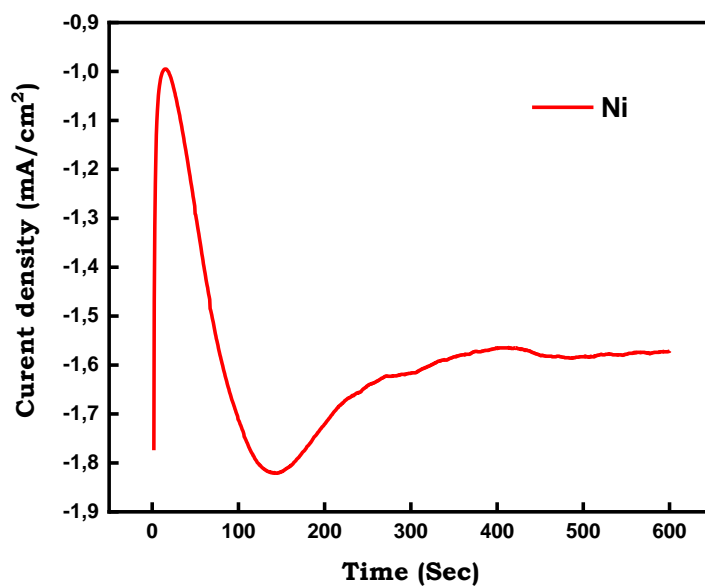


Figure. III.9. Transient current density plot of Ni on Cu electrode obtained at  $-0,8\text{V}$  (vs. Ag/AgCl)).

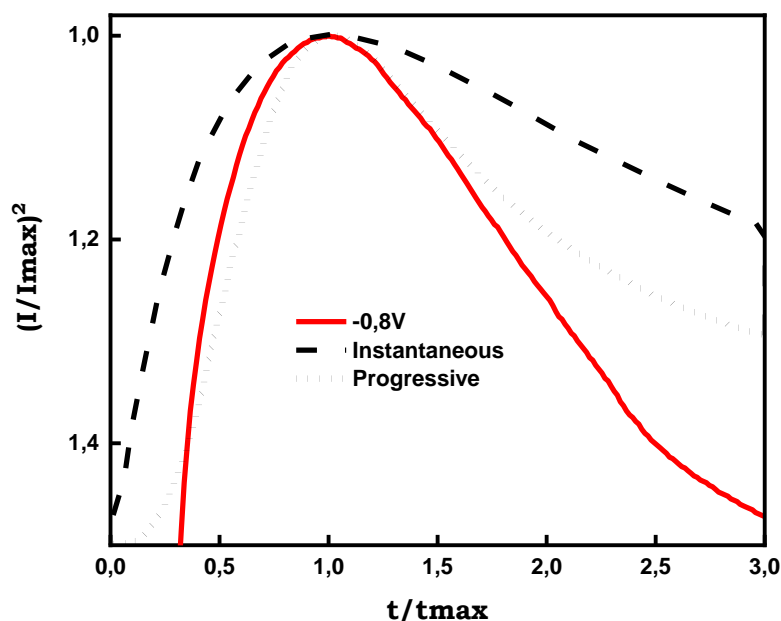
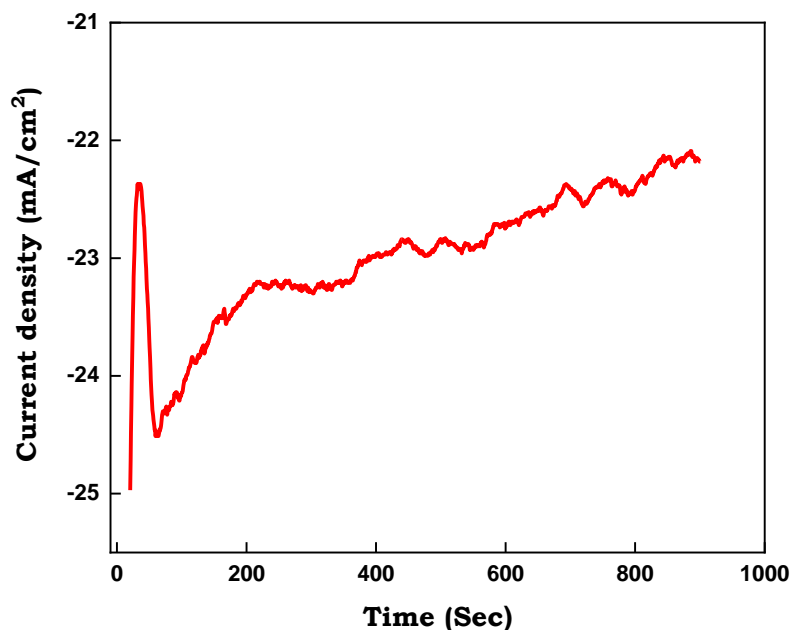


Figure III. 10. Nondimensional plot of experimental transients of Ni in comparison with instantaneous and progressive curves.

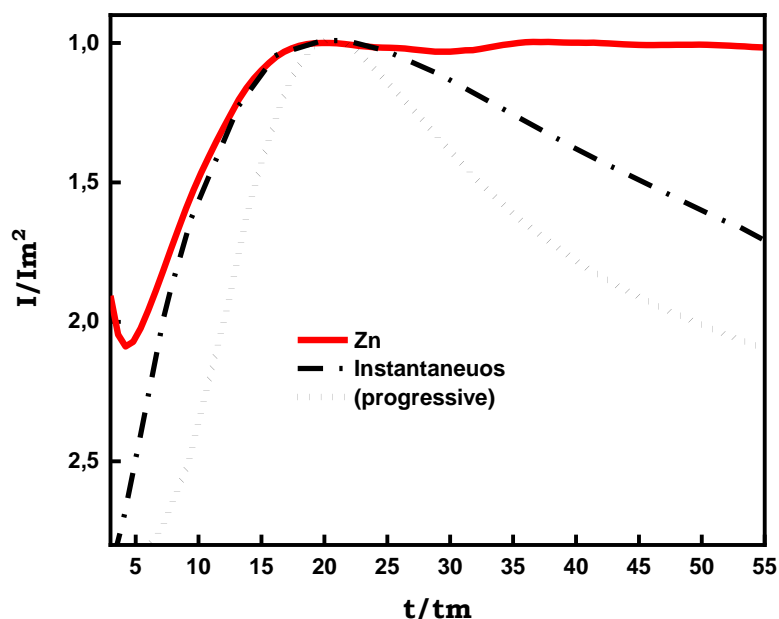
### III. 1.2. 2. CA study of Zn

Figure III.11 displays the current–time curves for Zn electrodeposition on a Cu substrate at  $-1,11\text{ V}$  (vs. Ag/AgCl). In general, the characteristic shape of this curve represents a typical response of transient current in an electrochemical nucleation–growth process under diffusion

control where the hemispherical diffusion zones surrounding each site facilitate the passage of electroactive molecules to the active sites. The radius of these zones expands over time, due to the expansion of the nuclei. Eventually, the curves exhibit oscillations due to the pronounced hydrogen evolution in the Zn bath. Figure III.12 displays the experimental transient curve, aligned with theoretical curves representing both instantaneous and progressive nucleation modes. It is noted that the experimental curve follows the instantaneous 3D mode during the electro crystallization process. When reaction time exceed the maximum time limit ( $t > t_{\max}$ ), the experimental curve moved away from the model. The slight difference between the theoretical and experimental plots can be attributed to the fact that theoretical models are based on nuclei with hemispherical geometry as well as the complexities involved by the hydrogen reduction reaction.



**Figure.III.11.** Transient current density plot of Zn on Cu electrode obtained at  $-1.1\text{V}$  (vs. Ag/AgCl)).



**Figure III. 12.** Dimensionless plot of experimental  $(I/I_{max})^2$  vs.  $(t/t_{max})$  of Zn and the theoretical curves (instantaneous and progressive modes).

### III.1.2.3. CA of Mn

The current–time curve for Mn electrodeposition at  $-1.6$  V (Ag/AgCl) on a Cu substrate is shown in Figure III.13. The chronoamperometric curve initiates with a rapid rise in current density, signifying the emergence of nucleation sites. As the number of these sites increases, the current density progressively increases reaching its peak at the maximum current ( $I_{max}$ ) along with the corresponding time ( $t_{max}$ ). After that, the current density progressively diminishes over time, converging toward a pseudo–stationary state. This state aligns with the linear diffusion process, representing the controlled diffusion–driven growth of germs established on the substrate during the initial phase. By comparing experimental data with theoretical current transients in a non–dimensional form,  $(I/I_{max})^2$  against  $(t/t_{max})$  is plotted. As depicted in Figure III.14, the Mn electrodeposition mechanism follows an instantaneous three–dimensional process initially. However, as it progresses to later stages ( $t/t_{max} > 1$ ), the experimental curve begins to deviate from the theoretical models. The Mn electrodeposition mechanism adheres to an instantaneous three–dimensional process. This can be explained by the presence of additional electrochemical processes (hydrogen reduction reaction).

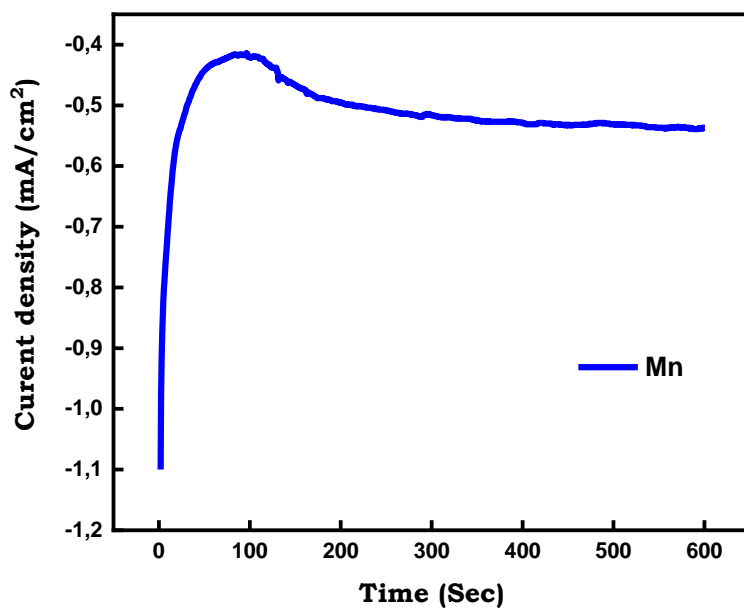


Figure III.13 Chronoamperometry curve of Mn deposited at 1.6 V (vs. Ag/AgCl) in the sulfate bath.

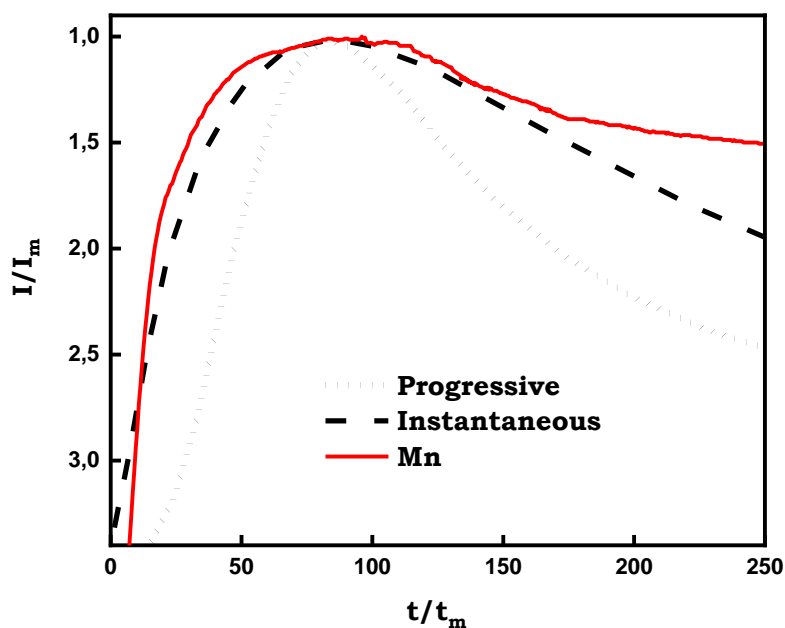


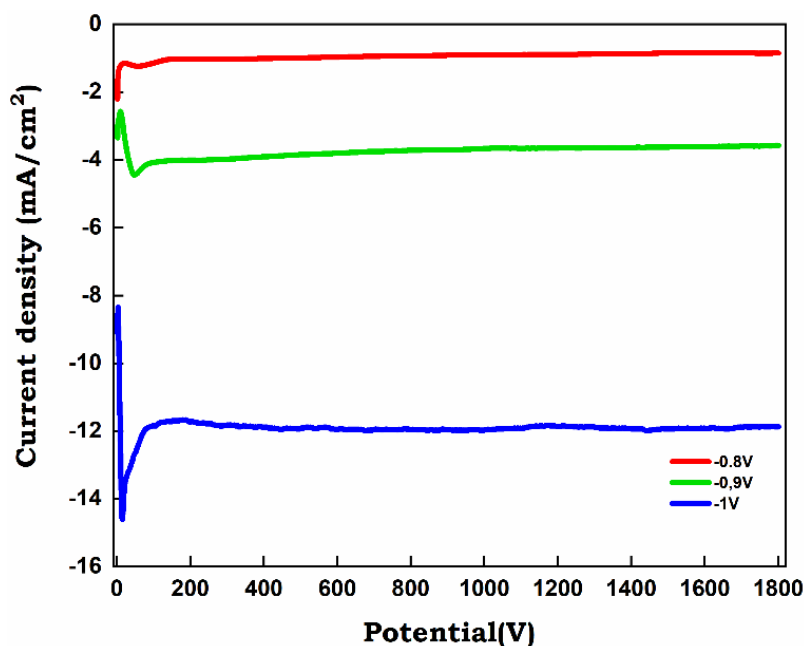
Figure III.14. Dimensionless plot  $(I/I_{max})^2$  vs.  $(t/t_{max})$  of Mn obtained in comparison with theoretical curves for instantaneous and progressive modes.

### III. 1. 2. 4 Effect of the applied potential on the nucleation process

The applied potential plays an important role in nucleation and growth mechanisms. In this sense, lower potentials may cause a weak development leading to a uniform and more controllable coatings thickness. Conversely, higher potential values increase nucleation leading to faster growth and thicker coatings [20–23]. The applied potential also influences the crystalline structure, adhesion, and microstructure of the coatings, providing control over properties like improved adhesion and desired microstructural characteristics [24].

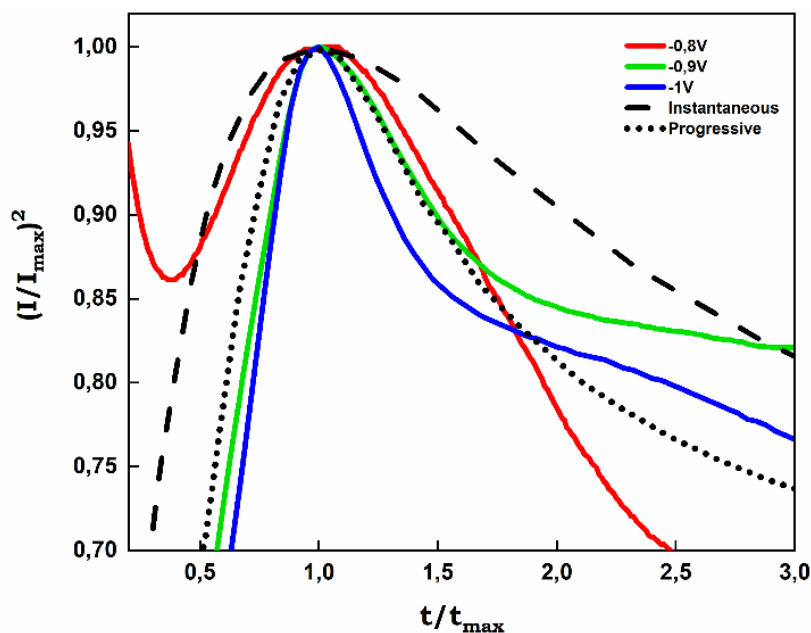
#### III.1.2. 4 .1. Effect of the applied potential on Ni–Mn nucleation

The CA experiments for Ni–Mn coatings were conducted at three distinct potential values ( $-0.8$ ,  $-0.9$ , and  $-1$  V Ag/AgCl). As illustrated in figure III. 15, all curves demonstrate three distinct regions corresponding to the nucleation and growth processes. In the initial stage (first region), the current density shows a rapid decrease over a short period, primarily attributable to electric double-layer charging on the surface of the substrate. Subsequently (in the second region), the current density rises to a maximum value ( $I_{\max}$ ) reflecting the typical nucleation and growth of the number of nuclei. [23]. Finally, in the third region, the current density gradually diminishes, approaching a steady state, signifying the limitation of mass transfer of ions to the electrode interface. Furthermore, the obtained current–time transients show that the cathodic current density shifted to more negative values for a potential of  $-1$  V vs.Ag/AgCl. In addition, the current density values are largely different for the curves obtained at deposition potentials of ( $-0.8$ ,  $-0.9$  V vs.Ag/AgCl) compared to that obtained at ( $-1$  V vs.Ag/AgCl). This indicates a rise in the nucleation rate corresponding to an increase in the number of nucleation sites on the substrate interface. It can be also observed that the maximum current density,  $I_{\max}$ , increases and the corresponding  $t_{\max}$  decreases by applying more negative potential. The increase of the maximum peak current density is an outcome of the rise of the number of sites and the nucleation rate at higher overpotential leading to the larger electroactive area. The decrease in  $t_{\max}$  at high applied potential is due to the lower activation energy against nucleation which accelerates the process of nucleation at shorter time.



**Figure III. 15.** Transient current density plots of Ni–Mn on Cu electrode obtained at various applied potentials ( $-0.8\text{V}$ ,  $-0.9\text{V}$ ,  $-1\text{V}$  (vs. Ag/AgCl))

The CA curves were analyzed using the most commonly used theory proposed by S–H [18]. For this purpose, the data extracted from the chronoamperometry curves were converted into non-dimensional forms, represented as  $(I/I_{\text{max}})^2$  against  $(t/t_{\text{max}})$  and subsequently compared to theoretical instantaneous and progressive nucleation plots as shown in figure III.16. When the applied potential value was fixed at  $-0.8\text{ V}$  vs. Ag/AgCl, the experimental data followed the instantaneous mode before  $t_{\text{max}}$ , then tended to the progressive one for  $t > t_{\text{max}}$ . The transition from the instantaneous to progressive mode could be related to the saturation of active sites, which cannot be refilled at the same time. When more negative potential values ( $-0.9\text{ V}$  vs. Ag/AgCl and  $-1\text{ V}$  vs. Ag/AgCl) are applied, the experimental data are fitted by the 3D progressive nucleation mechanism.



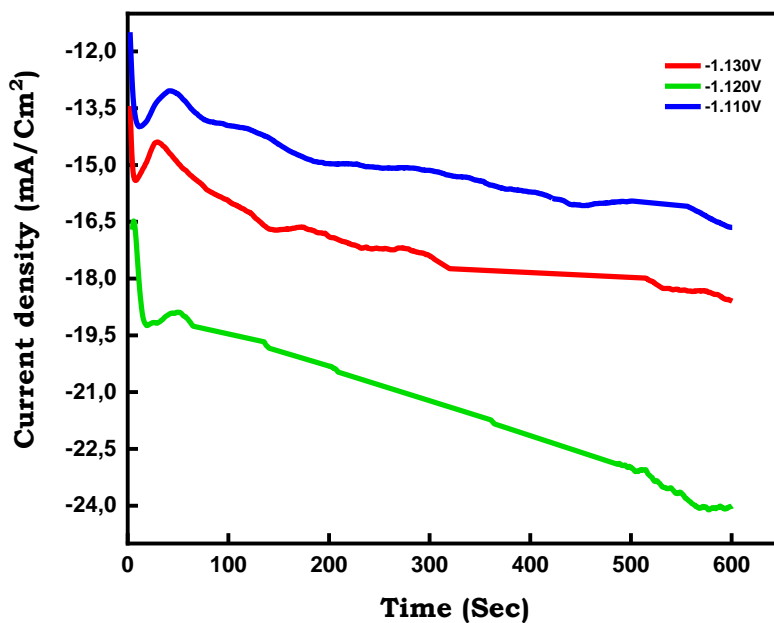
**Figure III. 16** Dimensionless plot  $(I/I_{max})^2$  vs.  $(t/t_{max})$  of Ni–Mn coatings deposited at different potentials ( $-0.8V$ ,  $-0.9V$ , and  $-1V$  vs. Ag/AgCl) and theoretical curves (instantaneous and progressive modes).

### III.1.2.4. 2. Effect of the applied potential on Zn–Ni–Mn

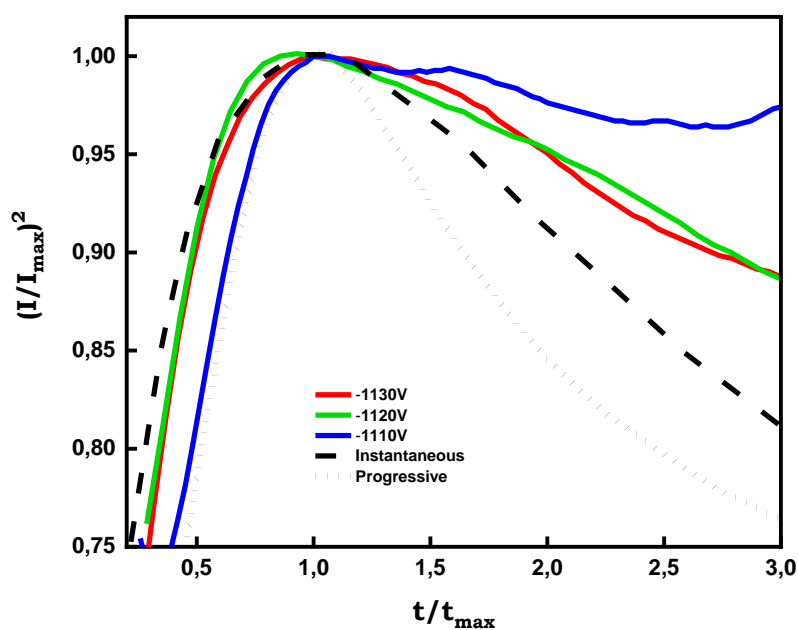
Figure III.17 shows the early stages of Zn–Ni–Mn coatings electrodeposition at various applied potentials ( $-1.11$ ,  $-1.12$ , and  $-1.13$  V vs. Ag/AgCl). The current density–time curve, recorded at the highest applied potential value ( $-1.11$  V vs. Ag/AgCl), shows the highest value of  $I_{max}$  in comparison to other current density–time curves. The rise in maximum current density is attributed to the increase in nucleation rate indicating an increase in the available active sites on the surface [25].

According to the S–H model [18], the current–time transients (figure III .18) acquired at  $-1.11$  V vs. Ag/AgCl indicate that electro–crystallization closely follows the progressive mechanism mode during shorter times ( $t < t_{max}$ ). However, with more negative potential values of  $-1.12$  V vs. Ag/AgCl and  $-1.13$  V vs. Ag/AgCl, the curves follow the instantaneous nucleation process. Lower applied potentials result in a low rate of nucleation, which progresses gradually through the progressive nucleation mode [26]. Beyond  $t > t_{max}$ , the curves are expected to significantly up on the theoretical models. The deviation of experimental plots from the S–H model can be attributed to the deviation of the nuclei from the hemispherical shape since the model were developed for hemispherical nuclei [27].





**Figure III. 17.** Transient current density plots of Zn–Ni–Mn coatings obtained at various applied potentials (–1.11 V, –1.12 V, 1.13 V (vs. Ag/AgCl))

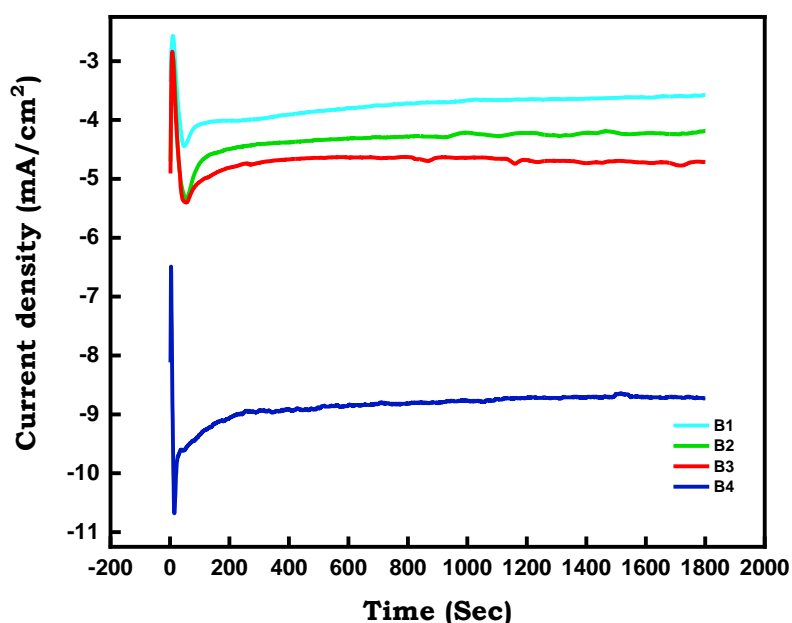


**Figure III.18.** Nondimensional plots of experimental transients of Zn–Ni–Mn coatings acquired at various deposition potentials. (–1.11V, –1.12V, and –1.13V vs. Ag/AgCl) and theoretical curves (instantaneous and progressive modes).

### III.1.2. 5 The influence of $[\text{Mn}^{2+}]$ on the coating's nucleation.

#### III.1.2. 5 .1. The influence of $[\text{Mn}^{2+}]$ on Ni–Mn coatings nucleation

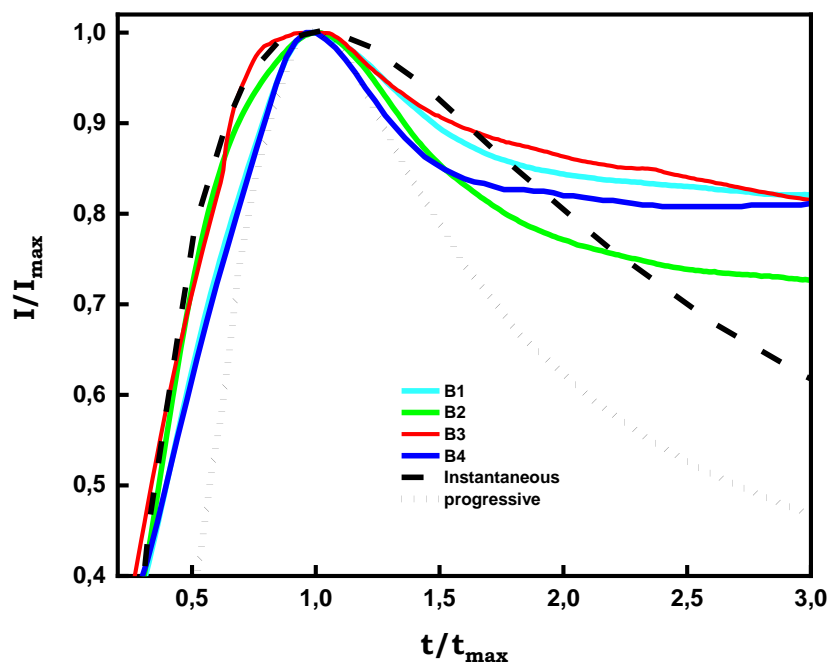
The CA curves of Ni–Mn coatings deposited from baths containing different  $[\text{Mn}^{2+}]$  ions are presented in Figure III.19. It is worth mentioning that with the increase of  $[\text{Mn}^{2+}]$  in the bath, the maximum current density,  $I_{\text{max}}$ , shifted to more negative values and the corresponding time,  $t_{\text{max}}$ , increased, which indicates a rise in the nucleation rate by providing more active sites.



**Figure. III. 19.** Transient current density plots of Ni–Mn coatings obtained at  $-1$  V (vs. Ag/AgCl)) with different  $[\text{Mn}^{2+}]$  (0.05M, 0.1M, 0.2M and 0.3M).

Figure III. 20. clearly demonstrates that in the first region,  $t < t_{\text{max}}$ , the curves of electrolytes with  $[\text{Mn}^{2+}]$  of 0.1 M and 0.2 M indicate an instantaneous nucleation mode while for the other concentration values (0.05 M, and 0.3 M), the curves are at the progressive mode. Beyond  $t_{\text{max}}$ , considering the second part of the curves, the experimental data, for all the concentrations, lie between both the theoretical nucleation modes and then tend gradually towards the instantaneous nucleation mode. These results indicate that the nucleation and subsequent growth of nuclei are described by the hemispherical diffusion model where the progressive nucleation mode is observed at the early stages and is followed by an instantaneous nucleation mode after reaching the maximum current density. The transition from progressive to instantaneous nucleation mode is observed just after the partial or total coverage of the electrode

surface ( $t > t_{\max}$ ). Under these new surface conditions, the competitive reaction of hydrogen is more susceptible and exhibits a direct effect on the mode of nucleation.

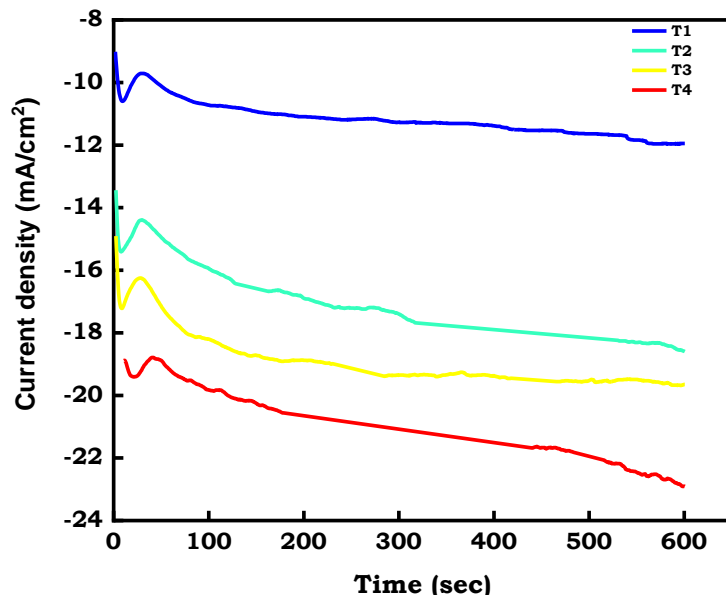


**Figure III.20.** Nondimensional plots of experimental transients of Ni–Mn coatings deposited at  $-1$  (vs. Ag/AgCl) for varying  $[\text{Mn}^{2+}]$  (0.05M, 0.1M, 0.2M and 0.3M) and theoretical curves (instantaneous and progressive mods).

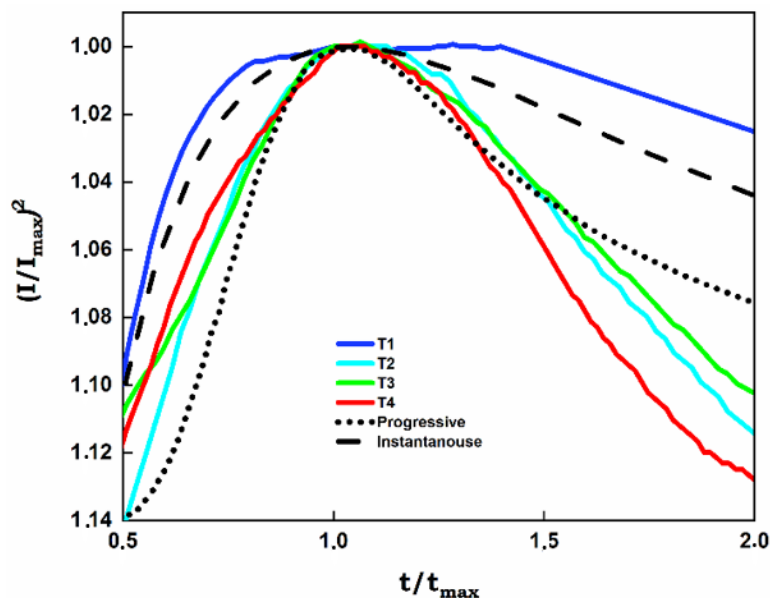
### III.1.2.5. 2. The influence of $[\text{Mn}^{2+}]$ on Zn–Ni–Mn coatings nucleation

Figure III. 21 shows the CA curves of Zn–Ni–Mn coatings deposited from baths with varying  $[\text{Mn}^{2+}]$ . The chronoamperograms display a three–dimensional diffusion–controlled nucleation and growth process behavior. The curves start with a decrease in current density, followed by a peak, and finally a slight decline to a near–constant level. Furthermore, it is observed that for 0.4 M, the current density shifted towards more negative values. This indicates that increasing  $\text{Mn}^{2+}$  ions in the bath could potentially enhance the deposition of Zn–Ni–Mn coatings. The comparison of the dimensionless theoretical plots with the experimental data is depicted in figure III. 22. It's evident that there is a gradual deviation of the experimental curve from the instantaneous theoretical model for the electrolyte containing 0.05 M of  $\text{Mn}^{2+}$  ions, attributed to the hydrogen evolution reaction. As the  $[\text{Mn}^{2+}]$  increases, the experimental curves initially ( $t < t_{\max}$ ) align between the theoretical progressive and instantaneous nucleation modes. Subsequently, they transition towards the progressive mode for  $t > t_{\max}$ , and ultimately deviate

from both theoretical curves. This phenomenon may be ascribed to the existence of structural defects on the surface, which offer additional active nucleation sites for the electro-crystallization of metal ions.



**Figure III. 21.** Transient current density plots of Zn–Ni–Mn coatings obtained at  $-1.12\text{V}$  (vs. Ag/AgCl) for different  $[\text{Mn}^{2+}]$  (0.05M, 0.1M, 0.3M and 0.4M).

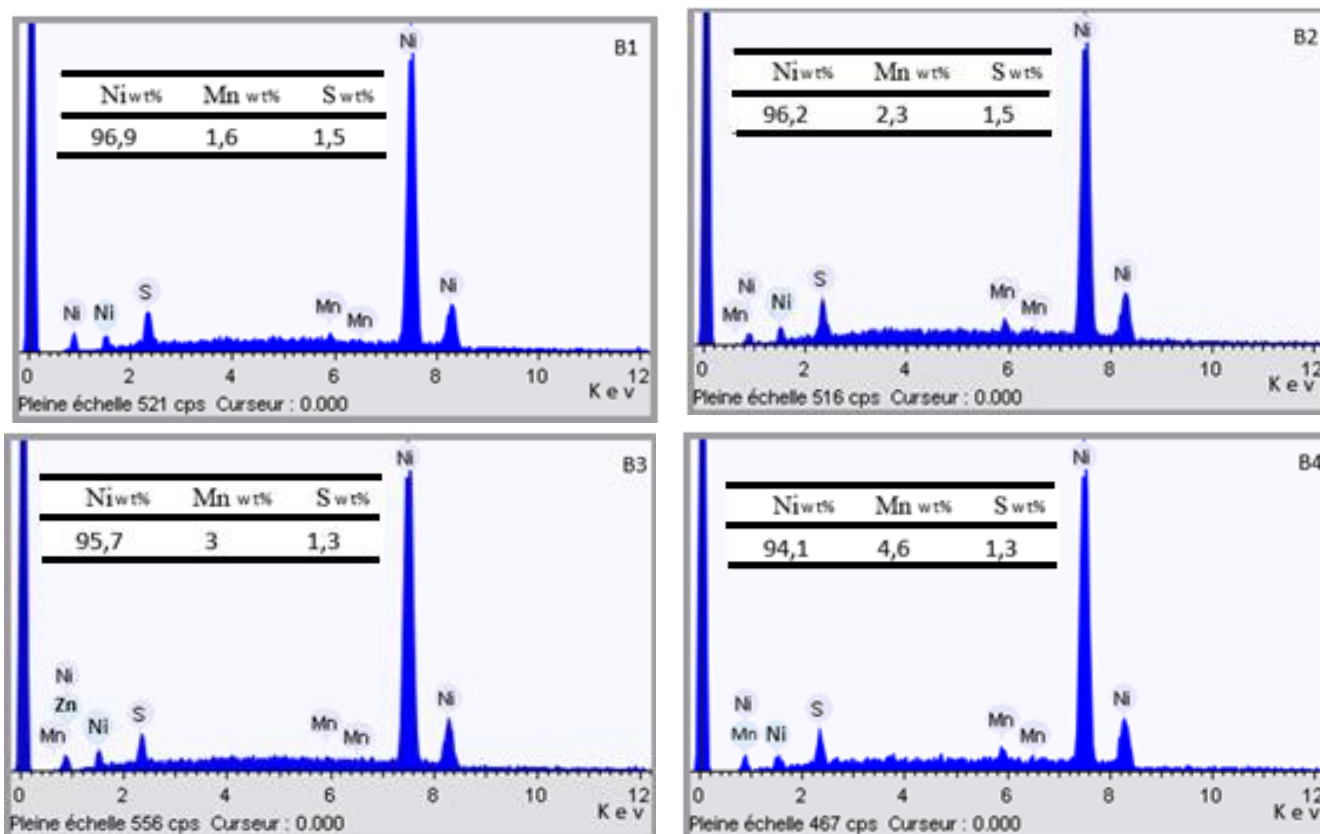


**Figure III. 22:** Nondimensional plots of experimental transients of Zn–Ni–Mn coatings obtained with different  $[\text{Mn}^{2+}]$  (0.05M, 0.1M, 0.3M and 0.4M) in comparison with theoretical curves for instantaneous and progressive modes.

### III.2. Chemical composition analyses

### III.2 .1. Chemical composition of Ni–Mn coatings

Elemental chemical composition of Ni–Mn coatings obtained at different  $[\text{Mn}^{2+}]$  was carried out by (EDX), as shown in Figure III.23. The EDX spectra exhibit distinctive peaks corresponding to Ni and Mn atoms. Additionally, peaks originating from sulfur (S) are detected. Notably, no peaks related to the Cu substrate are observed, suggesting thorough coverage of the substrate surface by the coatings with a significant thickness. Increasing the  $[\text{Mn}^{2+}]$  in the bath results in a rise in Mn content from 1.5 wt.% to 4.6 wt.% in the coatings while the Ni content decreases between 96.9 and 94.1 wt.%. On the other hand, the (S) content remains relatively constant at around 1.5 wt.%. It is noteworthy that there is a significant difference in the Mn and Ni contents. This discrepancy might be explained by the applied potential ( $-1\text{V}$  vs.  $\text{Ag}/\text{AgCl}$ ), which closely resembles Ni's deposition potential. Moreover, the Mn electrodeposition from an aqueous solution presents major obstacles, as it is accompanied by the concurrent hydrogen reduction reaction and features a low deposition potential ( $E_{\text{Mn}^{2+}/\text{Mn}} = -1.18 \text{ VSHE}$ ). The Ni–Mn coatings electrodeposition is considered as an induced process.



**Figure III. 23:** EDX spectra of Ni–Mn coatings electrodeposited at various  $[\text{Mn}^{2+}]$  (0.05M, 0.1M, 0.2M, and 0.3 M) at  $-1\text{V}$  (vs.  $\text{Ag}/\text{AgCl}$ ).

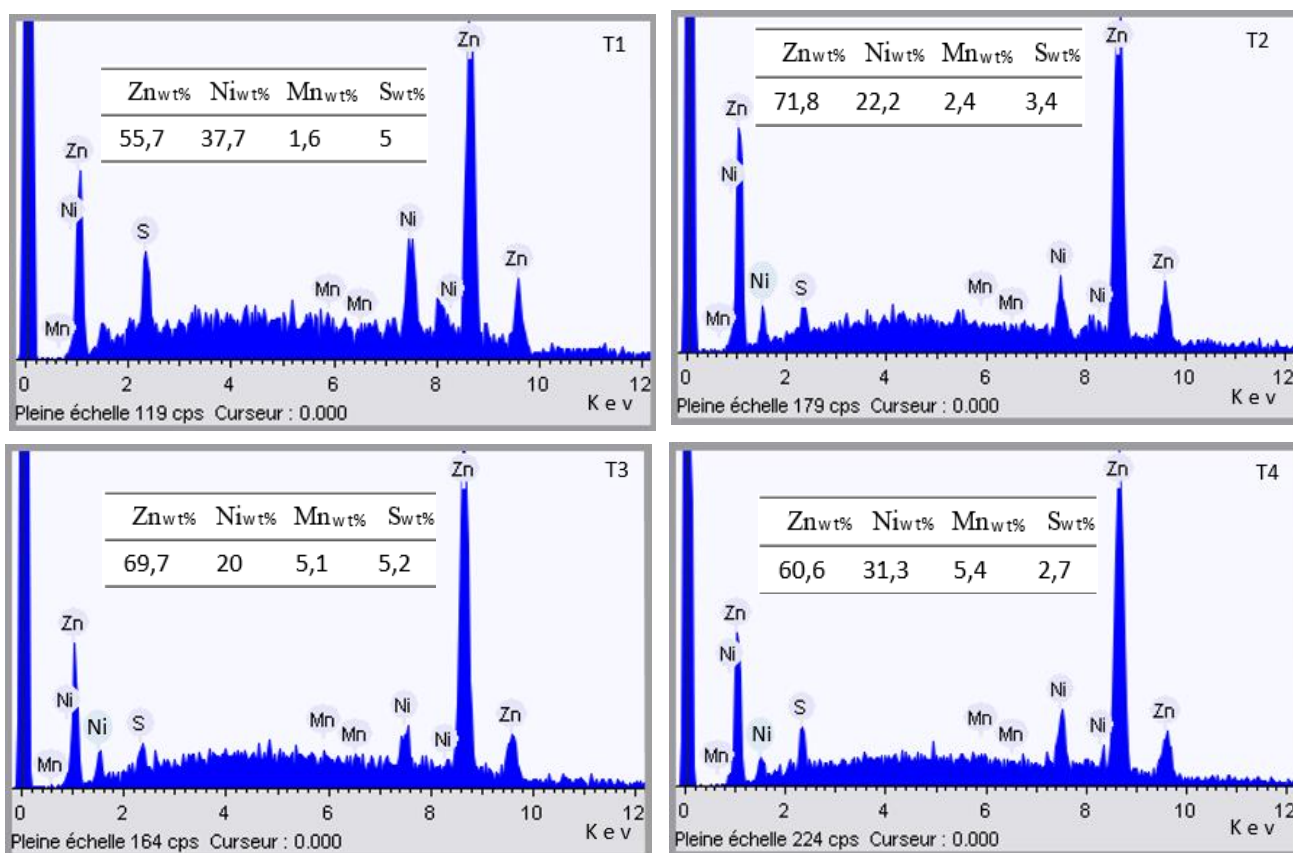
### III.2. 2. Chemical composition of Zn–Ni–Mn coatings

Figure III. 24 displayed the EDX spectra of the Zn–Ni–Mn electrodeposited coatings. One can observe the presence of peaks corresponding to Zn, Ni, and Mn, affirming the reduction of their respective ions and the subsequent deposition of Zn, Ni, and Mn atoms onto the Cu substrate. Furthermore, supplementary peaks of sulfur (S) originating from the electrolyte are also identified. It is also observed that the Zn content exceeds that of Ni and Mn due to the preferential electrochemical deposition of Zn. This phenomenon is identified as anomalous codeposition behavior, which occurs when less noble metal atoms are preferentially deposited from a bath containing various metallic ions. Consequently, the deposit contains a higher content of the less noble metal compared to its concentration in the bath. Typically, the electrodeposition of Zn with Fe group metals (Fe, Co, Ni), under varying deposition conditions, exhibits an anomalous codeposition behavior, wherein Zn is preferentially deposited. [30]. Specifically, Zn–Ni film deposition from chloride or sulfate baths has been identified as anomalous codeposition behavior and reduction mechanism has been suggested to clarify the anomalous codeposition phenomenon [31]. The proposed reduction mechanism unfolds in the following steps: (i) The pH increases near the cathode, driven by intense H<sub>2</sub> evolution, induces the production of zinc hydroxides, Zn (OH)<sub>2</sub>, (ii) Subsequently, the adsorption of Zn (OH)<sub>2</sub> inhibits the reduction of Ni ions, leading to a limitation in the deposition of Ni atoms. Consequently, the preferential deposition of the less noble metal (Zn) prevails, compromising the deposition of the more noble metal, Ni. Nevertheless, an alternative perspective suggests that the anomalous codeposition in Zn–Ni–Mn coatings could be attributed to the elevated overpotential required for Ni deposition on Zn. During the creation of the electric double layer, it's probable that the Zn ions replace Ni ions in the dense part of the double layer. This substitution occurs because Zn ions exhibit higher surface activity compared to Ni ions. As a consequence, the resulting effect is an enrichment of the alloy with Zn [32, 33].

As the [Mn<sup>2+</sup>] increases, the predominant element in the coatings remains Zn, with its content rising from 55.7 wt.% to 69.7 wt.%. Conversely, the Ni content varies between 37.7 wt.% and 20 wt.%, while the Mn content rises from 1.6 wt.% to 5.4 wt.%. Additionally, there is a slight decrease in the S content, which ranges from 5.2 wt.% to 2.7 wt.%.

Previous studies have reported that the increase in Mn content in Zn–Ni–Mn coatings correlates with a decrease in Ni content. Correspondingly, the elemental study of Zn–Ni–Mn films deposited from an alkaline bath demonstrates that with a rise in [Mn<sup>2+</sup>], the Mn content in the

coatings rises from 0.82 wt.% to 9.69 wt.%, while the Ni content decreases from 15.1 wt.% to 9.41 wt.% [31].



**Figure III. 24:** EDX spectra of Zn–Ni–Mn coatings electrodeposited at various  $[\text{Mn}^{2+}]$  (0.05M, 0.1M, 0.3M, and 0.4 M) at  $-1.12\text{V}$  (vs. Ag/AgCl).

### III. 3. Conclusion

This section explores the electrochemical synthesis of Ni–Mn and Zn–Ni–Mn coatings under specific conditions. The results can be summed up as follows:

- ❖ CV curves indicate that Ni, Zn, and Mn deposition occurred at  $-0.77$ ,  $-1.1$ , and  $-1.60$  V (vs. Ag/AgCl), respectively. The anodic peaks, appearing at  $-0.93$  V (vs. Ag/AgCl),  $0.015$  V (vs. Ag/AgCl), and  $-1.12$  V (vs. Ag/AgCl), correspond to their oxidation behaviors. Moreover, variations in behavior are evident during the electrodeposition of binary Zn–Ni, Zn–Mn, and Ni–Mn coatings.
- ❖ The presence of reduction peaks in the Ni–Mn and Zn–Ni–Mn voltammograms has been affirmed, confirming the formation of alloys.

- ❖ The experimental CA curves for Zn, Ni, and Mn coatings displays unique behavior during nucleation. Three distinctive phases can be detected: The current density first drops quickly, followed by a subsequent increase, and eventual stabilization. Additionally, every element
- ❖ Electrodeposition of Ni–Mn coatings involves a complex adsorption mechanism with diffusional processes that depend on the of  $[\text{Mn}^{2+}]$  as well as the potential applied.
- ❖ CA analyses revealed a high sensitivity in the deposition potential of the Zn–Ni–Mn coatings, with a notable influence from the hydrogen reduction reaction. The variation of  $[\text{Mn}^{2+}]$  influenced the nucleation and growth mechanism.
- ❖ The EDX results for Ni–Mn coatings indicate the presence of Mn, Ni, and S atoms in the deposits, with Ni being the predominant element, suggesting an induced co-deposition behavior.
- ❖ For Zn–Ni–Mn coatings, Zn becomes the predominant element indicating an anomalous co-deposition behavior.



### References

- [1] S. Somasundaram, A. M. Pillai, A. Rajendra, and A. K. Sharma, “High emittance black nickel coating on copper substrate for space applications,” (2015), *J. Alloys Compd.*, v. 643, pp. 263–269.
- [2] P. Díaz–Arista and G. Trejo, “Electrodeposition and characterization of manganese coatings obtained from an acidic chloride bath containing ammonium thiocyanate as an additive,” (2006), *Surf. Coatings Technol.*, v. 201, no. 6, pp. 3359–3367.
- [3] F. Claudel, N. Stein, N. Allain, A. Tidu, N. Hajczak, and R. Lallement, “Pulse electrodeposition and characterization of Zn – Mn coatings deposited from additive–free chloride electrolytes,” (2019), *J. Appl. Electrochem.*, v. 49, no. 4, pp. 399–411.
- [4] Hayette Faid. “Etude de l’électrodéposition et de la corrosion des alliages Zn–Ni”, (2018), Doctorate Thesis,” Ferhat Abbas University – Sétif 1 (Algeria).
- [5] A. Toghan, M. M. Abou–Krisha, F. H. Assaf, and F. El–Sheref, “Effect of Deposition Potential on the Mechanism and Corrosion Behavior of Zn–Fe–Co Thin Coatings Electrochemically Deposited on a Steel Substrate,” (2021), *Int. J. Electrochem. Sci.* 16, no. 1, pp. 1–15.
- [6] X. Fan, S. Xi, D. Sun, Z. Liu, J. Du, and C. Tao, “Mn–Se interactions at the cathode interface during the electrolytic– manganese process,” (2012), *Hydrometallurgy*, vol. 127–128, pp. 24–29.
- [7] N. Loukil and M. Feki, “Zn–Mn alloy coatings from acidic chloride bath: Effect of deposition conditions on the Zn–Mn electrodeposition–morphological and structural characterization,” (2017), *Appl. Surf. Sci.* 410, pp. 574–584.
- [8] D. Sylla, J. Creus, C. Savall, O. Roggy, M. Gadouleau, and P. Refait, “Electrodeposition of Zn–Mn alloys on steel from acidic Zn–Mn chloride solutions,” (2003), *Thin Solid Films*, v. 424, no. 2, pp. 171–178.
- [9] Assaf, Fawzi H., Abou–Krisha, Mortaga M., Daoush, Walid M. and Eissa, Ahmed A. "Fabrication of Zn–Ni–Mn alloy by electrodeposition and its characterization", (2018), *Corrosion Reviews*, v. 36, no. 6, pp. 547–5582018.
- [10] F. Elkhatabi, M. Sarret, and C. Müller, “Chemical and phase compositions of zinc + nickel alloys determined by stripping techniques,”, (1996), *J. Electroanal. Chem.*, v. 404, no. 1, pp. 45–53.

- [11] N. Lotfi, M. and all, “Zinc–Nickel Alloy Electrodeposition: Characterization, Properties, Multilayers and Composites “, (2018), v. 54, no. 6.
- [12] J. Zhang, Z. Feng, Q. Li, P. Yang, H. Song, and M. An, “Electrodeposition of nanocrystalline Zn–Ni coatings with single gamma phase from an alkaline bath,” (2015). *Surf. Coatings Technol.*, v. 270, pp. 47–56.
- [13] Y. Arthoba Naik and, S. Basavanna “Study of the effect of new brightener on Zn–Ni alloy electrodeposition from acid sulphate bath,” (2011), *J. Appl. Electrochem.*, v. 41, no. 5, pp. 535–541.
- [14] S. P. Kumaraguru, P. Ganesan, and B. N. Popov, “Development of compositionally modulated multilayer Zn–Ni deposits as replacement for cadmium,” (2007), *Surf. Coatings Technol.*, vol. 201, no. 18, pp. 7896–7904.
- [15] I. H. Karahan, A. Tozar and “Structural and corrosion protection properties of electrochemically deposited nano–sized Zn–Ni alloy coatings,” (2014), *Appl. Surf. Sci.*, v. 318, pp. 15–23.
- [16] Karolina Chat–Wilk, E. Rudnik, G. Włoch, and P. Osuch, “Codeposition of Zinc with Manganese from Different Gluconate Baths,” (2022), *Russ. J. Electrochem.*, v. 58, no. 3, pp. 168–183.
- [17] R. Winand, “Electrodeposition of metals and alloys–new results and perspectives,” (1994), *Electrochim. Acta*, v. 39, no. 8–9, pp. 1091–1105, 1994.
- [18] B. Scharifker, “Theoretical and experimental studies of multiple nucleation,” (1982), *Electrochim. Acta*, v. 28, no. 2, pp. 879–889, 1982.
- [19] G. B. Darband, M. Aliofkhazraei, A. Dolati, and A. S. Rouhaghdam, “Electrocrystallization of Ni nanocones from chloride–based bath using crystal modifier by electrochemical methods,” (2020), *J. Alloys Compd.*, vol. 818, p. 152843.
- [20] G. B. Darband, M. Aliofkhazraei, A. Dolati, and A. S. Rouhaghdam, “Electrocrystallization of Ni nanocones from chloride–based bath using crystal modifier by electrochemical methods,” (2020), *J. Alloys Compd.*, v. 818, p. 152843.
- [21] M. Ye, T. Ding, H. Zhou, and F. He, “Nucleation and growth mechanism of electrodeposited Ni – W alloy,” (2021), *Trans. Nonferrous Met. Soc. China*, vol. 31, no. 6, pp. 1842–1852, 2021.
- [22] R. Asseli, M. Benaicha, S. Derbal, M. Allam, and O. Dilmi, “Electrochemical nucleation

- and growth of Zn–Ni alloys from chloride citrate–based electrolyte,” (2019), *J. Electroanal. Chem.*, v. 847, no. June, p. 113261, 2019
- [23] L. A. Azpeitia, C. A. Gervasi, and A. E. Bolzán, “Electrochemical aspects of tin electrodeposition on copper in acid solutions,” (2019), *Electrochim. Acta*, v. 298, pp. 400–412.
- [24] L. Allam, F. Lazar, B. Benfedda, and J. P. Chopart, “Zn–Mn alloy coating elaboration by magnetoelectrodeposition,” (2021), *J. Solid State Electrochem.*, v. 25, no. 7, pp. 2041–2053.
- [25] M. Rezaei, S. H. Tabaian, and D. F. Haghshenas, “Nucleation and growth of Pd nanoparticles during electrocrystallization on pencil graphite,” (2012), *Electrochim. Acta*, v. 59, pp. 360–366.
- [26] G. A. Gunawardena, G. J. Hills, and I. Montenegro, “Potentiostatic studies of electrochemical nucleation,” (1978), *Electrochim. Acta*, v. 23, no. 8, pp. 693–697.
- [27] Y. Yuan, G. Luo, and N. Li, “New in situ description of electrodepositing multiple nucleation processes under galvanostatic stimuli,” (2021), *RSC Adv*, 11,31526.
- [28] A. Zandiatashbar *et al.*, “Effect of defects on the intrinsic strength and stiffness of graphene,” (2014), *Nat. Commun.*, v. 5, pp. 1–9.
- [29] Z. Xiong, L. Zhong, H. Wang, and X. Li, “Two–Dimensional Materials,” (2021), pp. 1–39.
- [30] K. H. Cheng *et al.*, “Fabrication of Ni–Mn microprobe structure with low internal stress and high hardness by employing DC electrodeposition,” (2014), *Adv. Mater. Sci. Eng.*, v. 2014, 2014
- [31] Akiyama. T. and Fukushima. H., “Recent Study on the Mechanism of the Electrodeposition of Iron–group Metal Alloys,” (1992), *ISIJ Int.*, v. 32, no. 7, pp. 787–798.
- [32] Assaf. F. H., Abou–Krisha. M. M, Alduaij. El–Seidy. O. K, A. M. A., and Eissa. A. A., “The effect manganese concentration on the corrosion resistance and physical properties of Zn–Ni–Mn alloy films produced by electrodeposition,” (2015), *Int. J. Electrochem. Sci.*, v. 10, no. 8, pp. 6273–6287.
- [33] Chouia. F, Chala. A, Lakel. A, and Sahraoui. T, “Morphology and corrosion behavior

of Zn–Ni layers electrodeposited on low alloy carbon steel substrate,” (2021), *Ann. Chim. Sci. des Mater.*, v. 45, no. 3, pp. 225–230.

## ***Chapter IV***

### *Morphology, Structural characterization, and corrosion resistance of Ni–Mn and Zn –Ni –Mn coatings: Effects of $[Mn^{2+}]$*

---

*This section's main focus is on the influence of  $[Mn^{2+}]$  on the morphological, structural, and corrosion resistance of different Ni–Mn and Zn –Ni –Mn obtained coatings.*

---

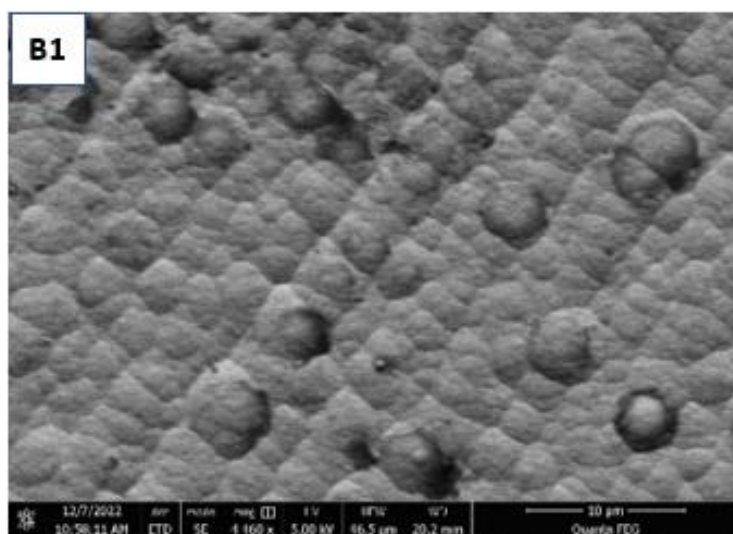
## IV.1. Morphology and crystalline structure of the obtained coatings

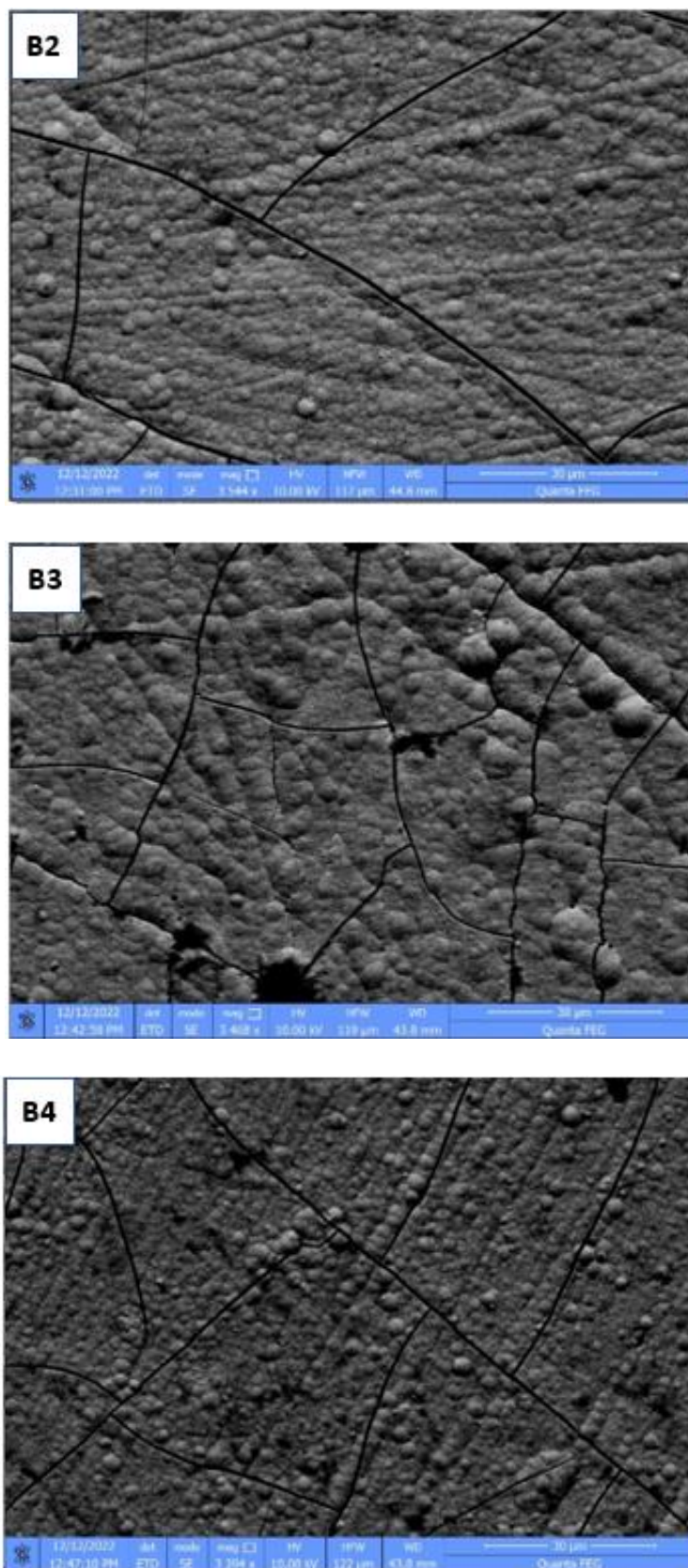
### IV.1.1. The coating's morphology

Utilizing SEM, an examination of the coatings surface morphology was conducted to evaluate the influence of Mn on the deposited and morphology of the deposits. ImageJ software was utilized for the examination of particle size distribution of the obtained coatings. ImageJ, a widely adopted open-source image processing and analysis tool developed by the National Institutes of Health (NIH) [1] plays a crucial role in processing and analyzing images of coatings to derive information about the sizes of particles.

#### IV.1.1.1. Surface morphology of Ni–Mn films

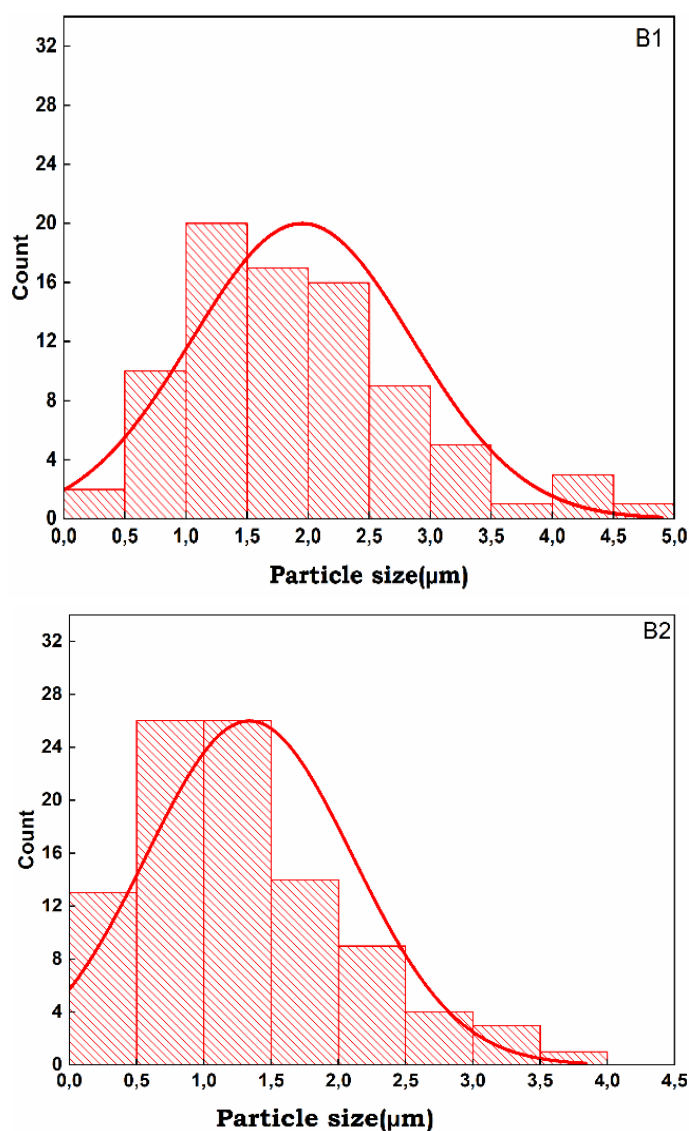
**Figure IV.1.** shows the SEM images of Ni–Mn coatings obtained with various  $[\text{Mn}^{2+}]$  in the bath. The deposits have a column-like morphology and the cauliflower-like agglomerates have different sizes with globular shape particles. The coatings exhibit a pin-hole morphology distributed on some regions of the surface for all the samples. The presence of cracks in coatings is mainly evident due to high residual stresses in the coatings owing to the evolution of hydrogen during the deposition of Ni–Mn coatings. This is a common behavior in electrodeposited Ni-based thin films. In fact, during electrodeposition, hydrogen atoms are generated and adsorbed on the surface of the coatings resulting in strong residual stress in the crystal lattice. Thereafter, the formation of cracks is possible after reaching a certain level of residual stress.



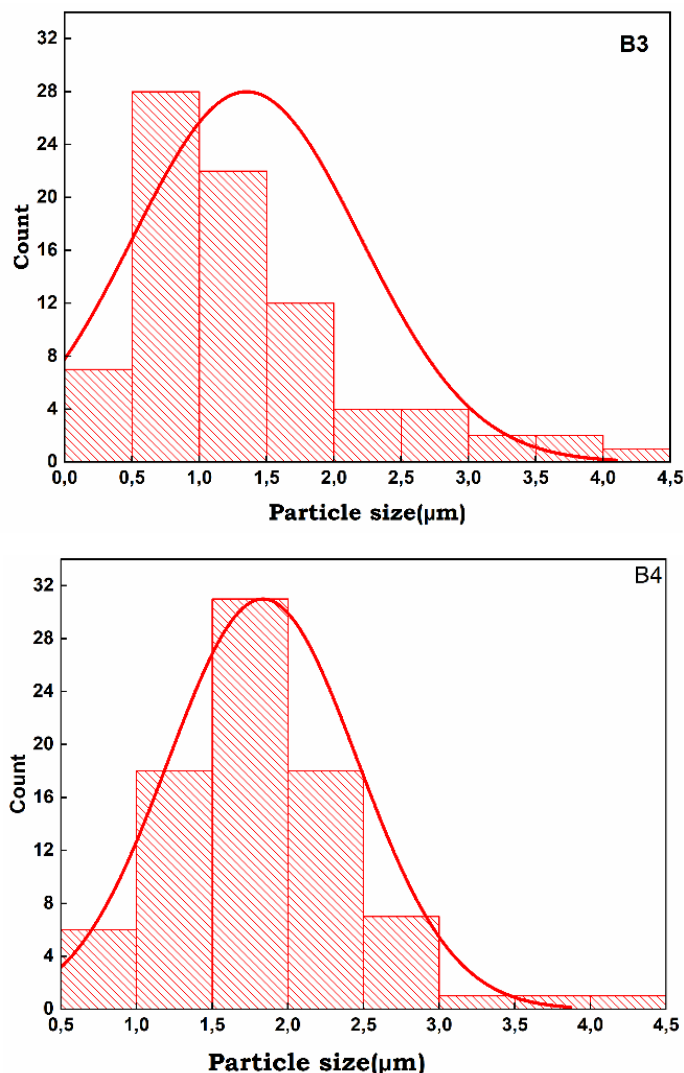


**Figure IV. 1.** SEM images of Ni-Mn films for various  $[\text{Mn}^{2+}]$  at -1V (vs. Ag/AgCl)

After investigating the influence of  $[\text{Mn}^{2+}]$  on the morphology of thin films, the particles size distribution was analyzed from SEM micrographs using ImageJ software. For binary **Ni–Mn** coatings, the corresponding histogram plots of particles size are shown in **figure IV.2**. It is noted that the particle's size distribution is large and spans the range  $\sim 0.5\div 5\ \mu\text{m}$  approximately. The inhomogeneity of size as revealed by the coexistence of bigger and smaller particles results from the competition between the nucleation and growth phenomena during the deposition process. The domination of fine particles for all  $[\text{Mn}^{2+}]$  can be related to the instantaneous nucleation process as revealed by CA results.



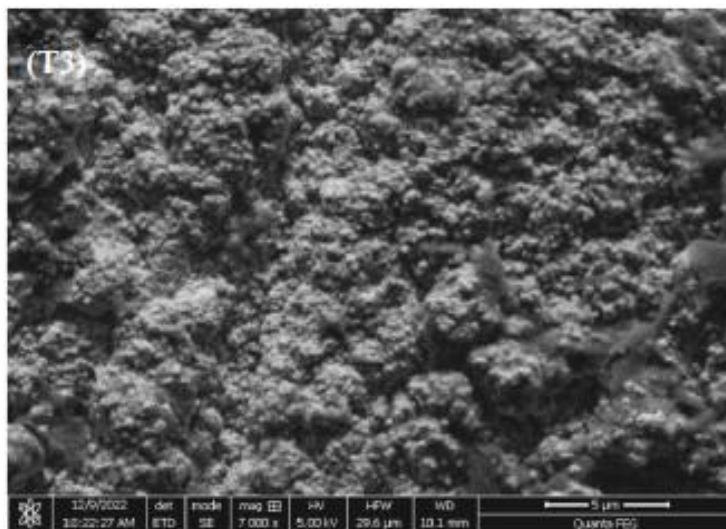
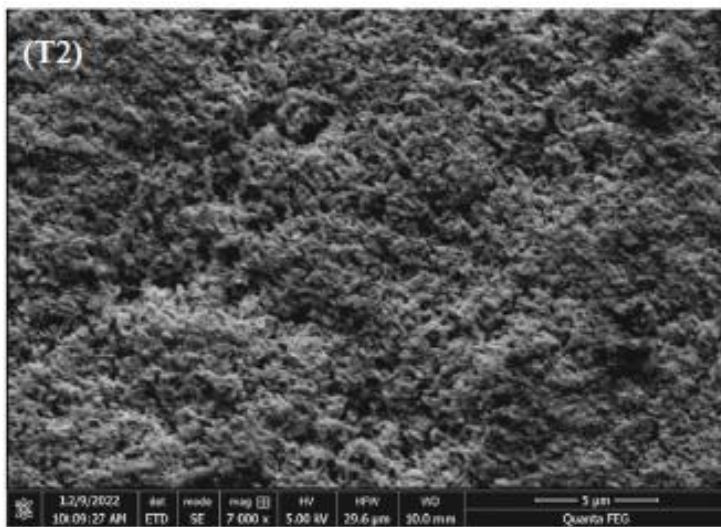
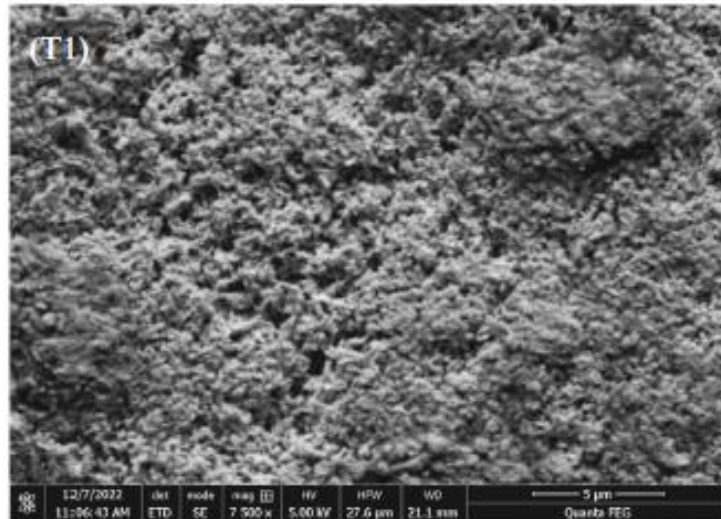


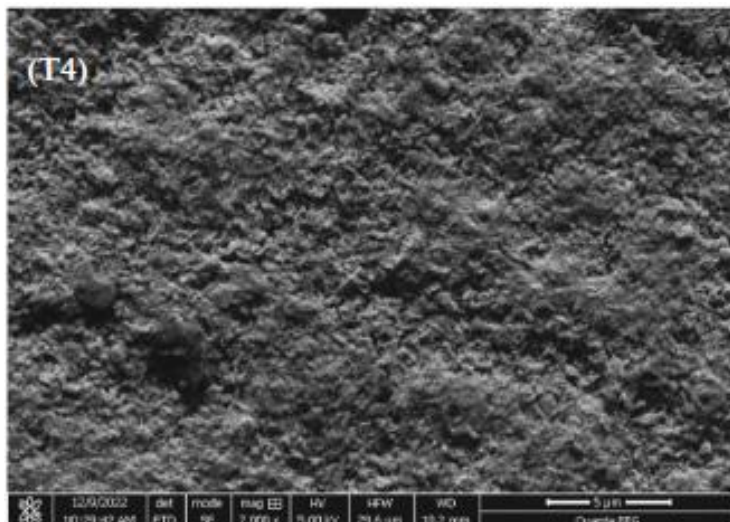


**Figure IV.2.** Histograms of the distribution of particles size in Ni–Mn coatings for different  $[\text{Mn}^{2+}]$ .

#### IV.1. 1.2. Surface morphology of Zn–Ni–Mn films

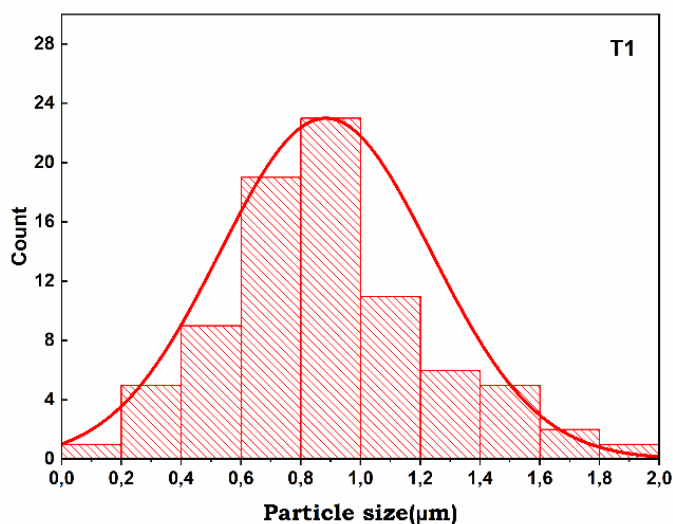
Figure IV.3 displays the SEM micrographs of Zn–Ni–Mn coatings obtained with various  $[\text{Mn}^{2+}]$  in the bath. It is evident from the SEM images that the surface morphology displays pyramidal-shaped particles, a characteristic feature of Zn deposit particles [2]. This finding can be attributed primarily to the prevalence of Zn content in the deposits, as confirmed by the EDX analysis. Additionally, no cracks are evident across the entire surface of the deposits. This observation indicates that Zn's existence could potentially reduce residual stress within the crystal. The morphology of the coating appears uniform, exhibiting a homogeneous distribution of particle sizes.





**Figure IV.3.** SEM images of Ni–Mn coatings for various  $[\text{Mn}^{2+}]$  content at  $-1.12\text{V}$  (vs. Ag/AgCl).

Figure IV.4 displays the evaluation of particle size distribution for Zn–Ni–Mn coatings using ImageJ software[3, 4]. It is noticeable that for all the obtained coatings, the particle sizes are uniformly distributed between  $0.2$  and  $2 \mu\text{m}$ . This finding holds significance as progressive nucleation is crucial for achieving maximum particle size homogeneity. An augmentation in the Mn deposited resulted in a slight increase in the number of particles within the size range of  $0.2$  to  $0.6 \mu\text{m}$ . This indicates that the rate of nucleation exceeds the growth rate of nuclei on the Cu interface. It aligns with prior discussions in the CA section, suggesting that the experimental data fall between theoretical progressive and instantaneous nucleation modes.



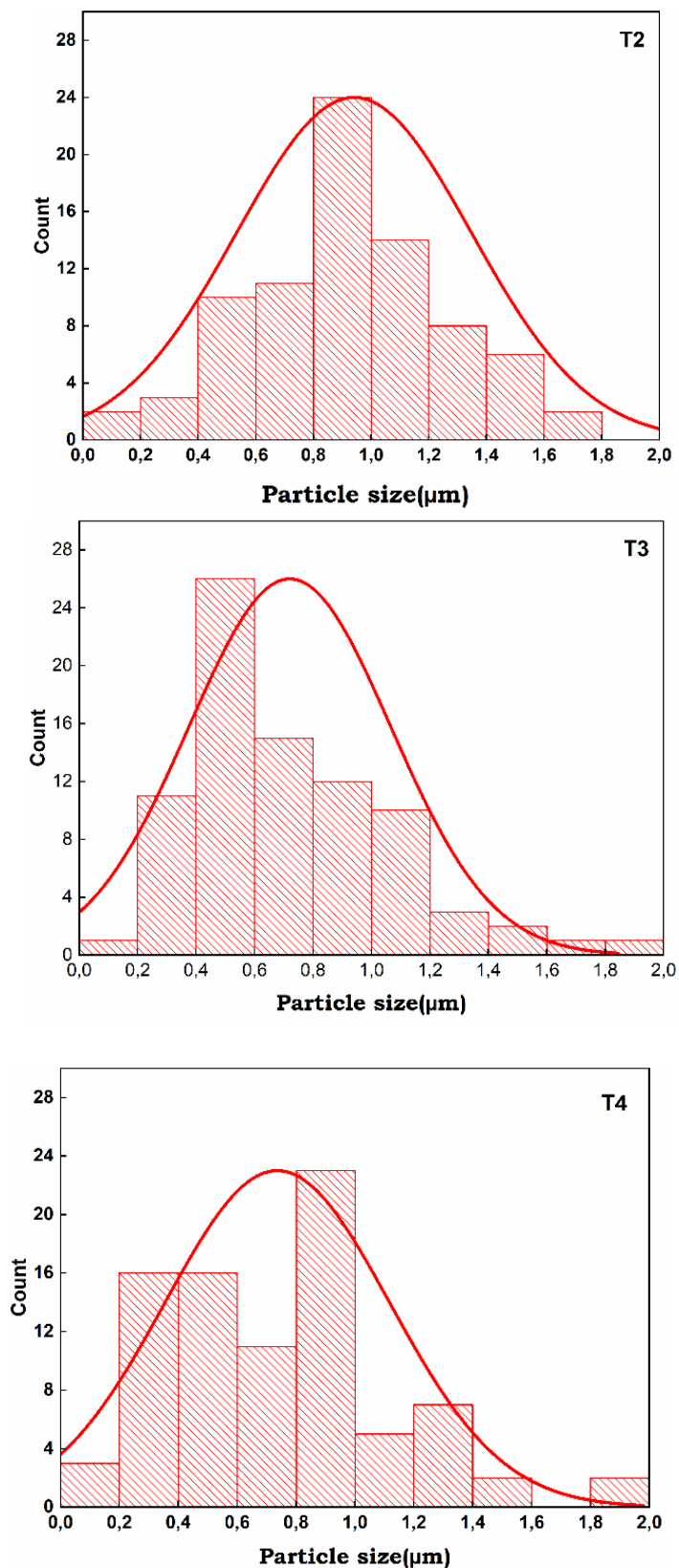


Figure IV .4 Histograms of the distribution of particles size in Zn-Ni-Mn coatings for various  $[Mn^{2+}]$ .

## IV.1.2. XRD analysis

### IV.1.2.1 Ni–Mn XRD analysis

The phase diagram of Ni–Mn alloys is known to be highly intricate, exhibiting diverse phases influenced by the composition of the plating solution and deposition parameters. Typically, the observed phases predominantly rely on the Mn content present within the alloy [5]. The crystalline structure of Ni–Mn deposits with different Mn concentrations was determined by XRD as can be seen in figure IV.5. The obtained XRD diffractograms indicate the presence of same peaks attributed to pure Ni in all diagrams. The crystal structure of Ni (JCPDS 01-089-7128) is characterized by three preferred orientations, namely Ni (1 1 1), (2 0 0) and (2 2 0) planes of the face-centered cubic (fcc) structure, corresponding to  $2\theta$  angles of  $44.35^\circ$ ,  $50.66^\circ$  and  $74.49^\circ$  respectively. Additionally, the diffraction patterns show the presence of Cu peaks (JCPDS N° 003–1018) at  $2\theta = 43^\circ$  due to the substrate. It is worth noting that no specific diffraction patterns corresponding to Mn and NiMn can be detected in all diffractograms. This observation suggests that Mn atoms are effectively incorporated into the nickel lattice and formed a solid solution. Incorporating Mn into the nickel lattice may influence arrangement of atoms in the lattice, leading to alterations in atomic distances, bond angles, and the overall symmetry of the lattice. The variations in the Mn content can result in modifications to the lattice parameters with no formation of new phase.

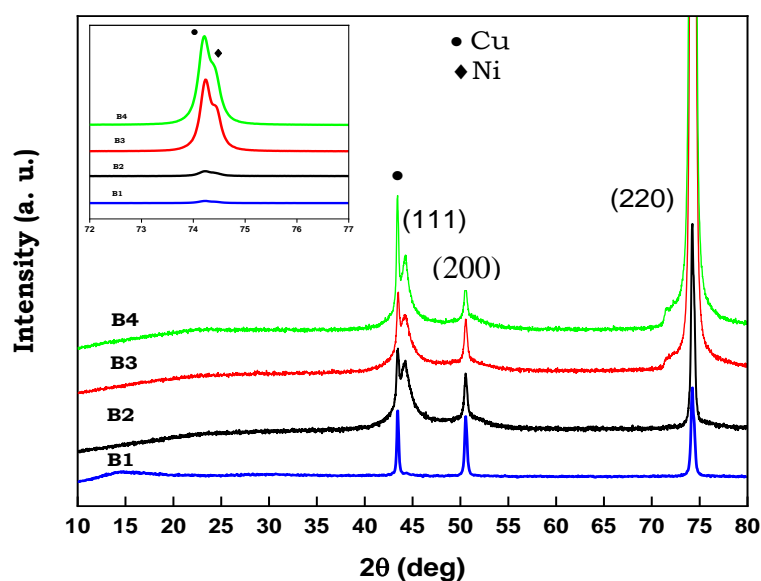


Figure IV.5. XRD patterns of Ni–Mn coatings with different Mn contents.

#### IV.1.2.2 XRD examination of Zn–Ni–Mn films

XRD patterns of Zn–Ni–Mn coatings, obtained from baths with different concentrations of  $[Mn^{2+}]$ , are presented in Figure IV.6. The appearance of sharp and narrow diffraction peaks at various  $2\theta$  positions results from the formation of Zn–Ni–Mn films with distinct crystalline phases. Thorough examination of the XRD patterns, it is evident that three primary phases coexist, namely cubic Cu (JCPDS No 003–1018),  $\eta$ -Zn (JCPDS N° 96–901-3474), and  $NiZn_3$  (JCPDS No 00-047-1019) phases. It is noted that Bragg peaks related to various formed phases are detected in all samples, with varying relative intensities. The existence of Cu peaks can be attributed to the Cu substrate, whereas the formation of  $\eta$ -Zn and  $NiZn_3$  phases is supported by the presence of Zn, Ni, and Mn in the Zn–Ni–Mn coatings.

The ( $\eta$ -Zn) phase crystallizes in the compact hexagonal system similar to pure Zn. This represents a Zn(Mn) solid solution with low Mn content (1-5 wt.% Mn), resulting from the complete dissolution of Mn atoms into the Zn matrix [6]. Indeed, various phases are recorded in the Zn–Mn coating as well as the structural changes primarily depend on the Mn content in the films, which is in turn influences directly by the deposition conditions. Previous studies have indicated that the crystalline structure of electrodeposited Zn–Ni coatings comprises a combination of three distinct phases ( $\alpha$ ,  $\gamma$ , and  $\eta$ ), which vary according to the Ni content in the coatings [7]. Zn–Ni coatings with more than 70 wt. % Ni only show  $\alpha$  phase. whereas the creation of the pure  $\gamma$  phase is noted as the Ni content falling between 10 and 30 wt. %. Beyond these specified ranges, Ni–Zn coatings demonstrate a mixture of two phases. For higher Ni content, the observed combination is ( $\alpha+\gamma$ ), while for lower Ni content, it consists of ( $\eta+\gamma$ ) phases [8]. In the current investigation, the chemical analysis of Zn–Ni–Mn coatings demonstrates a Ni content within the range of 20–37.7 wt.%, with detected reflections matching the  $\gamma$ -phase  $NiZn_3$  (00-047-1019) [14]. This complex phase is associated with a  $\gamma$ -brass type structure characterized by orthorhombic symmetry, contributing significantly to the enhancement of corrosion resistance in Zn–Ni coatings [9]. It's worth noting that there are no peaks attributed to pure Ni, Zn, and Mn phases, signifying the full dissolution of Ni and Mn into the Zn matrix. Furthermore, the XRD findings confirmed that changes in the coatings' composition did not influence phase formation, as evidenced by the absence of new peaks associated with the emergence of novel

phases or modifications to existing ones, nevertheless, there is a noticeable influence on the intensity of different Bragg peaks, reflecting variations in the proportions of distinct phases. Additionally, as illustrated in Figure IV.6, the augmentation of Mn content in the coatings is correlated with the broadening of various peaks and a reduction in their intensity. This is primarily because of the substantial reduction in crystallite size and the heightened lattice strain. This phenomenon is consistent with the SEM results mentioned earlier, suggesting that the arrangement and microstructure of the deposits are predominantly affected by the first steps of crystal growth and nucleation that occur during electrodeposition.

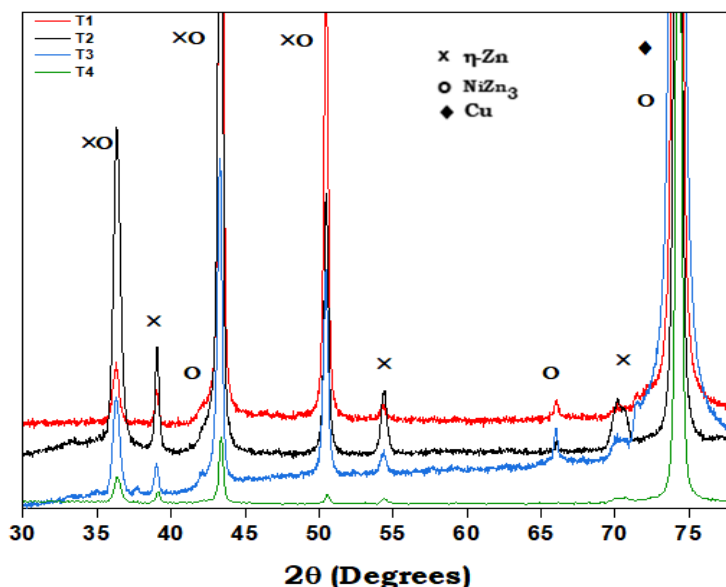


Figure IV. 6. XRD patterns of Zn–Ni–Mn coatings with varying Mn deposited.

## IV.2. Influence of Mn content on Corrosion behavior

### IV.2.1. Loss mass method

The corrosion rates of the coatings immersed in a NaCl solution were determined at 25°C. The obtained corrosion rates ( $\tau$ ) are presented in table IV.1.

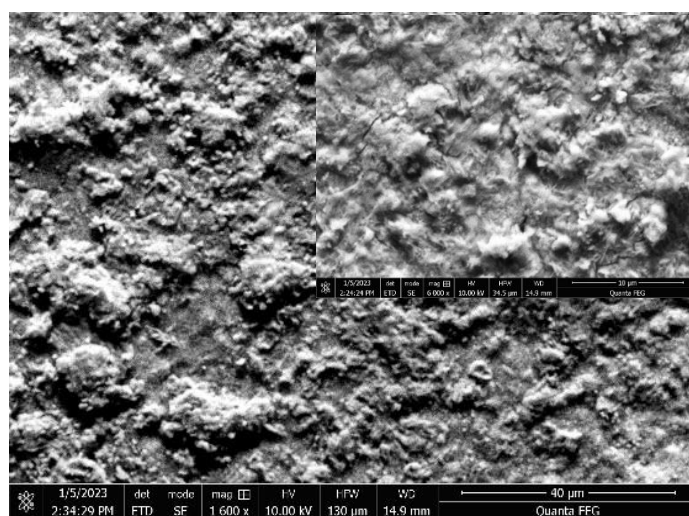
Table IV.1. Results of loss mass method

	Substrate	Ni	Ni–Mn	Zn–Ni–Mn
$m_i$ (g)	0.3425	0.3842	0.3293	0.4551
$m_f$ (g)	0.3401	0.3824	0.3290	0.4550
$\Delta m$ (g)	0.0024	0.0018	0.0003	0.0001
$\tau$ (g/cm <sup>2</sup> /year)	0.0180	0.0135	0.0022	0.0004

The above table illustrates the measurements of the metal's mass to monitor variations in corrosion rates of Ni, Ni–Mn, and Zn–Ni–Mn coatings dipped in sodium chloride solution. It is evident that the mass of the metals has gradually decreased during the course of the exposure period, signifying corrosion in the saline environment. Notably, the substrate exhibited a substantial mass loss compared to nickel and other alloys, suggesting that the substrate corroded more quickly. It's also noted that the mass loss in Ni–Mn is less than that in Ni. Additionally, the loss mass value for the Zn–Ni–Mn is lower than the combined missing mass values of Ni and Ni–Mn coatings. These results revealed that coatings have significantly reduced the Cu substrate corrosion. Moreover, it is obvious that the unique metal results from Zn, Ni, and Mn combination have greater corrosion resistance compared to Ni and Ni–Mn alloy.

#### IV.2.1.1. Morphology of Ni–Mn coatings after corrosion

The SEM image of sample B<sub>1</sub> after two weeks of exposure to a 3.5% NaCl solution is depicted in **Figure IV.7**. The sample surface has evidently damaged and the coating has displayed a rough surface. Additionally, the presence of porosity in corrosion products is evident, accompanied by a few minor fissures. These fissures likely resulted from the galvanic cell formed between Ni and Mn at the grain boundary regions. The existence of pores on the surface may result from the dynamic interplay involving the formation of the protective oxide film and the dissolution of the coating

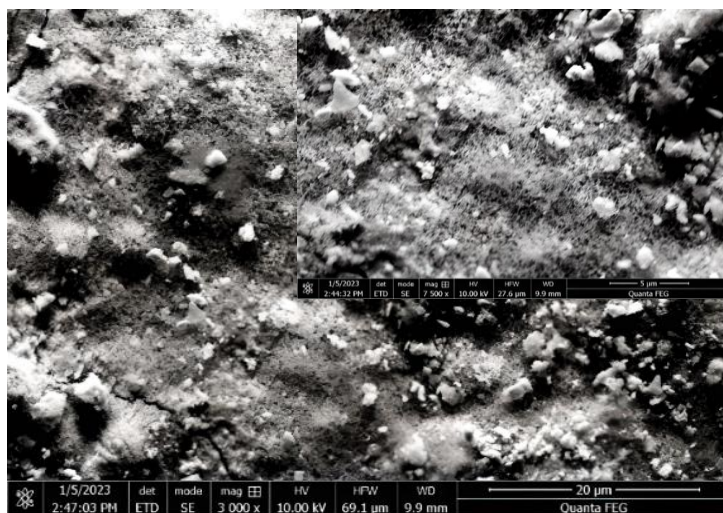


**Figure IV.7.** SEM image of Ni–Mn (sample B<sub>1</sub>). coatings after corrosion



#### IV.2.1.2. Morphology of Zn–Ni–Mn films coatings after corrosion

Figure IV.8. displays SEM image of the protective oxide layer on the surface of Zn–Ni–Mn film ( $T_1$ ) following a two-week immersion in an aggressive testing medium. The surface of the coating appears to be fully enveloped by the protective oxide layer, characterized by a non-uniform, highly porous microstructure featuring particles of various shapes and sizes. The existence of surface pores can be attributed to the dynamic interplay between the creation of the protective oxide layer and the dissolution of the films.



**Figure IV.8.** SEM image of corroded Zn–Ni–Mn films ( $T_1$ ).

#### IV.2.1.3 XRD analyses of Ni–Mn films coatings after corrosion

The obtained XRD pattern (Figure IV.9) reveals noticeable diffraction peaks of pure Ni peaks at  $2\theta$  angles of  $44^\circ$  and  $51^\circ$ , as mentioned previously. Additionally, distinct diffraction peaks were observed at  $2\theta$  angles of  $15^\circ$ ,  $30^\circ$ ,  $34^\circ$ , and  $37^\circ$  corresponding to Ni (OH)  $Cl_2$  phase (JCPDS card (N $^\circ$ . 03–1051)). Moreover, distinct diffraction peaks were identified at  $2\theta$  angles of  $12^\circ$ ,  $23^\circ$ , and  $65^\circ$ , which correspond to the Mn oxide phase,  $MnO_2$ , (JCPDS (N $^\circ$ . 80–1098) card).

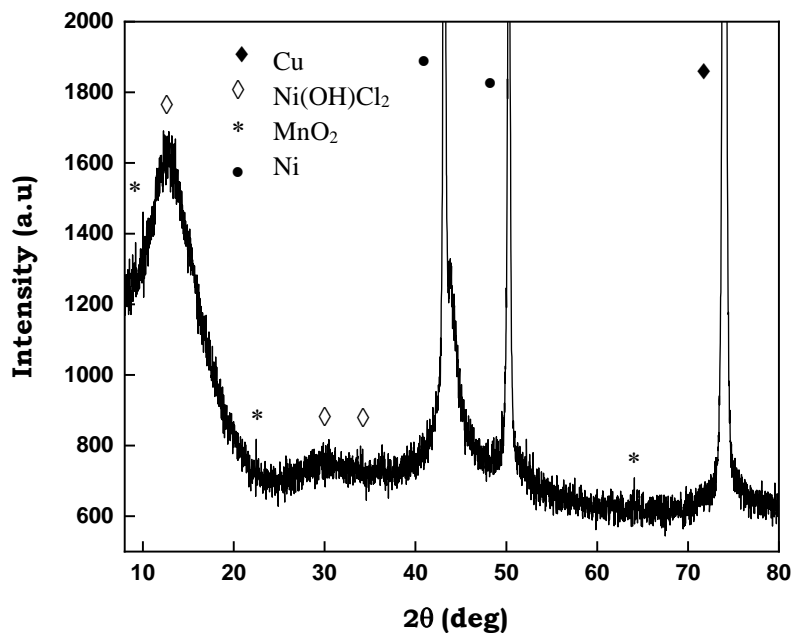
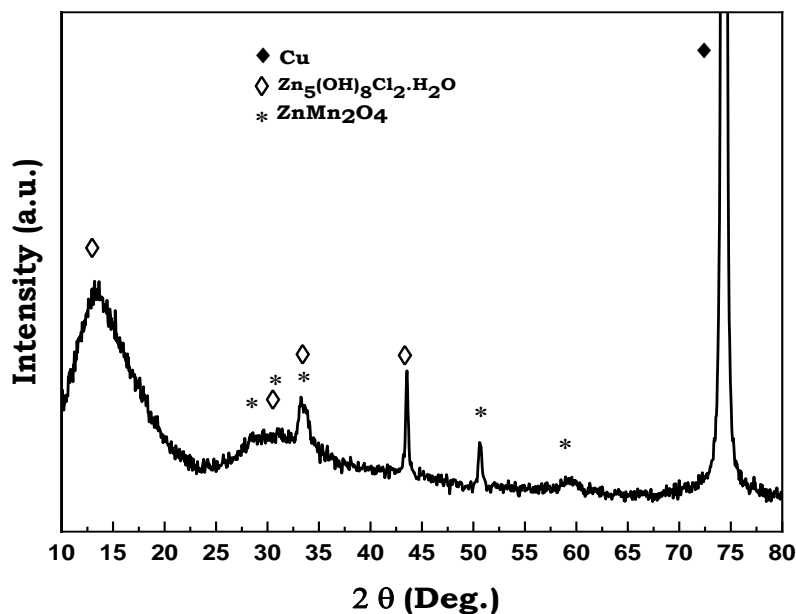


Figure IV.9. XRD patterns Ni-Mn films coatings after corrosion

#### IV.2.1.3 XRD analyses of Zn-Ni-Mn films coatings after corrosion

The XRD technique was employed to analyze the crystalline structure of the corrosion products developed on the Zn-Ni-Mn coating ( $T_1$ ) following two weeks of immersion in a 3.5 wt.% NaCl aggressive liquid. In Figure IV.10, various Bragg peaks with low intensity are observed, indicating the presence of different oxide and hydroxide chloride phases, such as  $Zn_5(OH)_8Cl_2$ , ZnO, and  $ZnMn_2O_4$ . This is attributed to the diffusion of  $O_2$ ,  $H_2$ , and/or  $Cl_2$  within the coating. Additionally, narrow Bragg peaks associated with the  $NiZn_3$  phase can also be detected due to the minimal thickness of the corrosion product.



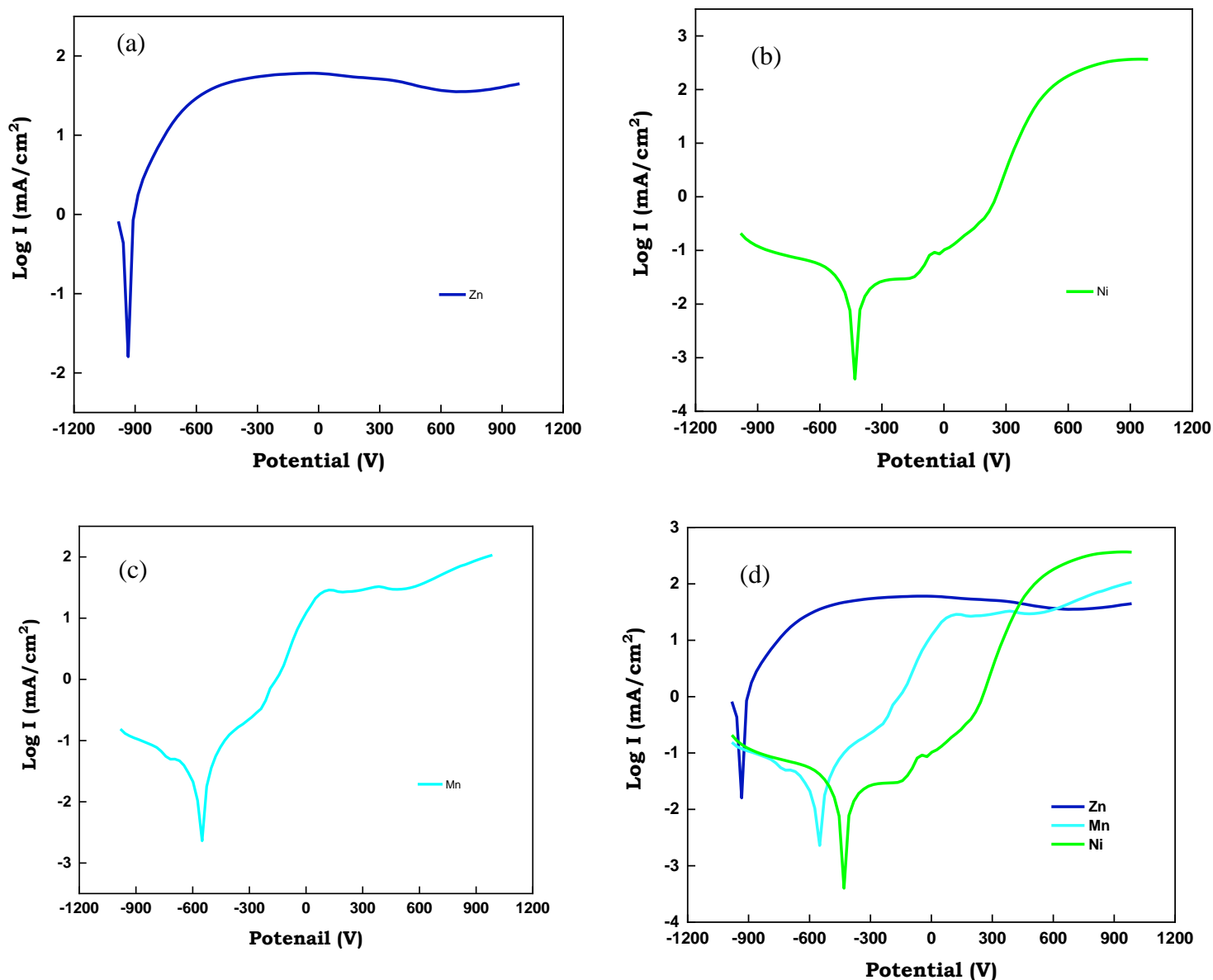
**Figure IV.10:** XRD pattern of the corroded Zn–Ni–Mn film (T1).

## IV.2.2. Linear polarization resistance analyses (LPT)

### IV.2.2.1. Linear polarization resistance of Ni, Zn, and Mn

Figure IV.11. illustrates the LPT curves of Zn, Ni and Mn coatings after subjecting in a corrosive media 3.5% NaCl. The figure reveals that the Ni coating exhibited a more favorable positive potential and lower current densities compared to Zn and Mn films, This suggests better corrosion resistance of the Ni film, aligning with previous studies[10]. Additionally, the Ni films feature both a passive region and pitting tendency. The passive region indicates the formation of a protective oxide layer on the surface, which decreases the corrosion rate. The presence of pits on the surface indicates that the films are susceptible to localized corrosion [11]. Notably, Zn deposits exhibit height corrosion current and more negative corrosion potentials than Mn, indicating a lower corrosion resistance. It can function as a sacrificial coating. Additionally, the presence of a substantial passive film on the zinc deposits serves as a protective barrier, further reducing the corrosion of the substrate by separating it from the corrosive medium. The absence of pitting tendency indicates that the Zn films possess self-repairing capabilities., Moreover, it is clearly observed that the studied Mn corrosion potential (-0.55 V) significantly differs from that of the existing literature [12]. This difference could be attributed to several factors, including differences in experimental

conditions and the real-world environment. and impurities, which may influence its corrosion potential differently compared to laboratory settings.



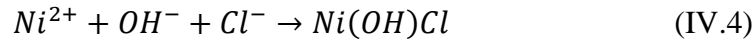
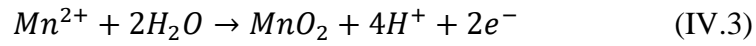
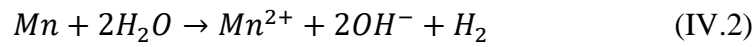
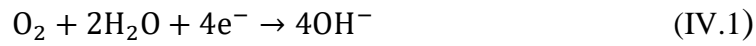
**Figure IV.11.** a), b), and c) LPT curves of Zn, Ni, and Mn coatings. d) Comparison of different curves.

#### IV.2.2.2 Linear polarization resistance of Ni–Mn films

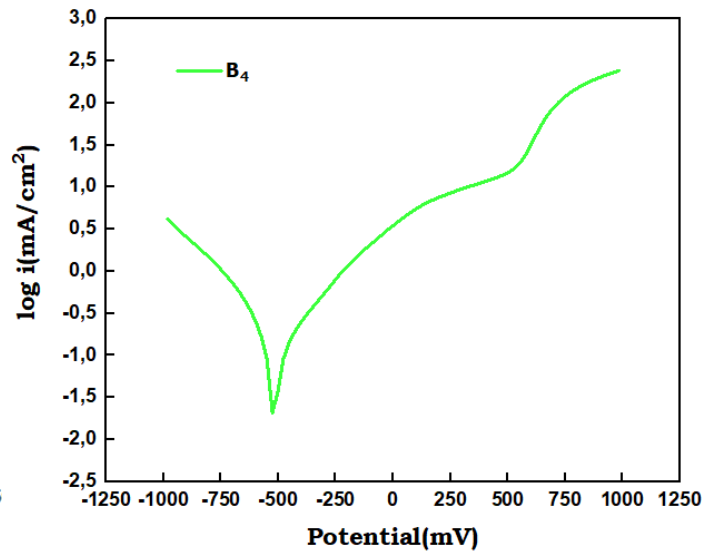
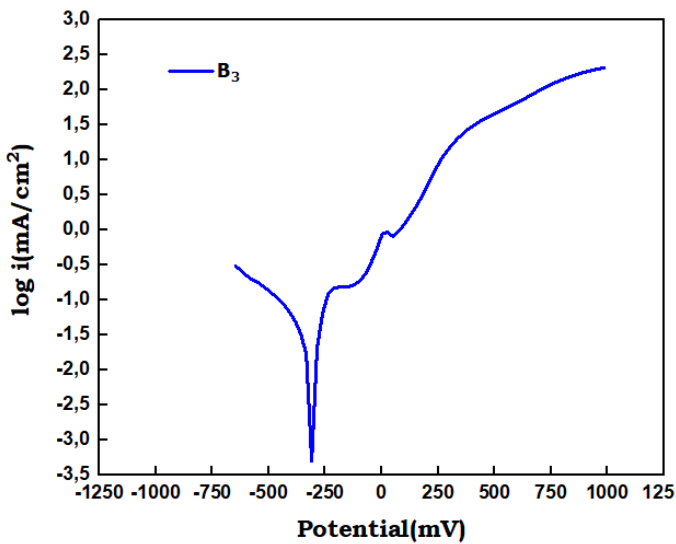
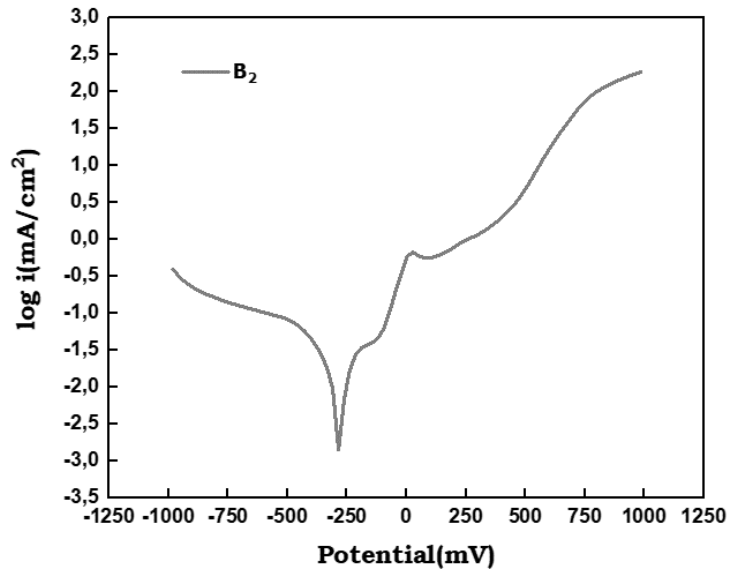
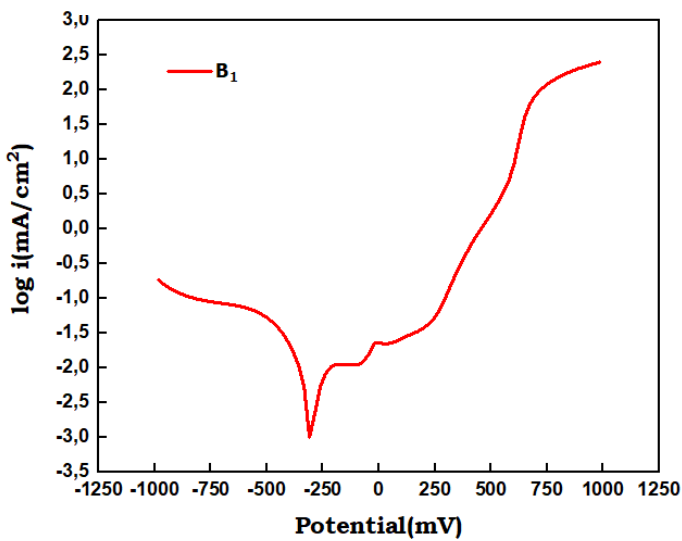
**Figure IV.12.** displays the typical LPT curves of the obtained Ni–Mn coatings immersed in 3.5 wt.% NaCl solution after 1 h of exposure and stabilization of potential. By comparing the Tafel curves, it can be noted that the cathodic regions of the Tafel curves of all Ni–Mn films show no plateau trend. The anodic region shows a corrosion

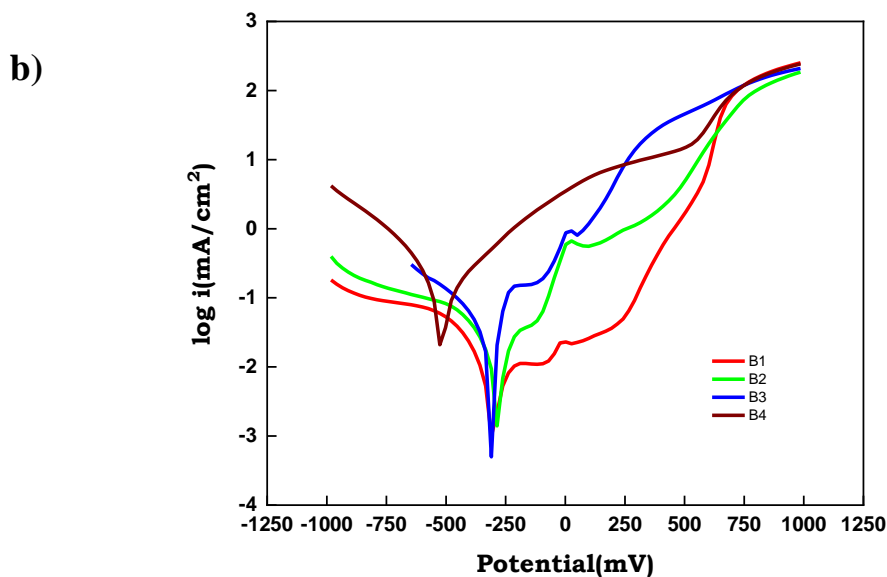
zone before reaching a passive area, between the passivation breakdown potential,  $E_b$ , and the corrosion potential ( $E_{corr}$ ), related to the creation of a stable passive film on the coating's interface.

The of corrosion potential values,  $E_{corr}$ , corrosion current density,  $I_{corr}$ , and polarization resistance,  $R_p$ , are established and noted in table IV.2. It can be clearly observed, in tableIV.2, that the corrosion behavior of Ni–Mn films is directly affected by the chemical composition of the coatings. The corrosion current density,  $I_{corr}$ , increases from 0.009 to 0.235  $\mu\text{A}/\text{cm}^2$  with the rise of the Mn content in the films according to the rise in the dissolution rate of the coatings. Simultaneously, the corrosion potential,  $E_{corr}$ , shifted to more negative values from  $-0.299$  to  $-0.514$  V (Ag/AgCl) while the corrosion resistance,  $R_p$ , decreases from 17 to 0.37 k $\Omega$ . This indicates the nobler character of the coatings by decreasing Mn content in the deposits. Indeed, the coating with low Mn content of 1.5 wt. % exhibits the highest corrosion resistance value of 17 k $\Omega$ . These results indicate that the incorporation of a small quantity of Mn in the bath can notably enhance the corrosion resistance of the resultant films. Furthermore, figure IV.b. 12 reveals that all the coatings exhibit a passive area in the anodic region indicating the formation of a stable protective passive layer on the interface which seems to be Ni hydroxide. The passivation phenomenon of Ni–Mn coatings, leading to the formation of a protective surface, can be described by the following steps: (i) Initially, in the anodic region, the dissolution of oxygen leads to the formation of hydroxyl group (Eq.IV.1). (ii) In the cathodic region, the dissolution of Mn atoms and the formation of  $\text{Mn}^{2+}$  ions take place through the reaction IV. 2. Mn atoms dissolves more quickly than Ni atoms because Ni has a higher potential ( $E_{\text{Ni}/\text{Ni}^{2+}} = -0.257\text{V}$  vs. ENH and  $E_{\text{Mn}/\text{Mn}^{2+}} = -1.18$ . vs. ENH) The Mn dissolution associated with the reduction of hydrogen reaction making the medium more alkaline. (iii) Thereafter, the reaction of  $\text{Mn}^{2+}$  and  $\text{Ni}^{2+}$  metal ions with the aggressive medium (Eq. IV.3and 4) takes place leading to the formation of corrosion products of  $\text{MnO}_2$  oxide and  $\text{Ni}(\text{OH})\text{Cl}$  hydroxide as a protective layer[4].



a)





**Figure IV.12.a).** LPT curves of Ni–Mn films obtained in the sulfate bath with various  $[\text{Mn}^{2+}]$ , following immersion in a 3.5 wt. % NaCl medium for 1 hour.

**b).** Comparison of different curves.

**Table IV.2.** Corrosion characteristics and chemical composition of Ni–Mn films developed with varying  $[\text{Mn}^{2+}]$ .

	<b>E<sub>corr</sub></b> (mV)	<b>I<sub>corr</sub></b> $\mu\text{A}/\text{cm}^2$	<b>R<sub>p</sub></b> (K $\Omega$ )	<b>Mn</b> wt. %	<b>Ni</b> Wt. %
<b>B1</b>	-0.299	0.009	17	1.6	96.9
<b>B2</b>	-0.282	0.023	4.26	2.3	96.2
<b>B3</b>	-0.307	0.047	1.48	3	95.7
<b>B4</b>	-0.514	0.235	0.37	4.6	94.1

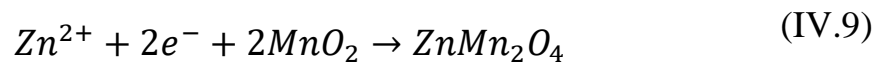
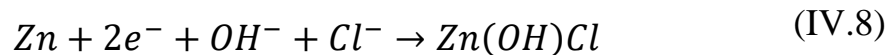
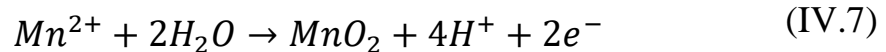
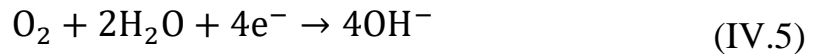
#### IV.2.2.3. Linear polarization resistance of Zn–Ni–Mn

The LPT curves for various Zn–Ni–Mn coatings are displayed in Figure IV.13. It is evident that all curves exhibit similar behavior, with the absence of pitting corrosion.

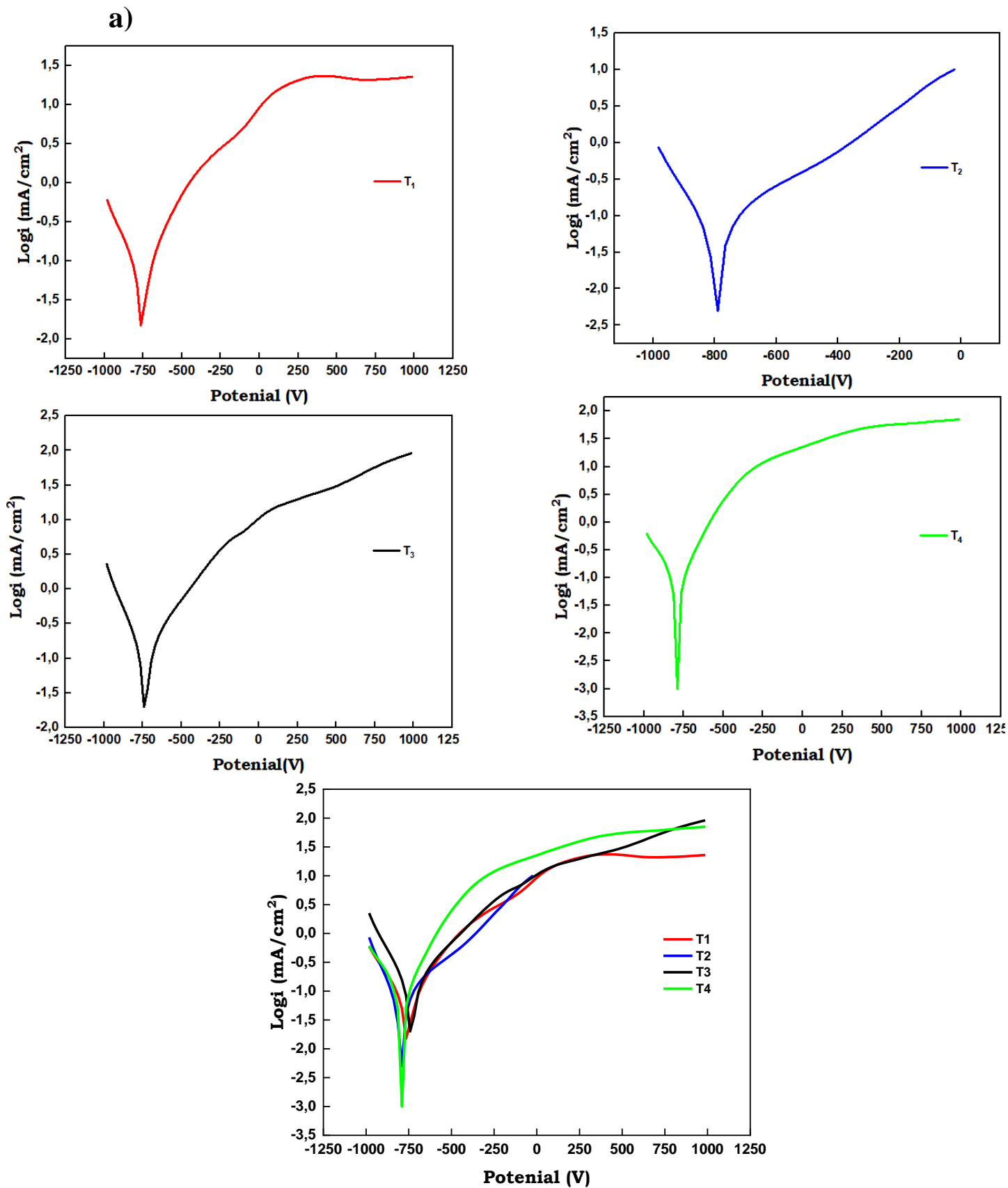
This observation may be attributed to the capacity of the formed protective layer to self-repair, thus preventing pitting corrosion in the chloride medium. The corrosion parameters are determined and listed in Table IV 3. The observed findings demonstrate that these parameters are influenced by the composition of the film, which is directly

associated with the composition of the bath. Therefore, adjusting  $[Mn^{2+}]$  in the bath results in an increase in the corrosion current density ( $I_{corr}$ ) values from 34 to 91  $\mu A/cm^2$ , a shift of the corrosion potential ( $E_{corr}$ ) to more negative values, and a decrease in corrosion resistance from 8.76 to 0.48  $K\Omega$ . It's noteworthy that the film with Zn, Ni, and Mn contents of approximately 55.7%, 37.7%, and 1.6% by weight, respectively, exhibits the lowest  $I_{corr}$ , the most positive  $E_{corr}$ , and the highest  $R_p$  values.

The resistance of corrosion of the resulting Zn–Ni–Mn films is attributed to the formation of a protective layer on the active sites of the interface of films, as outlined by the following mechanism. During the dissolution of Zn–Ni–Mn films, Mn dissolves initially due to its strong chemical reactivity, resulting in an increase in pH at the interface of the coating and the aggressive medium. This leads to the formation of  $Mn^{2+}$  ions, which interact with the medium ( $H_2O$ ), resulting in the creation of  $MnO_2$ oxide, as indicated in (Eq.IV.5, 6) [13-15]. Subsequently, Zn dissolution occurs, reacting with the medium to produce hydroxide chloride of Zn, as described in (Eq. IV. 7)[16 ,17]. Therefore, the dissolution of Mn and Zn leads to the formation of a compact passive layer  $ZnMn_2O_4$ , as outlined in (Eq. IV. 9) [18] .







FigureIV.13: a) LPT curves of Zn–Ni–Mn films obtained in the sulfate bath with different  $[\text{Mn}^{2+}]$ , following immersion

for 1 hour in a 3.5 wt. % NaCl medium. **b).** Comparison of different curves.

**Table IV.3.** Corrosion characteristics and chemical composition of Zn–Ni–Mn films developed with varying  $[\text{Mn}^{2+}]$ .

	$E_{\text{corr}}$ (mV)	$I_{\text{corr}}$ ( $\mu\text{A}/\text{cm}^2$ )	$R_p$ ( $\text{K}\Omega$ )	Zn (wt. %)	Ni (wt. %)	Mn (wt. %)	S (wt. %)
<b>T1</b>	-0.744	54	8.76	55.7	37.7	1.6	5
<b>T2</b>	-0.742	34	0.96	71.8	22.2	2.4	3.4
<b>T3</b>	-0.757	71	0.58	69.7	20	5.1	5.2
<b>T4</b>	-0.756	91	0.48	60.6	31.3	5.4	2.7

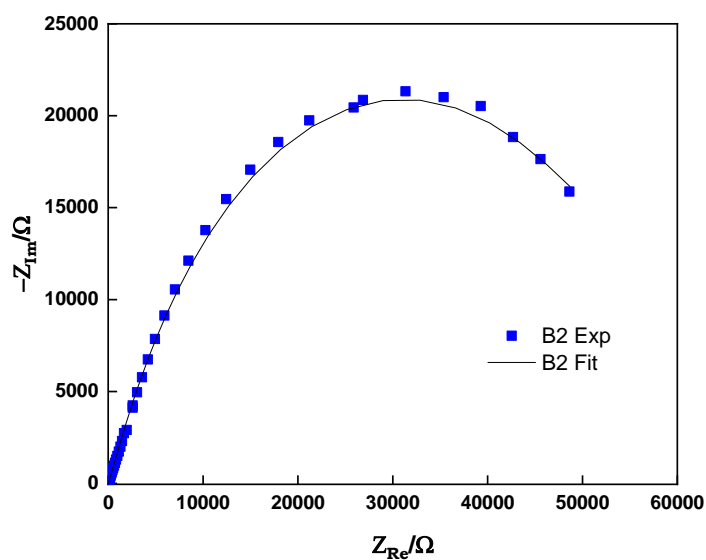
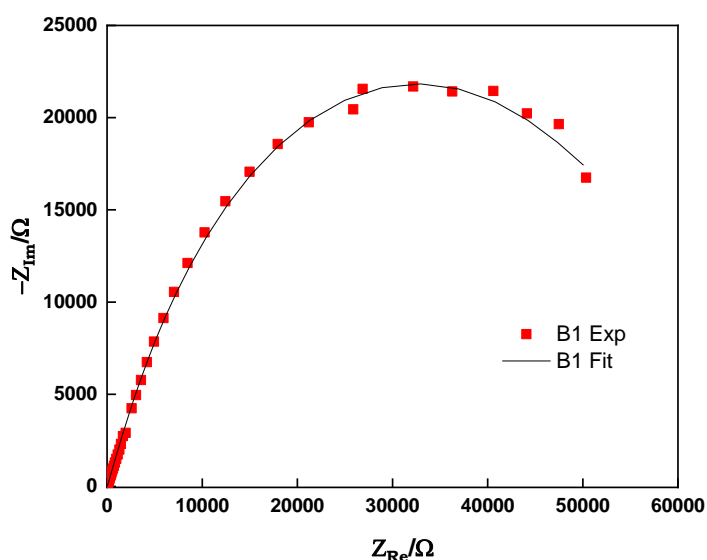
## IV. 2. 3. Electrochemical impedance analysis

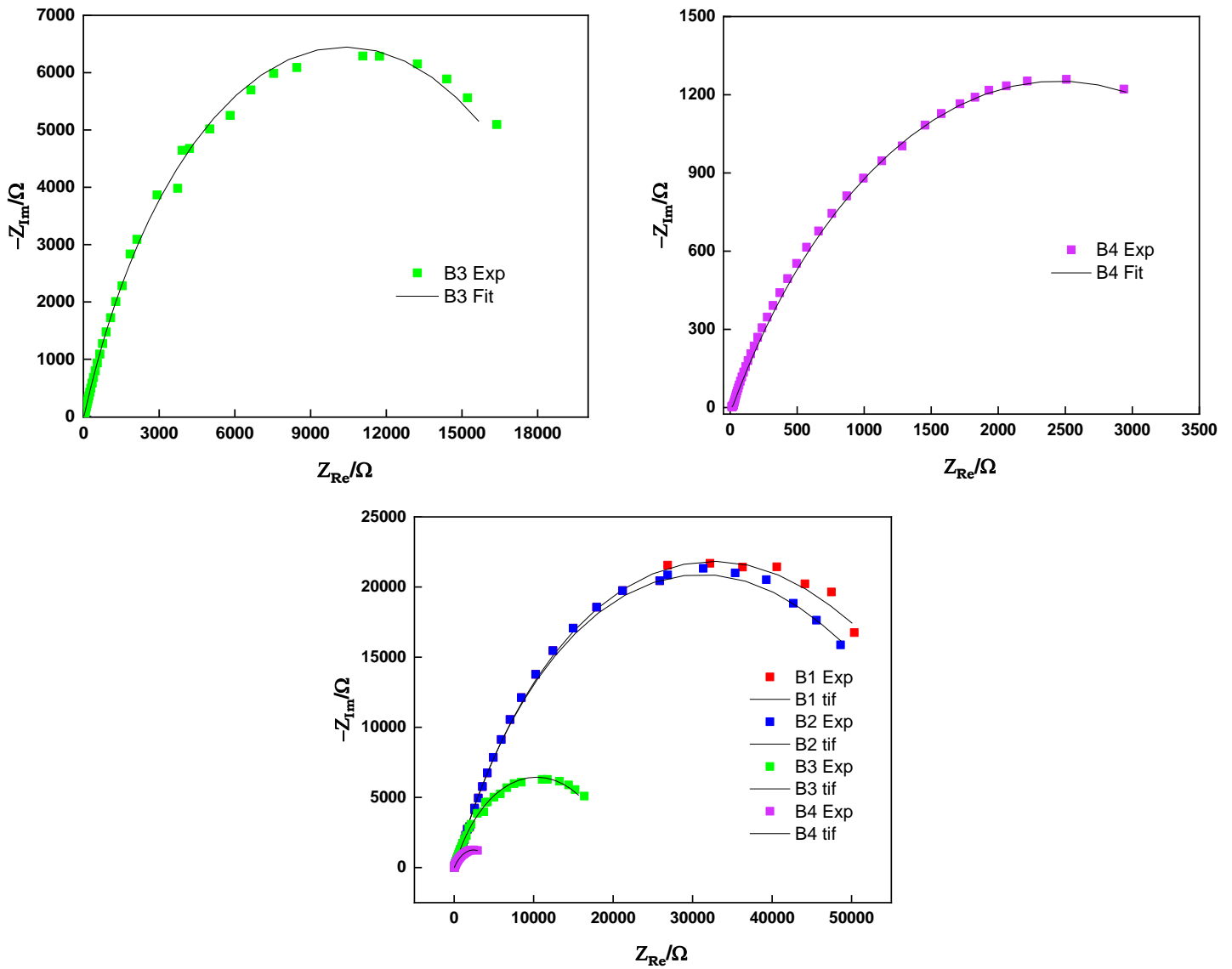
### IV.2.3.1. Electrochemical impedance spectroscopy of Ni–Mn coatings

EIS spectroscopy is employed to examine the features of the electrochemical reaction that predominates in corrosive environments at the electrode/solution interface [18,19]. In order to follow the corrosion resistance behavior of different films, the EIS tests were conducted on Ni-Mn coatings in 3.5 wt. % NaCl solution. As can be seen Figure IV. 14 (**a, and b**), Nyquist plots of diverse coatings exhibit semicircle loops. Typically, the semicircle represents the charge transfer resistance ( $R_{ct}$ ) at the electrode-electrolyte interface. As the Mn content deposits in the coatings increases, a noticeable decrease in the semicircle diameter is observed. The diameter of the semicircle in a Nyquist plot is directly linked to the charge transfer resistance, implying that an enlarged semicircle indicates an elevated resistance to charge transfer at the electrode-electrolyte interface [20,21]. Additionally, the augmentation of the deposit with Ni, a more noble element than Mn, has proven to enhance the corrosion resistance of the Ni-Mn deposit. This enhancement results in a more challenging transfer of electrons from the deposit's surface to the corrosive environment. Consequently, there is a reduction in double layer capacity, effectively diminishing the electroactive surface. These results indicate that modifications in Mn content deposits can induce changes in charge transfer resistance and alter the electrochemical behavior of the system.

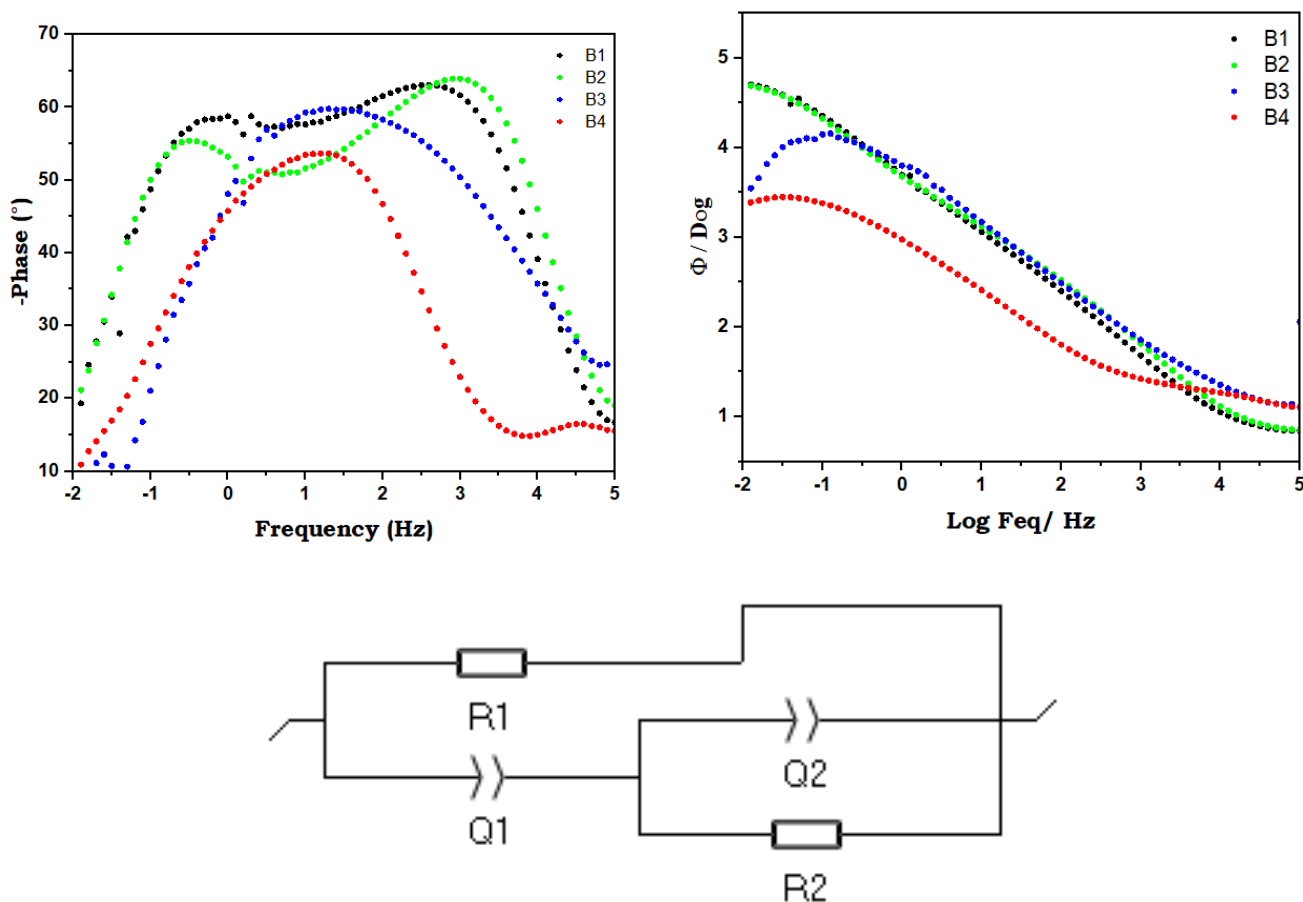
Based on the Bode plots (figure IV.15.a), the presence of maximum peak angles at high frequencies suggests the presence of a corrosion product film. Conversely, the peak angles, which are observed at low frequencies, can be attributed to the electric double layer. Notably, low Mn content samples which exhibit obvious peaks in the high-frequency region indicate a corrosion product layer formation. Similarly, significant peaks in the low-frequency region indicate a hindered charge transfer process.

The experimental data can be achieved by fitting a suitable equivalent circuit (EEC). As can be seen in figure IV.15.c). the equivalent circuit consists of a pair of elements in parallel, Q1 (representing the double electric layer) and R1 (representing the charge transfer resistance). These elements represent the electrical characteristic of the electric double layer at the interface of the corrosion product layer and the medium. Additionally, the equivalent circuit includes another pair of elements: Q2 (film capacitance) and R2 (film resistance), which elucidate the process of charge transfer through the corrosion product layer. Integrating these elements into the equivalent circuit enables a comprehensive analysis of the impedance parameters. The effectiveness of the coating was validated by observing a significant increase in the R1 value. Specifically, sample B1 displayed an R1 value of 81.427 Ohms, indicating a considerable enhancement in its resistance property compared to previous measurements. Based on these results, it's clear that the passive film doesn't completely cover the metal, posing difficulties in identifying it as a consistent layer. This observation is evident from the analysis of the morphology of samples B1.





**Figure. IV .14.** (a) Nyquist plot obtained from EIS analyses on Ni–Mn coatings in NaCl medium. (b) comparison of the curves.



**Figure. IV .15.** (a) Bode-magnitude and (b) Bode-phase plot obtained from EIS analyses on Ni–Mn coatings in NaCl medium. (c) ECC used to fit Nyquist curves.

**Table IV.3.** EIS findings of Ni–Mn coating.

	<b>B1</b>	<b>B2</b>	<b>B3</b>	<b>B4</b>
R <sub>1</sub> , KΩ cm <sup>2</sup>	0.81	0.79	0.20	0.048
Q <sub>1</sub> , mF	0.084	0.092	0.034	0.33
Q <sub>2</sub> , mF	0.181	0.159	0.112	0.0003
R <sub>2</sub> , KΩ cm <sup>2</sup>	82.02	87.85	0.06	0.015

### III.2.3.2 Electrochemical impedance spectroscopy of Zn–Ni–Mn

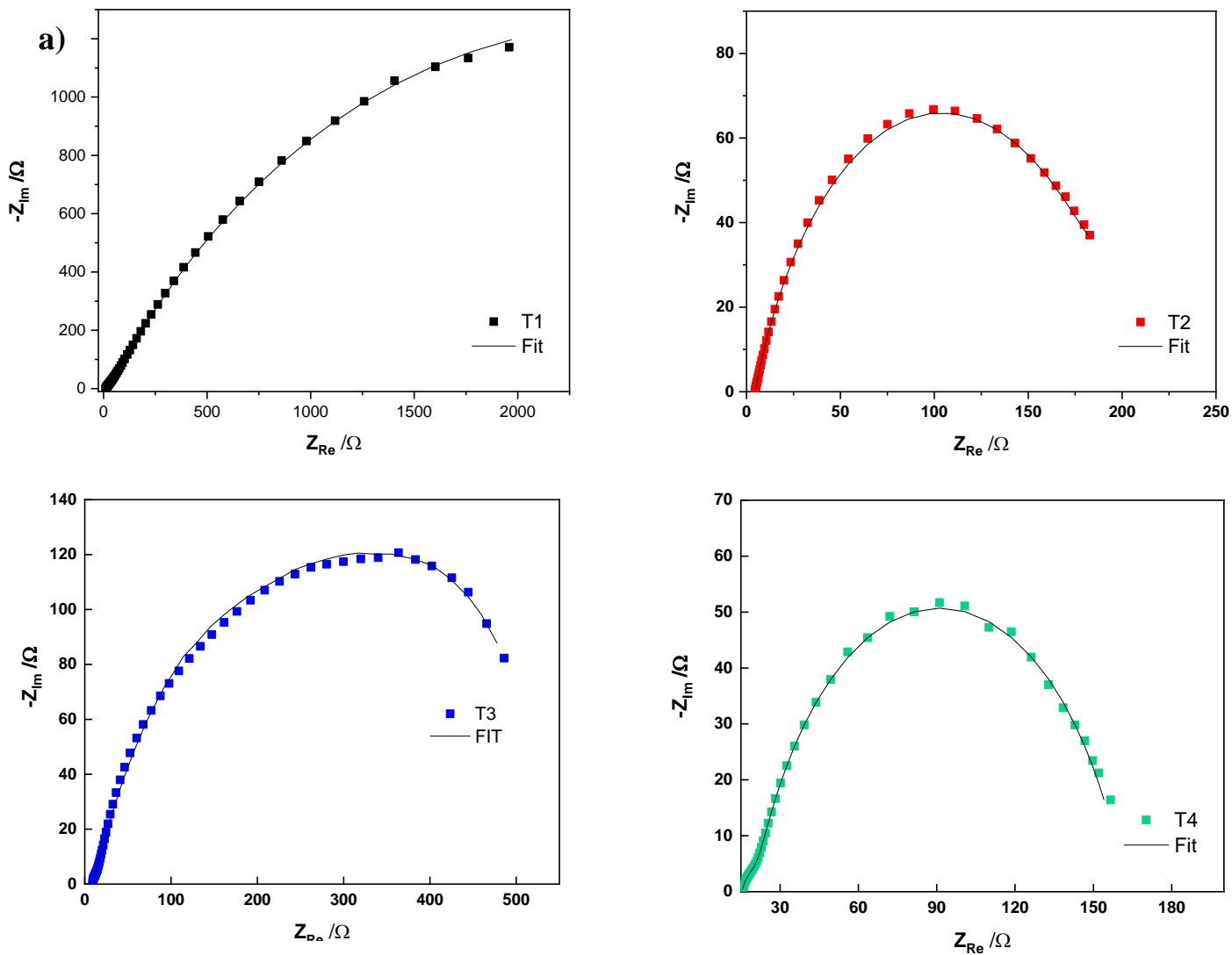
The corrosion performance of Zn–Ni–Mn coatings with differing Mn contents was examined through EIS. The associated experimental Nyquist diagrams are depicted in Figure 16. (a) showing a similar behavior. Specifically, the shape of all the recorded Nyquist diagrams can be characterized by one or two semi-circles, referred to as capacitive loops, which linked to the oxide products that developed at the double layer

interface and surface of the films[21]. The existence of multiple capacitive loops indicates that the corrosion product may consist of a monolayer or multilayer with either a relatively dense or porous structure. Specifically, the presence of a single time constant is attributed to the formation of a homogeneous layer structure, whereas the presence of two sublayers results in two distinct constants.

The semi circles are followed by the Warburg tail, in the lower frequency region (LF), known as Warburg impedance and corresponding to the diffusion of corrosive species through the coatings surface. Consequently, the acquired spectra were interpreted using a fitting model that incorporates considerations for both charge transfer and mass transport effects. This model serves to elucidate the physical processes transpiring at the metal-electrolyte interface, providing a comprehensive understanding of the electrochemical reactions transpiring at the electrode/electrolyte interface. Consequently, the experimental data were fitted to an appropriate equivalent electrical circuit (EEC), shown in the inset of **figure IV. 17. c)**. resulting from the arrangement of different electrical elements ( $R_s$ ,  $R_{ct}$ , CPE,  $W$ ). The EEC can be described by parallel combinations of the constant phase element (CPE), the charge transfer resistance ( $R_{ct}$ ) and the Warburg diffusion impedance,  $W$ , jointly in series with the solution resistance ( $R_s$ ). Herein, it becomes necessary to replace the capacitor,  $C_{dl}$ , with a constant phase element (CPE) to achieve a more accurate fit of depressed capacitive loops. This adjustment is essential because the shape of the Nyquist plot deviates from a perfect semicircle, primarily due to frequency dispersion resulting from surface inhomogeneities on the electrode. From figure IV.16. a), the Nyquist plot clearly indicate that the diameter of the capacitive loops, associated to the resistance of the electron charge transfer ( $R_{ct}$ ), increases by decreasing the quantity of Mn in the films. The significant enlargement of the capacitive loop diameter in Nyquist plots is attributed to the formation of corrosion-resistant products, which serve to protect the surface of the working electrode [22]. It's noteworthy that the highest recorded value of  $R_{ct}$  is observed for the Zn-Ni-Mn coating (T1) containing 1.6 wt. % Mn. This observation indicates that the incorporation of lower Mn content and higher Ni content in the deposit enhances Zn-Ni-Mn Films' corrosion resistance. These findings align with those previously reported from the study of polarization Tafel plots.

The logarithm of the impedance modulus and the corresponding phase angle are plotted as a function of the logarithm of the frequency of the applied signal in two different

plots, named the Bode plot, As illustrated in Figure IV.17a, there is a noticeable increase in impedance modulus values for deposits with lower Mn and higher Ni contents, suggesting an enhancement in corrosion protection. In the phase angle plots, two distinct maxima corresponding to two-time constants of the corroded interface are observed



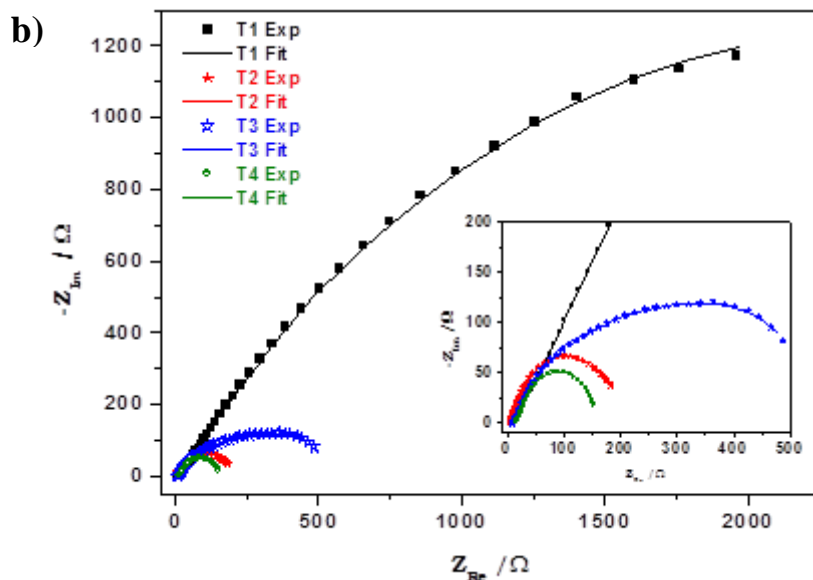


Figure IV. 16 (a) Nyquist plots obtained from EIS analyses on Zn–Ni–Mn films in NaCl medium. (b) comparison of curves.

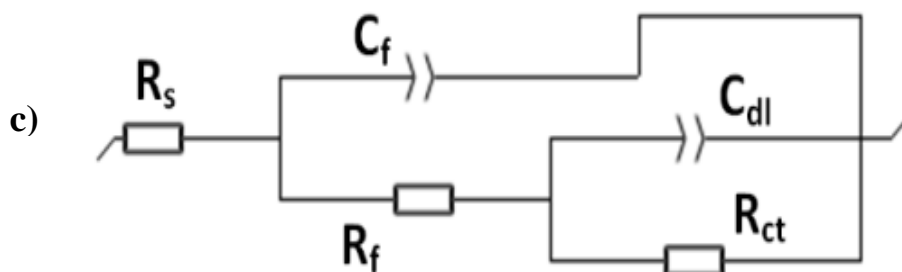
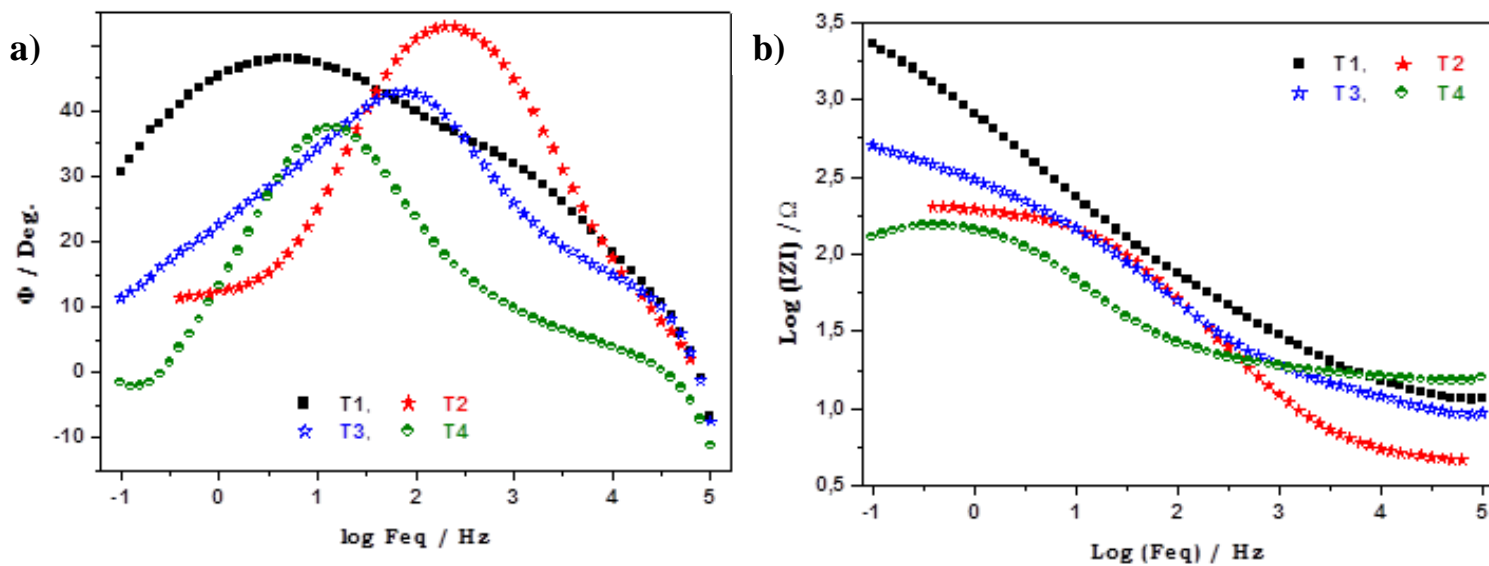


Figure III. 17: (a) Bode-magnitude and (d) Bode-phase plot obtained from EIS analyses on Zn–Ni–Mn films in NaCl solution. (c) ECC used to fit Nyquist curves.



**Table IV. 3.** EIS findings of Zn-Ni-Mn coatings

	<b>T1</b>	<b>T2</b>	<b>T3</b>	<b>T4</b>
$R_s, K\Omega \text{ cm}^2$	0.011	0.005	0.010	0.016
$CPE_{ct}, \text{mF}$	0.004	0.15	0.51	0.18
$R_{ct}, K\Omega \text{ cm}^2$	0.04	0.20	0.44	0.01
$CPE_f, \text{mF}$	0.34	8.78	3.73	0.39
$R_f, K\Omega \text{ cm}^2$	4.95	0.17	0.12	0.14
$R_c = R_f + R_{ct}$	44.99	0.37	0.56	0.15

### IV.3. Conclusion

This study investigated the influence of  $[Mn^{2+}]$  on the various characteristics of Ni–Mn and Zn–Ni–Mn films, including coatings surface morphology, particle size, crystalline structure and corrosion resistance.

The surface morphology of Ni–Mn coatings is characterized by a cauliflower-like structure, globular-shaped particles, ranging from 0.5 to 5  $\mu\text{m}$ , along with noticeable porosity and cracks. The crystal structure predominantly comprises pure nickel with favored orientations (111), (200), and (220) in the FCC structure. Notably, changes in manganese content are clearly observed through changes in the orientations of the Ni lattice. These coatings offer effective cathodic protection for Cu substrate enveloping them with a protective oxide layer ( $MnO_2$  oxide and Ni (OH)Cl hydroxide) characterized by a non-uniform highly porous microstructure and diverse shapes and sizes of particles. Incorporating a small amount of Mn in the bath significantly improved corrosion resistance, indicating the nobler character of the coatings with lower Mn content. Corrosion behavior of Ni–Mn coatings is directly influenced by the chemical composition of the coatings.

Zn–Ni–Mn coatings, which have pyramidal-shaped particles, are consistent with the typical morphology of Zn deposits. Importantly, the coatings reveal a crack-free surface and the particle sizes ranging from 0.2 to 2  $\mu\text{m}$  across all examined coatings. In these

alloys, both Ni and Mn exhibited complete solubility within the Zn matrix. Therefore, the formation of the ( $\eta$ -Zn) and NiZn<sub>3</sub> phases is confirmed. These phases support excellent corrosion resistance with the passive layer including Zn<sub>5</sub>(OH)<sub>8</sub>Cl<sub>2</sub>, ZnO, and ZnMn<sub>2</sub>O<sub>4</sub> phases.

LPT results of Ni–Mn shows a stable passive film on the interface. With increasing Mn deposited,  $I_{\text{corr}}$  increases from 0.009 to 0.235  $\mu\text{A}/\text{cm}^2$ , while  $E_{\text{corr}}$  becomes more negative (-0.299 to -0.514 V Ag/AgCl) and  $R_p$  decreases from 17 to 0.37 k $\Omega$ . The Ni<sub>96.9</sub>Mn<sub>1.5</sub> coating exhibits the highest resistance at 17 k $\Omega$ . For Zn–Ni–Mn coatings, all curves exhibit similar behavior without pitting corrosion. As  $[\text{Mn}^{2+}]$  in the bath changes,  $I_{\text{corr}}$  increases from 34 to 91  $\mu\text{A}/\text{cm}^2$ ,  $E_{\text{corr}}$  becomes more negative, and corrosion resistance decreases from 8.76 to 0.48 K $\Omega$ . A film containing Zn, Ni, and Mn at 55.7%, 37.7%, and 1.6% by weight respectively, demonstrates the lowest  $I_{\text{corr}}$ , highest  $E_{\text{corr}}$ , and maximum  $R_p$  values.

EIS analyses of Ni–Mn films shows semicircle loops in Nyquist plots of various coatings. The equivalent circuit includes two parallel elements: Q1 (double electric layer) and  $R_1$  (charge transfer resistance), as well as Q2 (film capacitance) and  $R_2$  (film resistance). Zn–Ni–Mn coatings Nyquist plots show one or two capacitive loops and a Warburg tail. Data fitting used an EEC model, replacing Cdl with a CPE for improved fitting. Decreasing Mn content enlarges the capacitive loop diameter. The highest  $R_{\text{ct}}$  value recorded in the 1.6 wt.% Mn Zn-Ni-Mn coating.

**References**

- [1] M. D. Abràmoff, P. J. Magalhães, and S. J. Ram, “Image processing with imageJ,” (2004) *Biophotonics Int.*, v. 11, no. 7, pp. 36–41,
- [2] K. S. Ramakrishna *et al.*, “Evaluation of Structural, Micro-structural, Vibrational and Elastic Properties of Ni–Cu–Zn Nanoferrites: Role of Dopant Cu<sup>2+</sup> at Constant 0.1 mol% in Ni–Zn Spinel Structure,” (2021), *J. Inorg. Organomet. Polym. Mater.*, v. 31, no. 3, pp. 1336–1346,
- [3] A. Farooq, S. Ahmad, K. Hamad, and K. M. Deen, “Effect of Ni Concentration on the Surface Morphology and Corrosion Behavior of Zn-Ni Alloy Coatings,” 2022. *Metals*, v, 12, 96.
- [6] J. Guo, X. Guo, S. Wang, Z. Zhang, J. Dong, and L. Peng, “Applied Surface Science Effects of glycine and current density on the mechanism of electrodeposition , composition and properties of Ni – Mn films prepared in ionic liquid,” (2016), *Appl. Surf. Sci.*, vol. 365, pp. 31–37,
- [7] C. Savall, C. Rebere, D. Sylla, M. Gadouleau, P. Refait, and J. Creus, “Morphological and structural characterisation of electrodeposited Zn-Mn alloys from acidic chloride bath,” (2006), *Mater. Sci. Eng. A*, vol. 430, no. 1–2, pp. 165–171,
- [8] Y. Tsuchiya, S. Hashimoto, Y. Ishibashi, T. Urakawa, M. Sagiya, and Y. Fukuda, “Structure of electrodeposited Zn-Mn alloy coatings,” (2000, *ISIJ Int.*, v. 40, no. 10, pp. 1024–1028,
- [9] J. and W. J. van Ooij, “Study of Zn-Ni and Zn-Co alloy coatings electrodeposited on steel strips I: Alloy electrodeposition and adhesion of coatings to natural rcompounds,” (1992), *Surf. Coatings Technol.*, v. 52, no. 1, pp. 17–30,
- [10] S. Anwar, F. Khan, and Y. Zhang, “Corrosion behaviour of Zn-Ni alloy and Zn-Ni-nano-TiO<sub>2</sub> composite coatings electrodeposited from ammonium citrate baths,” (2020), *Process Saf. Environ. Prot.*, vol. 141, pp. 366–379,
- [11] Abdel RahmanEl-Sayed, H. S. Mohran, and H. M. Abd El-Lateef, “Corrosion study of zinc, nickel, and zinc-nickel alloys in alkaline solutions by Tafel plot and impedance techniques,” (2012), *Metall. Mater. Trans. A Phys. Metall. Mater. Sci.*, v. 43, no. 2, pp. 619–632,
- [12] L. Wang, J. Zhang, Y. Gao, Q. Xue, L. Hu, and T. Xu, “Grain size effect in corrosion behavior of electrodeposited nanocrystalline Ni coatings in alkaline

- solution,” (2006), *Scr. Mater.*, v. 55, no. 7, pp. 657–660,
- [13] F. H. Assaf, M. M. Abou-krisa, W. M. Daoush, and A. A. Eissa, “Zn-Ni-Mn alloy by electrodeposition and its characterization,” (2018), *Russian Journal of Applied Chemistry*, v, 91, No. 3, pp. 510–519.
- [14] B. Abedini, N. Parvini, S. Yazdani, and L. Magagnin, “Surface & Coatings Technology Structure and corrosion behavior of Zn-Ni-Mn / Zn e Ni layered alloy coatings electrodeposited under various potential regimes,” (2019), *Surf. Coat. Technol.*, v. 372, no. March, pp. 260–267,
- [15] L. D. Bailote, R. Ramanauskas, and P. Bartolo-p, “Mn Oxide film as Corrosion Inhibitor Of ZN-MN coatings,” pp. 41–52.
- [16] N. Boshkov, “Galvanic Zn – Mn alloys — electrodeposition , phase composition , corrosion behaviour and protective ability,” 2003, *Surface and Coatings Technology*, v. 172, no. 11, pp. 217–226,
- [17] H. S. Lee *et al.*, “Corrosion mechanism and kinetics of Al-Zn coating deposited by arc thermal spraying process in saline solution at prolong exposure periods,” (2019), *Sci. Rep.*, vol. 9, no. 1, pp. 1–17,
- [18] Z. I. Ortiz, P. Díaz-Arista, Y. Meas, R. Ortega-Borges, and G. Trejo, “Characterization of the corrosion products of electrodeposited Zn, Zn-Co and Zn-Mn alloys coatings,” (2009), *Corros. Sci.*, vol. 51, no. 11, pp. 2703–2715,
- [20] T. Xue and H. J. Fan, “From aqueous Zn-ion battery to Zn-MnO<sub>2</sub> flow battery: A brief story,” (2021), *J. Energy Chem.*, v. 54, pp. 194–201,
- [21] H. H. Hernández *et al.*, “Electrochemical Impedance Spectroscopy ( EIS ): A Review Study of Basic Aspects of the Corrosion Mechanism Applied to Steels,” (2020) *.Electrochem. Impedance Spectrosc.*, pp. 1–35,
- [22] C. A. M. Dutra, J. W. J. Silva, and R. Z. Nakazato, “Corrosion Resistance of Zn and Zn-Ni Electrodeposits: Morphological Characterization and Phases Identification,”(2013), *Materials Sciences and Applications*,v. 4, pp. 644–648, 2
- [23] S. Ganesan, G. Prabhu, and B. N. Popov, “Electrodeposition and characterization of Zn-Mn coatings for corrosion protection,” (2014), *Surf. Coatings Technol.*, v. 238, pp. 143–151,

## *General Conclusion*

This study focused on the electrodeposition of Ni–Mn and Zn–Ni–Mn alloys on a copper substrate using a sulfate bath under different conditions, including different deposition potentials and  $[\text{Mn}^{2+}]$ . Various characterization techniques were employed to assess the coatings, encompassing CV, CA, EDX, SEM, and XRD. LTP and EIS were utilized to evaluate corrosion behavior.

The CV investigation revealed that the Ni–Mn and Zn–Ni–Mn curves differ from those observed in Zn, Ni, and Mn coatings. Additionally, the potential required for Mn formation is more negative compared to that for Ni and Zn deposition. The formation of Ni–Mn and Zn–Ni–Mn alloy is favored under more positive potential. The application of a more negative potential leads to the formation of brittle coating. Considering these results, the deposition potential was selected at  $-1\text{ V}$  (vs Ag/AgCl) for the Ni–Mn and  $-1.12\text{ V}$  (vs Ag/AgCl) for Zn–Ni–Mn alloys.

The CA experiments conducted for Zn, Ni, and Mn coatings reveal distinctive patterns in their electrochemical behavior. The chronoamperograms of Zn, Ni, and Mn, exhibit three discernible regions described by an initial rapid drop, subsequent increase, and eventual stabilization in current density. The mechanism and kinetics of nucleation and growth of Ni–Mn coatings is controlled by the diffusion of the electrochemical species, following, 3D progressive nucleation model. These processes depend on both the  $[\text{Mn}^{2+}]$  and the potential applied to the working electrode. The deposition potential of Zn–Ni–Mn coatings is highly sensitive, with a notable effect from the hydrogen release reaction. The nucleation and growth mechanism of Zn–Ni–Mn coatings are altered by changes in  $[\text{Mn}^{2+}]$  and deposition potential.

The Ni–Mn coatings' EDX results show that Mn, Ni, and S are present in the deposits, with Ni standing out as the main element, the electrodeposition of the Ni–Mn alloys is described as an induced process. In the case of Zn–Ni–Mn, the EDX results show the presence of Ni, Zn, and Mn atoms, with a notably higher Zn content. This observation suggests anomalous behavior in the electrodeposition process.

SEM morphological characterization reveals a significant variation in the obtained deposits' morphology and particles sizes with changes in  $[\text{Mn}^{2+}]$ . The Ni–Mn coatings exhibit a column–like structure with cauliflower–like agglomerates and pin–hole morphology. Particle

size distribution analysis suggests a wide range of sizes ( $\sim 0.5$  to  $5 \mu\text{m}$ ) due to competition between nucleation and growth phenomena, with fine particles dominating.

The Zn–Ni–Mn coatings display pyramidal-shaped particles, uniform morphology, reduced stress, and no cracks. Increased  $[\text{Mn}^{2+}]$  corresponds to a higher number of smaller particles ( $0.2 \div 0.6 \mu\text{m}$ ), indicating a faster nucleation rate compared to nucleus growth on the Cu surface.

The XRD results of the Ni–Mn coatings indicate the presence of Ni with favored orientations in the face-centered cubic (fcc) structure. Specifically, the preferred planes are Ni (1 1 1), (2 0 0), and (2 2 0). And formation of a solid solution Ni (Mn) and a crystalline structure of Increasing Mn deposited leads to changes in lattice parameters, suggesting effective incorporation of Mn into the Ni lattice, forming a solid solution. In the case of Zn–Ni–Mn coatings, the XRD patterns analysis demonstrates the formation of a Zn (Mn) solid solution. The coatings exhibit a cubic structure identified as  $\eta$ -Zn, Furthermore, the observed  $\gamma$ -NiZn<sub>3</sub> phase is characterized by orthorhombic symmetry.

The initial corrosion analyses (mass loss measurements) suggest that Ni, Ni–Mn, and Zn–Ni–Mn coatings effectively protect the substrate from corrosion. Zn–Ni–Mn coatings exhibit superior corrosion resistance compared to Ni and Ni–Mn alloy. Moreover, the SEM and XRD study reveals that the Ni–Mn coating surface is covered by a protective oxide layer (Ni, Ni (OH) Cl<sub>2</sub>, and MnO<sub>2</sub>), presenting a non-uniform, porous microstructure. Similarly, the Zn–Ni–Mn coating's surface is shielded by a non-uniform, porous oxide layer (Zn<sub>5</sub>(OH)<sub>8</sub>Cl<sub>2</sub>, ZnO, and ZnMn<sub>2</sub>O<sub>4</sub>) with diverse particle shapes and sizes.

The potentiodynamic curves of Zn, Ni, and Mn coatings illustrate superior corrosion resistance in Ni, characterized by a more positive potential and lower current densities compared to Zn and Mn coatings. Conversely, Zn exhibits the weakest corrosion resistance with the most negative  $E_{\text{corr}}$  values. The Mn corrosion potential differs significantly from existing literature, due to its thickness and fragile deposits. Ni–Mn coatings display diverse corrosion behavior influenced by Mn content. Higher Mn content increases corrosion rates, shifting  $E_{\text{corr}}$  values more negative and reducing corrosion resistance. Notably, incorporating a small amount of Mn significantly improves corrosion resistance.

Furthermore, the LPT curves for various Zn–Ni–Mn coatings reveal same behavior with no pitting behavior. The  $I_{\text{cor}}$ ,  $E_{\text{cor}}$ , and  $R_p$ , are influenced by Mn deposited in the coatings. The

coating with approximately 55.7% Zn, 37.7% Ni, and 1.6% Mn displays the highest corrosion resistance. The protective layer formation during coating dissolution involves Mn and Zn, leading to the creation of a compact passive layer,  $ZnMn_2O_4$ , and preventing pitting corrosion.

The EIS tests on Ni–Mn coatings, analyzed through Nyquist and Bode plots along with an equivalent circuit (EEC), revealed provided valuable findings, The curves exhibit distinctive semicircle loops. The equivalent circuit includes parallel elements,  $Q_1$  (representing the double electric layer) and  $R_1$  (denoting charge transfer resistance), along with  $Q_2$  (film capacitance) and  $R_2$  (film resistance). The increased of Ni and reduced Mn content in the Ni–Mn coatings enhanced corrosion resistance by challenging electron transfer and reducing double layer capacity.

(EIS) and the corresponding Nyquist diagrams, along with Bode diagrams, for Zn–Ni–Mn coatings revealed similar patterns. These diagrams displayed one or two capacitive loops and a Warburg tail in the lower frequency region, indicating varied structures within the corrosion product and the diffusion of corrosive species through the coating surface. The equivalent electrical circuit (EEC), encompassing the constant phase element (CPE), charge transfer resistance ( $R_{ct}$ ), and Warburg diffusion impedance. Corrosion resistance was enhanced with decreasing Mn content in the coatings, and the Zn–Ni–Mn coating with 1.6 wt. % Mn exhibited the highest  $R_{ct}$  value, suggesting improved corrosion resistance due to low Mn and high Ni content.